Synthesis and Catalytic Applications of Transition Metal Incorporated Mesoporous Materials

A Thesis submitted in the partial fulfillment of the requirement for the Degree of

Doctor of Philosophy

By

Shweta Sareen
(Regn. No: 901109003)

Under the supervision of

Dr. Satnam Singh
Professor
School of Chemistry & Biochemistry
Thapar University
Patiala -147004

Dr. Bonamali Pal
Professor & Head
School of Chemistry & Biochemistry
Thapar University
Patiala -147004

SCHOOL OF CHEMISTRY AND BIOCHEMISTRY
THAPAR UNIVERSITY, PATIALA – 147 004

Dedicated to
My
Parents and Teachers

Certificate

This is to certify that thesis entitled "**Synthesis and Catalytic Applications of Transition Metal Incorporated Mesoporous Materials**" being submitted by Shweta Sareen in the fulfilment of the requirement for the award of Degree of Doctor of Philosophy to the School of Chemistry and Biochemistry, Thapar University, Patiala, is a record of candidate's own work carried out by her under our supervision and guidance. The matter presented in the thesis has not been submitted in part or full to any other University or Institute for the award of any degree or diploma.

Dr. Satnam Singh
Professor
School of Chemistry & Biochemistry
Thapar University
Patiala -147004

Dr. Bonamali Pal
Professor & Head
School of Chemistry & Biochemistry
Thapar University
Patiala -147004

Candidate's Declaration

I, hereby declare that the work presented in the thesis entitled "**Synthesis and Catalytic Applications of Transition Metal Incorporated Mesoporous Materials**" in fulfilment of the requirement for the award of the Degree of Doctor of Philosophy, School of Chemistry and Biochemistry, Thapar University, Patiala, is an authentic record of my own work carried out under the supervision of Dr. Satnam Singh, Professor, and Dr. Bonamali Pal, Professor, at School of Chemistry and Biochemistry, Thapar University, Patiala, India. The matter embodied in this thesis has not been submitted in part or full to any other university or institute for the award of any degree in India or Abroad.

Shweta Sareen

Dr. Satnam Singh
Professor
School of Chemistry & Biochemistry
Thapar University
Patiala -147004

Dr. Bonamali Pal
Professor & Head
School of Chemistry & Biochemistry
Thapar University
Patiala -147004

Acknowledgements

I thank God for being always with me and for everything he has done for me. This Thesis is the result of four and a half year hard work supported by many people. It is very difficult to express gratitude to all of them in few lines.

First of all, I would like to express my sincere appreciation to my Supervisors Dr. Satnam Singh and Dr. Bonamali Pal, School of Chemistry and Biochemistry, Thapar University, Patiala for accepting me to guide for Ph.D Degree. I am greatly indebted to them for their kind guidance, constructive criticism, valuable suggestions, discussions, and moral support. They mentored me at each and every point from the elementarily steps to complex experimental design. They have always been pillars of support and constant source of inspiration.

I am also extremely thankful to the Director, Dean (Research & Sponsored Projects) and Head, School of Chemistry & Biochemistry, Thapar University, for extending the opportunity to undertake this doctoral research.

I would be failing in my duties if I do not mention Departmment of Science & Technology for providing fellowship under Women Scientist Scheme (WOS-A) and the members of the doctoral committee for monitoring my research work from time to time and giving their valuable suggestions.

I would also like to acknowledge Mr. Chander Singh, Lab Assistant and other members of the School of Chemistry & Biochemistry for their support and co-operation.

This journey would not have been easy without the support of my Friends and Lab-mates, Foremost of them being Ms. Prinka Singla who has always been on my

side and lending me the required support whenever I needed the most. I would like to acknowledge Dr. Bhupender Pal thakur, Dr. Inderpreet Singh Grover, Mrs. Anila Monga, Roopchand Prajapat, Rayees Ahmad, Tanushree Basu, Mr. Sharad Tiwari and Syed Lynofer for their support and co-operation.

I am indebted to parents, my father, Late, Mr. Vinod Sareen who had been a source of motivation and encouragement in my life. I would like to acknowledge My mother Mrs. Meeta Sareen for all the sacrifices she has made for me. Her understanding and her love has always encouraged me to be steadfast and never bend to difficulties in life. I would also like to acknowledge constant love and support of my sisters, Nidhi and Sheena.

Words cannot express how grateful I am to my grandparents (in-laws) Mr. Shanu Ram Mehta and Mrs. Santosh, my father-in-law Mr. Sukhdev Lal and mother-in-law Mrs. Nirupma Mehta for their unconditional love, unending support and blessings. I would like to acknowledge my sisters-in-law, Mrs. Urvashi Chugh, Mrs. Meenakshi Verma, and brothers-in-law Mr. Amit Chugh and Mr. Nikhil Verma for their prayers, affection and love.

Last but not the least I would like to acknowledge my husband Dr. Vishal Mutreja and My Daughter Chahak for being my backbone through this entire journey of Ph.D.

Table of Contents

nanocomposites

List of Abbreviations

UV	Ultraviolet
Vis	Visible
DRS	Diffuse reflectance spectroscopy
HPLC	High pressure liquid chromatography
GC	Gas chromatography
GC-MS	Gas chromatography - mass spectrometry
SAED	Selected area electron diffraction
EDX	Energy dispersive X-ray spectroscopy
BET	Brunauer- Emmett-Teller
BJH	Barret-Joyner-Halenda
FT-IR	Fourier Transform Infra red
IUPAC	International Union of Pure and Applied Chemistry
JCPDS	Joint Committee on Powder Diffraction Standards
TEM	Transmission Electron Microscope
HR-TEM	High resolution- Transmission Electron Microscope
XRD	X-ray Diffraction
TGA	Thermo Gravimetric Analysis
XPS	X-ray photon spectroscopy
MP-AES	Microwave plasma-Atomic emission spectroscopy
CMC	Critical micelle concentration
TOF	Turn over frequency
IEP	Isoelectric point
FCC	Face centred cubic
SBA-15	Acronym for Santa Barbara
MCM	Mobil composition of matter
APTMS	3-aminopropyltrimethoxysilane
APTES	3-aminopropyltriethoxysilane
ap-SBA-15	APTES/APTMS modified SBA-15
m-SBA-15	surface modified SBA-15

MMs	Mesoporous materials
IWI	Incipient Wetness Impregnation
DP	Deposition-precipitation
MWI	Microwave irradiation
CVD	Chemical vapour deposition
PLA	Pulsed laser ablation
PDA	pH assisted delay-addition method
MCS	Mechanochemical synthesis
WPO	wet peroxide-oxidation
PVP	Poly vinyl pyrollidone
TEOS	Tetra ethyl orthosilicate
AN	Aniline
NB	Nitrobenzene
m-DNB	*m*-dinitrobenzene
m-PDA	*m*-phenylenediamine
m-NA	*m*-nitroaniline
m-CNB	*m*-chloronitrobenzene
m-CAN	*m*-chloronitroaniline
m-NT	*m*-nitrotoluene
m-AT	*m*-aminotoluene
p-DNB	*p*-dinitrobenzene
p-PDA	*p*-phenylenediamine
p-NA	*p*-nitroaniline
p-NP	*p*-nitrophenol
p-AP	*p*-aminophenol
wt.%	Weight Percentage
BM	Bimetallic
NPs	Nanoparticles
NS	Nanospheres
NR	Nanorods
min	Minute

mol	Mole
mM	Milli molar
mL	Milli litre
µmol	Micro mole
nm	Nanometre
mM	Milli molar
mL	Milli litre
µl	Micro litre
µm	Micro metre
nm	Nanometre
a.u.	Astronomical unit

List of symbols

Å	Angstrom
A	Absorbance
°	Degree
λ	Wavelength
%	Percentage
µ	Micro
h	Hour
g	Gram
mg	Milligram
s	Second
L	Length
W	Width
υ	Frequency
θ	Theta
C	Concentration
C_o	Initial Concentration
^oC	Degree Celsius
% T	Transmittance
M	Molar

Abstract

The work presented in the thesis sheds light on the synthesis of SBA-15 supported transition metal nanocomposites and their importance as improved catalytic systems for the reduction of nitroaromatics. The main emphasis has been laid on the synthesis of varying morphologies of transition metallic nano species within the mesoporous host as a function of increased metal loading and studying its effect on the various physicochemical and catalytic properties of nanocomposites. The whole work has been divided into five chapters.

Chapter 1 Introduction, Literature survey and Experimental procedures

This chapter provides a brief introduction to the historical background of the porous materials, different pathways of synthesis of mesoporous materials like SBA-15, importance of SBA-15 as a preferred mesoporous host. Moreover, reports based on the recent developments in the field of transition metal (Au, Ag, Cu/CuO as well as bimetallic Au-Ag) supported SBA-15 nanocomposites have also been discussed. A brief description of the methodology and various techniques used for the characterization of optical, thermal, surface structural morphology and catalytic properties of prepared nanocomposites have also been incorporated.

Chapter 2 Homogeneous dispersion of Au nanoparticles into mesoporous SBA-15 exhibiting improved catalytic activity for nitroaromatic reduction

This chapter demonstrates the synthesis of homogeneously dispersed Au loaded SBA-15 nanocomposites by varying the Au loading from 1-5 and 10 wt. % by post modified method. It was found that with an increase in the amount of Au loading, followed by calcination at 350 ^{o}C, a change of morphology from Au nanospheres (5-6 nm) for 4 wt. % Au loading to rod-like Au nanostructures (width 6-9 nm and length 90-180 nm) beyond 5 wt. % loading was observed. The surface area (664 m^2/g) and pore volume (1.33 cm^3/g) of bare SBA-15 were significantly reduced to 292 m^2/g and 0.6031 cm^3/g for Au nanosphere, and 457 m^2/g and 0.7677 cm^3/g for Au nanorod dispersed SBA-15, respectively, due to partial filling of mesopores. Moreover, the quantum sized, non-aggregated Au nanostructures stabilized within the mesochannels of SBA-15 exhibited improved catalytic activity over catalytically inactive bare SBA-15 with 89 % selectivity for *m*-phenylenediamine and 81% for *p*-nitroaniline formation for the reduction of *m*- and *p*-dinitrobenzene respectively.

Chapter 3 Preparation, surface structural morphology and catalytic properties of uniformly dispersed Ag nanoparticle loaded mesoporous SBA-15

This chapter deals with the preparation of varying morphologies of Ag nanoparticles within the channels of APTMS modified SBA-15 and study of the changes in physicochemical parameters and catalytic properties with increased Ag impregnation. The prepared materials were characterized by XRD, TEM, FTIR and solid-state UV-Visible spectroscopy. It was found that gray colored samples were formed with Ag impregnation in comparison to white colored bare SBA-15, exhibiting broad absorption band in the range of 450-500 nm and a weak absorption band at 700-900 nm indicating the formation of long anisotropic Ag nanostructures (Ag nanorods) within the mesoporous matrix. XRD studies revealed the retention of mesoporous structure, even after surface modification with APTMS and Ag loading. TEM micrographs depicted well dispersed Ag nanostructures (7-8 nm) fixed within the mesoporous matrix. Moreover, incorporation of Ag led to a significant decrease from 680 m^2/g of SBA-15 to 385 m^2/g due to plugging of mesopores with Ag. The Ag-impregnated SBA-15 catalyst displayed superior catalytic activity than bare SBA-15 with 4 wt. % Ag-loaded catalyst exhibiting optimum activity for selective reduction of *p*-nitrophenol to p-aminophenol (100%) and *p*-dinitrobenzene to *p*-nitroaniline (87%) along with small amount of *p*- phenylenediamine formation. Moreover, comparative studies of various physicochemical and catalytic parameters pertaining to 4 wt. % Au/Ag/CuO loaded SBA-15 nanocomposites have also been discussed.

Chapter 4 Fine CuO anisotropic nanoparticles supported on mesoporous SBA-15 for selective hydrogenation of nitroaromatics

This chapter illustrated the formation of well dispersed CuO nanospheres (~5-6 nm) and nanorods (aspect ratio ~11-20 nm) having monoclinic crystal phase within the mesoporous channels of SBA-15. Moreover, the effect of calcination temperature, changes in the size, shape, dispersion ability and catalytic activity of the metal oxide NPs present within the mesoporous host as a function of increased metal loading have also been discussed. It has been supported by various characterization techniques. Elemental mapping studies confirmed uniform distribution of CuO nanoparticles on the surface of SBA-15. An increase in surface area was also observed from 694 m^2g^{-1} for SBA-15 to 762 $m^2g^{-1}$for 10 wt. % Cu loading probably due to the deposition of an excess of CuO nanoparticles on the outer siliceous surface. The high surface area of the 10 wt. % CuO/ap-SBA-15 also contributed to the efficient adsorption of nitro groups on the

active sites of the CuO/ap-SBA-15 resulting in enhanced catalytic activity. The catalytic activity also increased with Cu loading and 10 wt. % CuO/ap-SBA-15 catalyst displayed the highest catalytic activity for the reduction of *m*-chloronitrobenzene and *m*-nitrotoluene with 83 % and 100 % selectivity for *m*-chloroaniline and *m*-aminotoluene respectively. The reaction rate showed dependence on the electron withdrawing ability of the substituents present on nitrobenzene and was found to be maximum for *m*-CNB.

Chapter 5 Uniform dispersion of a bimetallic/binary mixture of Au-Ag supported SBA-15 nanocomposites for selective reduction of nitroaromatics

This chapter comprises the formation of a binary mixture of Au-Ag nanoparticles with controlled shape and size supported on mesoporous SBA-15 by post modified method involving variation in the amount of Au loading w.r.t fixed Ag loading. DRS studies showed the presence of single plasmon band for various bimetallic Au:Ag loadings illustrating that the NPs formed an alloy structure with homogeneous composition.TEM micrographs depicted discrete bimetallic nanostructures uniformly distributed and stabilized within/on the surface of the mesoporous host. Among all bimetallic nanocomposites, Au:Ag(5:1)/*m*-SBA-15 nanocomposites exhibited the best catalytic activity ($k= 2.12\times10^{-2}$ min^{-1} and 3.99×10^{-2} min^{-1}) in comparison to monometallic Au/*m*-SBA-15 and Ag/*m*-SBA-15 nanocomposites for the selective reduction of nitrobenzene (NB) to aniline (AN) and *p*-nitroacetophenone (*p*-NAP) to *p*-aminoacetophenone (*p*-AAP)respectively. The strong synergism between Au and Ag resulted in the improved catalytic activity of the bimetallic Au:Ag nanocomposites in comparison to the monometallic Au/Ag counterparts and bare SBA-15 for the reduction of NB and *p*-NAP respectively. The catalytic activity was greatly influenced by metal loading, surface area and distribution of bimetallic nanospheres within/on the surface of the mesoporous host.

Chapter 1

Introduction, Literature survey and Experimental

1.1 Introduction

1.1.1 Porous materials

A porous material is a solid substance having interconnected network of pores (voids). Due to the interconnection between the pores, various atoms, ions and molecules are able to interact among themselves at the surface as well as in the bulk of the material. As a result, they exhibit potential applications in the field of adsorption, ion exchange and catalysis. Different known porous substances are clays, rocks, bones, ceramics, carbonaceous materials and metal oxides. Generally, porous materials (Sing et al., 1985) are characterized by their porosity (ratio of the volume of pore space to the total volume of the material) which lies between 0.2-0.95 as well as their textural and physical properties. According to IUPAC, depending on the sizes of the pores, the porous materials are classified as (i) Microporous materials having pore diameters upto 2 nm, (ii) mesoporous materials (MMs) with pore diameter within the range of 2-50 nm and (iii) macroporous materials with pore diameter above 50 nm (Zhao et al., 1996). Moreover, depending upon the distribution of pore sizes, shapes and uniformity of pore spaces, these materials can be manipulated to form new materials with unusual properties resulting in the scope beyond their traditional use as catalysts by ranging from microelectronics to medical diagnosis (Davis et al., 2002). Among various porous materials, silica based porous materials such as zeolites, mesoporous silicates and aluminosilicates have been extensively studied and characterized as they offer a better control over mesostructure leading to wide applications in catalysis, adsorption, sensors and drug delivery (Alothmann et al., 2010).

1.1.2 Historical background of porous materials

Zeolites constitute an important and oldest member of the family of crystalline porous materials. Zeolites were discovered by Cronsted et al. (1956) from the mineral stilbit (David et al., 1992). They are hydrated crystalline tectoaluminosilicates composed of XO_4 tetrahedra (X being tetrahedral atom i.e., Si, Al and tetco refer to the presence of two adjacent tetrahedra sharing a single apical oxygen atom) giving a framework ratio of O/X = 2. Aluminosilicates have negatively charged oxide framework, whereas pure silicate structure, does not carry any charge.

Zeolites are composed of molecular sieves like structure forming regular arrays of channels or cavities that can be filled with water or any guest molecules. As a result, they are widely used in the shape selective processes such as ion-exchange, sorption and catalysis (Barrer et al., 1982; Breck et al., 1974; Szostak et al., 1989). Although these materials offered an increase in scientific curiosity but suffered limited application due to small pore size (0.8-1.3 nm), low stability and weak acidity. On the other hand, the pioneering findings by Kresge et al. (1992) led to the synthesis of ordered MMs, a major breakthrough in the development of high surface area porous materials with tunable porosity. Silica was preferred as the main building block for MMs as it was inexpensive, inert, harmless, thermally stable and abundant in the earth's crust. Furthermore, the discovery of M41S, a new family of silicate/aluminosilicate mesoporous molecular sieves stimulated a massive research, not been limited to MMs but also extended to organic-inorganic hybrid MMs (Parida et al., 2009) and other metal-oxide systems other than silica. M41S family exhibited high surface area, uniform pore structure and pore volume with three mesophases comprising hexagonal MCM-41, cubic MCM-48 and lamellar MCM-50 (Attard et al., 2001).

However, a remarkable contribution towards mesoporous chemistry was made by Zhao et al. (1998) for synthesizing SBA-n type materials (SBA-1, SBA-3 and SBA-15) using nonionic triblock copolymer as a template in the acidic medium. In comparison to other reported MMs, SBA-15 showed outstanding features like easy synthesis, remarkable reproducibility over a wide temperature range (35-130 ^{o}C), tunable pore size (~5-30 nm), high surface area, thicker walls (Khodakov et al., 2005; Linssen et al., 2003) with greater hydrothermal and mechanical stability, making it one of the promising investigated material towards a wide range of applications in catalysis (Ressler et al., 2008). The synthesis of SBA-15 involves the use of the non-ionic triblock ($EO_{20}PO_{20}EO_{20}$) copolymer as template and use of different silica sources viz., tetramethyl orthosilicate (TMOS), tetraethyl orthosilicate (TEOS) or tetrapropyl orthosilicate (TPOS) as a source of the framework under strongly acidic conditions and was influenced by the reaction conditions and surfactant concentration. Amorphous silica was formed below 0.5 wt. % concentration of block polymer whereas formation of silica gel was observed above 6 wt. %. Furthermore, the formation of SBA-15 can be achieved within a temperature range of 35-80 ^{o}C and pH ~1. A slight variation in the temperature or pH may result in the formation of disordered/amorphous silica (~25 ^{o}C, neutral pH) or silica gel (80 ^{o}C and pH ~2-6). Hence, by

the use of suitable acidic conditions and block polymer concentration, mesoporous SBA-15 with thicker walls (31-64 A^o) and greater hydrothermal stability can be prepared in comparison to other MMs like MCM-41. Despite the presence of many promising properties, the existence of neutral framework and absence of Brønsted acidity limits their application in catalysis. This limitation was overcome by modifying or functionalization of SBA-15 surface by various organic groups such as aminopropyl (Chen et al., 2012), sulphonic (Margolesse et al., 2000), carboxylic (Chen et al., 2013), imidazole (Zhang et al., 2014a) and triazole (Park et al., 2010) that act as a binding agent and a stabiliser for immobilising enzymes onto SBA-15 and incorporation of different metals in SBA-15 framework.

1.1.3 Formation of mesoporous materials (MMs)

Generally, the formation of MMs is influenced by self cooperative assembly between the template and the silica as an inorganic precursor in solution. The template can be an organic compound, a block copolymer, dendrimer or surfactant. The surfactant molecule is amphiphilic that is made up of a hydrophilic head and a hydrophobic tail that self organizes beyond CMC (critical micelle concentration) into micelles to achieve minimum energy and maximum stability. The different assemblies attained by the micelles is attributed to the fusion of intermolecular (H-bonding, van der Waals, Coulombic) and entropy interactions. However, synthesis of MMs is based on the liquid crystal templating (LCT) mechanism (Fig. 1.1) involving two basic pathways (Beck et al., 1992). Pathway 1, involves preformation of liquid crystal phase by the accretion of the surfactant micelles into micellar rods that rearrange among themselves to form hexagonal arrays, followed by condensation of silicate species around the preformed hexagonal micellar arrays. The second pathway is silicate initiated pathway involving the adsorption of silica around an external surface of surfactant micellar rod through coulombic or other interactions. Thereafter, the silicate coated micellar rods cluster among themselves in a hexagonal mesophase followed by silicate condensation. Finally, the organic materials are removed by calcination resulting in a stable mesoporous molecular sieve. Another pathway involves the formation of the nanometric inorganic component by the polymerisation of inorganic precursor or precipitation reaction which is the limiting factor for mesostructure syntheses. Nanometric building block (NBB) can congregate among themselves interconnected by organic groups present on their surface, resulting in the formation of ordered/disordered hybrid assemblies.

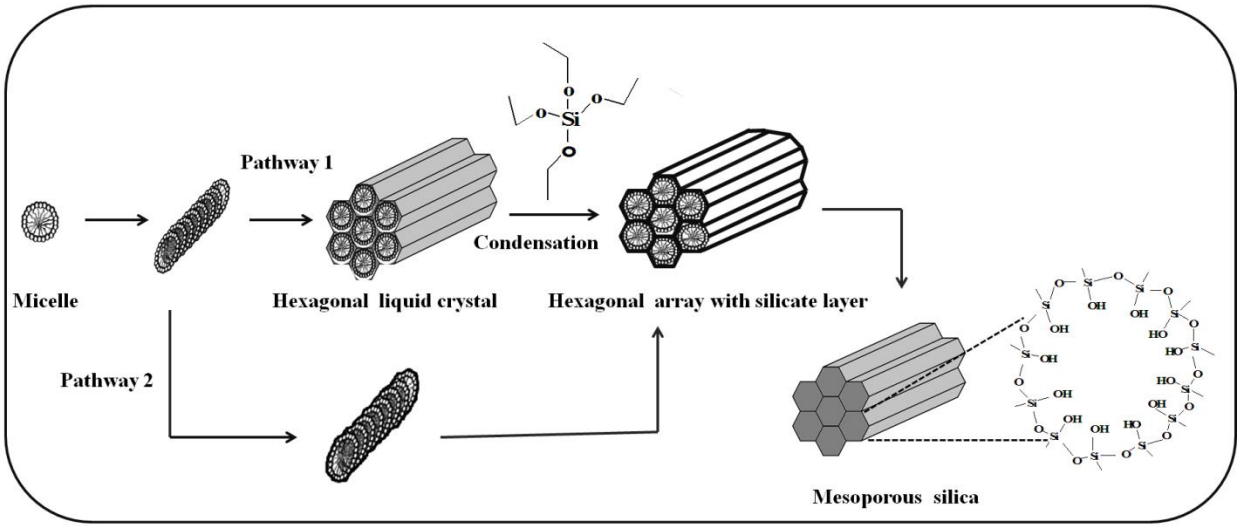

Fig. 1.1 Different synthetic pathways of mesoporous silicates

Studies showed different interactions between inorganic silicate precursor and the surfactant species in solution viz., electrostatic repulsion between polar heads, hydrophobic interactions between organic chains, geometric restrictions due to molecular packing and entropy restrictions that are detrimental factors in governing the synthesis of different mesophases. The formation of different mesophases is directed by different reaction pathways (Huo et al., 1994a, 1994b). For ionic surfactants, electrostatic interactions between the surfactant (S) and inorganic precursor (I) bearing opposite charges, govern the formation of MMs either by the direct syntheses i.e., S^+I^- /S^-I^+ or indirect syntheses i.e., $S^+X^-I^+$ and $S^-M^+I^-$. The direct syntheses route consists of (i) The (S^+I^-) route: Ion pairs (S^+I^-) are formed by the direct co-condensation of anionic inorganic species (I^-) with a cationic surfactant (S^+) e.g., M41S family. (ii) The (S^-I^+) route: Self-assembling of cationic inorganic species (I^+) with anionic surfactant (S^-) by means of (S^-I^+) ion pairs e.g., hexagonal tin oxides and tantalum oxides. Under indirect synthesis, there are another two pathways ($S^+X^-I^+$) and ($S^-M^+I^-$) involving the association of similarly charged surfactant and inorganic precursor species stabilized using counterions like X^- = Cl^-, Br^- etc. for ($S^+X^-I^+$) and M^+ = Na^+, K^+ etc. for ($S^-M^+I^-$). However, nonionic surfactants follow neutral path routes, viz., S^oI^o and $S^o(IX)^o$, involving either H-bonding or dipolar interactions between the surfactant and the inorganic precursor. Neutral path with S^oI^o was used by Bagshaw et al. (1995) and Prouzet et al. (1997) for synthesizing alumina and disordered worm like mesoporous silica under neutral pH conditions. Besides, the above mentioned pathways, (S^oH^+)(X^-I^+) pathway is used for the synthesis of mesoporous SBA-15 where S^oH^+ being the surfactant hydrogen bonded to a

hydronium ion, X^-: the chloride ion and I^+: the protonated silica. In this mechanism, an association of the cationic silica species occurs with ethylene oxide (EO) units of the block polymer by involving a combination of van der Walls, H-bonding and electrostatic interactions.

$$Si(OEt)_4 + nH_3O^+ \xrightarrow[pH < 2]{\text{hydrolysis}} Si(OEt)_{4-n}.(OH_2^+)_n + nEtOH$$

$$REO_m + {}_yHX \xrightarrow{H_2O} REO_{m\text{-}y}\,[(EO).H_3O^+]_y.....yX^-$$

where R= alkyl poly(propylene oxide), $X = Cl^-, Br^-, I^-, NO_3^-$

This is followed by the silica condensation and the restructuring of the surfactant and inorganic silica species forming hybrid mesoporous framework.

1.2 Transition-metal incorporated SBA-15 nanocomposites

A scientific curiosity due to the recent developments and research in the field of supported transition metal nanocomposites has led to the synthesis of new designer materials and catalysts with superior catalytic activity in comparison to the conventional nanoparticles (NPs). Moreover, the molecular interactions, processes and phenomena involved at the nanoscale to design materials with desired functionalities and physicochemical properties make it all the way more fascinating. However, the presence of highly active centers and high surface energy of the NPs make them thermodynamically unfavorable. Stabilization can be done by capping them with organic (Gavia et al., 2015) or inorganic ligands (Dirin et al., 2014) or by immobilising them on some suitable porous support. A porous support provides an environment that influences the formation, distribution and dispersal of metal species by confining them, thus limiting their particle growth to a particular size and shape. Among various porous supports, mesoporous SBA-15 is the most preferred host, although bare SBA-15 does not exhibit any catalytic activity due to lack of active sites. Thus, the union of porous materials with nanoparticle syntheses has led to the emergence of host-guest chemistry in the form of supported transition metal nanocomposites having a wide range of applications in the field of catalysis (Deng et al., 2010), sensing (Walcarius et al., 2005) and medical diagnosis (Slowing et al., 2007).

1.2.1 Role of SBA-15 as a support: SBA-15 is the most frequently used mesoporous host for the synthesis of supported metal nanocomposites as

1. it possesses tunable pore size and thicker walls that help in the formation of the stable matrix for stabilising the NPs against aggregation within mesochannels.
2. it can adjust the shape and size of encapsulated nanospecies by the confinement imposed by the walls of the support.
3. high surface area and pore volume of the support help in achieving high metal loading with homogeneous metal deposition.
4. the presence of large pores (4-30 nm) and uniform hexagonal structure offers lower diffusion resistance to the solvent and reactant molecules towards the active sites and thereby improves their catalytic efficiency.
5. it mediates the transfer of charge to or from the NPs in the case of reducible oxides as a support.

1.2.2 Various chemical methods being used for the synthesis of supported metal nanocomposites are being described:

1. Incipient Wetness Impregnation (IWI): This method involves the addition of a concentrated solution of the metal precursor to the porous solid support under stirring till the formation of a thick paste. The paste thus formed is dried and calcined resulting in the formation of supported metal nanocomposites. Although high metal loading can be achieved by this method yet it affords a limited control over the NPs size and its distribution due to weak interactions between the metal precursor and the support.

2. Co-precipitation: In this method, precipitation of the metal and the support take place simultaneously. A major drawback associated with this method is that the formation of the NPs hinders the formation of the support structure leading to the formation of ill formed nanostructures.

3. Deposition-precipitation (DP): This method encompasses the formation of metal precursor solution in a minimum amount of solvent followed by pH adjustment till complete precipitation of the metal hydroxide. Finally, the precipitates are deposited on some suitable support and calcined for the reduction of metal precursor to its elemental state. Although, fine NPs can be prepared by this approach yet nanoparticle aggregation cannot be avoided.

4. Microwave irradiation (MWI): Metal NPs are synthesized using MWI as a heating source with reduced preparation time and a narrow particle size distribution.

5. Chemical vapour deposition (CVD): In this technique, the growth of the supported metal nanostructure occurs by conversion of metal to its vaporised form in high vacuum under the influence of an excess of stabilising agent (THF, alkenes) or reducing agent (H_2). Although metal NPs with narrow size distribution can be obtained yet the cost of the instrument and mass transfer limited kinetics are the major drawbacks associated with the method.

6. Pulsed laser ablation (PLA): It involves the conversion of metal to its vaporised form using a pulse laser (eg: Nd-YAG) under particular conditions of temperature and pressure. It helps in establishing a control over the metal NPs which are deposited on a support without involving the use of any chemical precursors and solvent.

7. pH assisted delay-addition method (PDA): It involves the addition of a Al precursor to a pH adjusted solution containing preformed hierarchically and radially mesoporous (HRM) nanostructures via a hydrothermal treatment followed by a second hydrothermal treatment to introduce heteroatoms into the silica framework, resulting in the maintenance of the unique structure with acidic properties (Sika Yun et al., 2014).

8. Mechanochemical synthesis (MCS): The method involves dry-mixing of a metal precursor salt (e.g., metal acetate) with a support (e.g. carbon nanotubes) followed by heating in an inert atmosphere in the absence of any solvent, reducing agent or electric current. As inert atmosphere sublimes the metal acetates before decomposing resulting in their autoreduction directing nanoparticle sizes as well as their interaction with the support. For e.g., Ag nanoparticle-decorated carbon nanotubes (Xu et al., 2015).

9. Vapor infiltration process (VIP): In this method, the support is immersed into the aq. solution of metal precursor under reduced pressure to incorporate metal species into support through capillary force. Then, the mesoporous-metal powder is placed in a closed container with a reducing agent under atmosphere to reduce the metal species (Takai et al., 2010).

The applications of these methods for the supported Au, Ag and CuO nanocomposites are being described:

1.2.3 Supported Au nanocomposites

For many years, Au was considered to be inert till the exciting discovery made by Haruta et al. (1987) and Hutchings et al. (1985) that revolutionized the field of catalysis on Au based catalysts. Although bulk Au is unreactive yet on the contrary, Au in the nanocrystalline

form or Au supported on porous framework revealed unprecedently high chemical reactivity owing to its high surface area to volume ratio, exhibiting wide applications in the field of catalysis, gas sensors, nano electronic/optical devices and medical diagnosis (Campelo et al., 2009). Thus, Au catalysis has become a fascinating topic of research today which is illustrated by an exponential increase in the number of publications based on numerous applications of supported Au catalysts. The high activity of the Au catalysts is governed by factors such as preparation methods, shape and size of Au NPs, nature of the support, metal-support interactions as well as the oxidation state of the Au incorporated over the support (Zheng et al., 2006). Recent reports for the synthesis of supported Au catalysts by different methods have been compiled in Table 1.1 and discussed below.

1. Deposition-precipitation (DP): Initially, this method showed limited applicability for supports with high IEP ~ TiO_2, Al_2O_3 and CeO_2 (Ma et al., 2008) and was assumed to be inappropriate for supports like SiO_2 having low IEP ~ 2 as these supports involve an adjustment of pH to high value for complete precipitation of the metal hydroxide. Moreover, at high pH, the siliceous surface develops negative charge leading to aggregation of Au NPs due to electrostatic repulsion between negatively charged siliceous surface and $[Au(OH)_nCl_{4-n}]^-$ species (Hutchings et al., 2005). But there are reports of Au loaded SBA-15 nanocomposites prepared by DP method. Initially, Liu et al. (2007) reported the formation of Au/SBA-15 nanocomposites by DP method resulting in larger Au aggregates (10-15 nm) on the outer surface of the silica host. Ma et al. (2009) prepared Au/SBA-15 catalysts by grafting and DP method and reported that the synthesized catalysts by DP method showed lower catalytic activity for the oxidation of benzyl alcohol in comparison to grafting method. This was attributed to the formation of large sized Au NPs (size ~10-50 nm) on the intra surface of SBA-15 in comparison to small sized (10 nm) and uniformly dispersed spherical Au NPs within the pores of SBA-15 prepared by grafting method. However, the problem of nanoparticle aggregation was circumvented by either modifying the siliceous surface or metal oxide with functional groups. Following this, Liu et al. (2009) synthesized Au clusters (~1 nm) within the mesoporous channels by depositing triphenylphosphine protected Au precursor on the siliceous surface in an organic medium that showed high catalytic activity for alcohol oxidation. Similarly, Ovoshchnikov et al. (2014) also used triphenylphosphine protected Au precursor for preparing Au nanostructures supported on various oxides for catalysing the solventless oxidation of cyclohexene. Recently Shu et al. (2015)

prepared silica supported cationic Au (I) complex as the heterogeneous catalyst that showed high regio and enantioselectivity for lactonisation reactions. Binder et al. (2013) also synthesized highly stable Au incorporated SBA-15 catalyst prepared by deposition of Au precursor on surface modified SBA-15 support that demonstrated high catalytic activity for CO oxidation.

2. Direct synthesis/Co-condensation/One pot method: This method involves simultaneous mixing of all the reagents that helps in bringing about the homogeneous dispersion of metallic nanospecies throughout the mesoporous support. A variety of supports has been used for the preparation of supported Au nanocatalysts using one pot method. Selvakannan et al. (2013) reported the formation of high surface area Au/SBA-15 nanomaterials through direct synthesis by utilising amino acid tryptophan that played a dual role of co-structure directing agent as well as reducing agent for Au ions to form Au NPs within SBA-15. Wu et al. (2010) synthesized Au supported SBA-15 nanocomposites (size ~5 nm) by one pot method using vinyltriethoxysilane (VTES) as functionalising agent for modification of the silica surface. The functionalising agent acted as a stabiliser by improving the interaction between Au NPs and the silica support resulting in a uniform dispersion of Au nanospecies all over the SBA-15 surface. The prepared materials showed high catalytic activity for the selective oxidation of cyclohexane using molecular oxygen with conversion above ~21 % and 95 % selectivity towards cyclohexanol and cyclohexanone respectively. Sekhar et al. (2012) reported a simple one pot strategy for synthesising Au incorporated mesoporous silica nanocomposites without utilising any functionalising agents or linkers. Though the nanocomposites showed poor catalytic activity for the oxidation reactions, however, they became exceptionally active with 100 % conversion after mild H_2 reduction at 100 ^{o}C.

3. Incipient Wetness Impregnation (IWI): A major part of the recent research and developments on supported metal nanocomposites is based on this method. Wu et al. (2010) employed IWI to prepare Au catalyst supported on SBA-15 having surface modified with VTES for the cyclohexane oxidation. It was observed that with Au impregnation, large Au NPs (~9 nm) were formed resulting in slight disruption of the mesoporous structure. El-Sheikh et al. (2013) prepared Au/SBA-15 nanocomposites (~10 nm) by IWI method using H_2 or sodium citrate as reducing agent that displayed high catalytic efficiency for the reduction of *p*-nitrophenol.

4. Ion exchange method: Fattori et al. (2012) used ion-exchange method for the preparation of Au NPs (~1.5-4.7 nm) within the channels of surface modified SBA-15. Initially, the surface of SBA-15 was modified with imidazolium alkoxysilane and then $AuCl_4^-$ anions were exchanged on its surface. The solid SBA-15/$R^+AuCl_4^-$ thus formed was filtered, washed with distilled water and finally reduced with $NaBH_4$ leading to the formation of Au NPs within SBA-15.

5. Chemical vapour deposition (CVD): There are reports (Schimpf et al., 2002; Okmura et al., 2003) showing the formation of Au NPs over different mesporous supports using CVD for catalysing different chemical reactions.

6. Au/SBA-15 nanocomposites using $[Au(en)_2]Cl_3$ (en = ethylenediamine): Au loaded mesoporous silica nanostructures have been prepared by using cationic Au complexes. Schunemann et al. (2015) reported the preparation of Au complex by addition of organic functional ligand to the aqueous solution of Au precursor that was then deposited on silica surface by adjusting pH to10 and reduction under H_2, leading to the formation of Au/mesoporous silica nanocomposites. Similarly, Au/SBA-15 catalysts (Yin et al., 2010) have been synthesized by utilizing cationic Au complex for catalyzing CO oxidation.

Table 1.1 Characteristics and catalytic applications of Au supported SBA-15 nanocomposites

Metal	Support	Size (nm)	Method	Application	Ref.
Au	SBA-15	10-15	Deposition-precipitation	----	Liu et al. (2007)
Au	SBA-15	10-50	Deposition-precipitation	Oxidation of benzyl alcohol	Ma et al. (2009)
Au	SBA-15	~1	Deposition-precipitation	Alcohol oxidation	Liu et al. (2009)
Au	SiO_2, TiO_2, WO_3	~4-10	Deposition-precipitation	Oxidation of cyclohexene	Ovoshchnikov et al. (2014)
Au	SBA-15	----	One pot method	Lactonisation reaction	Shu et al. (2015)
Au	SBA-15	~ 3-4	Deposition-precipitation	CO oxidation	Binder et al. (2013)
Au	SBA-15	----	One pot method	----	Selvakannan et al. (2013)
Au	SBA-15	~5 ~9	One pot method Impregnation	Oxidation of cyclohexane	Wu et al. (2010)

Au	SiO_2	~2-4	One pot method	Oxidation of benzyl alcohol, CO oxidation	Sekhar et al. (2012)
Au	SBA-15	10	Impregnation	Reduction of p-nitrophenol	El-Sheikh et al.(2013)
Au	SBA-15	1.5-4.7	Ion exchange	----	Fattori et al. (2012)
Au	SiO_2	~6	Chemical vapor deposition	CO oxidation	Okmura et al. (2003)
Au	SiO_2	----	Chemical vapor deposition	CO oxidation	Schimpf et al. (2002)
Au	SBA-15 KIT-6 MCM-41	~2	Using cationic Au complex	Glycerol oxidation	Schunemann et al. (2015)
Au	SBA-15	2-4	Using cationic Au complex	CO oxidation	Yin et al. (2010)
Au	CeO_2-SBA-15	2-5	Doping oxides	CO oxidation	Ren et al. (2012)
Au	CeO_2-SBA-15	~5	Doping oxides	Liquid phase oxidation of benzyl alcohol	Wang et al. (2015)
Au	Co_3O_4-SBA-15	~1-3	Doping oxides	CO oxidation	Ma et al. (2012)
Au	SBA-15	~5-10	Microwave irradiation	----	Gu et al. (2008)

7. Au/SBA-15 synthesis by doping oxides: There are reports of supported Au nanocomposites prepared by doping different metal oxides like CeO_2, TiO_2 on the mesoporous supports. Preloading of metal oxide on the siliceous support helped in improving the interaction between the support and the introduced Au NPs, thus leading to enhanced dispersion and catalytic efficiency of supported Au nanostructures. Ren et al. (2012) prepared Au loaded SBA-15 catalysts by doping mesoporous host with CeO_2 for catalyzing CO oxidation. Although pure Ceria was considered as an active support for oxidation reactions yet Au NPs incorporated over the support were found to be unstable. In order to circumvent this problem, three component nanocatalysts was prepared that showed better chemical reactivity as compared to bare supports. Similar findings have been reported elsewhere (Ma et al., 2012; Wang et al., 2015).

8. Microwave irradiation (MWI): Gu et al. (2008) designed uniformly distributed Au NPs within channels of mesoporous SBA-15 by MWI technique. The average size of the NPs varied

between ~5-10 nm ascribed to the fast nucleation, propagation and termination of Au precursor by MWI.

1.2.4 Supported Ag nanocomposites

Like Au loaded mesoporous nanocomposites, Ag also displayed high chemical reactivity due to fascinating physical and chemical properties and high surface energy. However, being easily susceptible to oxidation it undergoes aggregation (during the reaction process) resulting in decay of catalytic activity. Hence, in order to achieve high catalytic efficiency, it is necessary to stabilize Ag NPs which can be achieved by immobilizing and stabilizing metal NPs on some suitable porous support that has prompted massive research on supported Ag nanomaterials. Efforts have been made for synthesizing Ag incorporated mesoporous silica nanostructures by various methods (Table 1.2). Ma et al. (2014) synthesized Ag/SBA-15 nanocomposites by varying the Ag loading (4-16 %) using IWI method. Of all the prepared nanocomposites, a catalyst with 5.1 % Ag loading showed highest catalytic activity with 94 % conversion and 97 % selectivity for oxidation of benzyl alcohol to benzaldehyde. A series of monometallic transition metal (M = Cu, Co, Pt, Pd, Ag, Fe, V and Mn) loaded SBA-15 nanocomposites were also synthesized (Zhang et al., 2014b) involving IWI method for catalytic combustion of acetonitrile. The catalytic performance of the catalysts was influenced by their redox ability as well as chemical nature of the incorporated metal within silica host. Various other reports based upon IWI method includes the comparative study of adsorption and oxidation of formaldehyde (HCHO) catalysed by Ag loaded nanocomposites (Chen et al., 2011) on different supports (MCM-41, NaY, titania, SiO_2, SBA-15 and zeolites). Among various catalysts, Ag/SiO_2 catalysts exhibited best surface reaction activity for HCHO oxidation owing to the presence of varying oxidation states of Ag species (Ag^o, Ag^+, Ag_2O and $Ag_n^{\delta+}$ clusters) on different supports. Naik et al. (2011) reported varying morphologies of SBA-15 supported Ag NPs by using 5 and 10 wt. % Ag impregnation without involving any precomplexation of Ag ions or surface modification of silica surface for the reduction of *p*-nitrophenol. Besides Ag/SBA-15 nanocomposites, there have been reports of supported Ag nanostructures based on different supports including the synthesis of Ag/HMS catalysts by one pot method (Jia et al., 2012) with varied Ag loading (0.55-3.5 wt. %) for catalysing the gas phase oxidation of benzyl alcohol to benzaldehyde. It was observed that catalyst with intermediate (2.81 wt. %) Ag loading revealed the best catalytic activity with 100 % conversion and 96% selectivity towards benzaldehyde. Likewise, Han et al. (2012) reported

the formation of Ag/SBA-15 nanocomposites by one pot method utilizing aniline as reducing agent and exhibiting improved catalytic activity for *p*-nitrophenol reduction. Yin et al. (2011) reported the formation of Ag/MCM-41 catalytic systems by employing DP method and showed that catalyst with 10 wt. % Ag loading was catalytically most effective for gas phase hydrogenation of dimethyl oxalate to methyl glycolate and ethylene glycol. Apart from conventional synthetic methods, a new range of techniques has been employed for controlled deposition of metals on the support. Szegedi et al. (2014) reported the formation of Ag nanoparticle loaded mesoporous silica nanostructures by the use of PLA method and compared it with other chemical methods. It was observed that smaller and uniformly distributed Ag NPs were effectively obtained within the mesochannels of the host by PLA method showing high catalytic activity for the oxidation of toluene. Fuku et al. (2013) employed microwave assisted alcohol reduction method for the formation of highly dispersed Ag nanospheres (~4 nm) and nanorods (~9 nm in diameter) within the channels of SBA-15. Zienkiewicz-Strzalka et al. (2013) reported an efficient approach for the synthesis of Ag nanostructures (nanospheres ~4 nm and nanowires ~50 nm depending on Ag loading) supported on mesoporous silica with controlled morphology and composition using tollen's reagent as Ag source. Zhang et al. (2011) employed pH adjusting method for preparing Ag NPs within the SBA-15 host for catalyzing CO oxidation.

Table 1.2 Characteristics and catalytic applications of Ag supported SBA-15 nanocomposites

Metal	Support	Loading (wt. %)	Size (nm)	Method	Application	Ref.
Ag	SBA-15	4.1-16.5	~6	Impregnation	Gas phase selective Oxidation of benzyl alcohol to benzaldehyde	Ma et al. (2014)
Ag	SBA-15	~2	~5-6	Impregnation	Combustion of acetonitrile	Zhang et al. (2014b)
Ag	SBA-15, HMS, SiO_2, TiO_2	8	2-10	Impregnation	Oxidation of formaldehyde	Chen et al. (2011)
Ag	SBA-15	5 and10	~7	Impregnation	Reduction of p-nitrophenol	Naik et al. (2011)
Ag	HMS	0.5-3.5	~5-32	One pot	Oxidation of benzyl	Jia et al.

				method	alcohol to benzaldehyde	(2012)
Ag	SBA-15	0.2-0.7	~15	One pot method	Reduction of p-nitrophenol	Han et al. (2012)
Ag	MCM-41	3-20	~10	Deposition-precipitation	Gas phase hydrogenation of dimethyloxalate	Yin et al. (2011)
Ag	SBA-15	5 and 8	5-50	Pulsed laser ablation	Toluene oxidation	Szegedi et al. (2014)
Ag	SBA-15	----	~4	Microwave assisted alcohol reduction	H_2 production from ammonia borane ($NH_3.BH_{3)}$	Fuku et al. (2013)
Ag	SBA-15	----	~4-50	Various methods	----	Zienkiewicz -Strzalka et al. (2013)
Ag	SBA-15	7.86	----	pH adjusting method	CO oxidation	Zhang et al. (2011)
Ag	SBA-15	0.75-2	5-20	Double solvent method	Oxidation of styrene	Huang et al. (2011)
Ag	Monolithic silica	33	----	Two pot method	Separation of hydrocarbons	Zhu et al. (2013)

The pH played a significant role in the Ag content and the oxidation state of species, ultimately affecting the catalytic efficiency of Ag/SBA-15 nanocomposites. Huang et al. (2011) used a double solvent technique for forming Ag nanostructures (nanospheres and nanowires) within and on the external surface of the channels of mesoporous silica by using hydrophobic n-hexane and aqueous silver nitrite as hydrophilic solvent. It was observed that the prepared composites demonstrated high selectivity (59 %) for oxidation of styrene to styrene oxide. Zhu et al. (2013) introduced Ag NPs into porous monolithic silica columns having well defined macropores and SBA-15 mesopores using ethanol as reducing agent. It was found that the column with 30 wt. % Ag loading exhibited a difference in retention time that was large enough for the separation of aromatic hydrocarbons like benzene, naphalene, anthracene and phenanthrene.

1.2.5 Supported Cu/CuO nanocomposites

As discussed in the previous sections, a large amount of research has been dedicated towards the development of Au and Ag NPs incorporated in mesoporous silica but their high cost bounds their industrial applicability. Compared with noble metals, Cu/CuO have also shown the capacity

as redox catalysts (Table 1.3). They are relatively cheap, easily accessible and exhibit exceptional electrochemical and catalytic properties. But Cu is prone to oxidation and CuO undergoes aggregation at high thermal treatment. However, they can be stabilized by capping with PVP (Polyvinyl pyrollidone) but that hampers the access of reactant molecules to the active sites resulting in decreased catalytic activity. These reasons prompted studies that triggered research for the development of supported Cu/CuO nanomaterials by exploiting different chemical routes (Table 1.3). Recently, Wang et al. (2014) prepared Cu/SBA-15 nanocomposites by different chemical routes and compared their catalytic efficiency for gas phase hydrogenation of methyl acetate (MA). Of the various catalysts, Cu/SBA-15 produced by homogeneous deposition- precipitation (HDP) method displayed highest catalytic performance on the basis of small particle size and the synergistic effect between Cu^{o} and Cu^{+} species with 99.5 % MA conversion and 99.5 % ethanol selectivity for MA hydrogenation under benign reaction conditions. In another report, vapor phase hydrogenation of furfuryl has been studied (Vargas-Hernandez et al., 2014) by preparing a series of Cu supported SBA-15 catalysts by impregnating 7.8-20.2 wt. % of Cu on a preformed silica support. It was observed that Cu/SBA-15 catalysts evidenced higher furfuryl conversion (54 mol %) and furfuryl alcohol selectivity (95 mol %) at the low reaction temperature (170 ^{o}C) with high catalyst wt. (15 wt. %) and low furfuryl feed. However, Chen et al. (2013) successfully produced very fine Cu NPs (2-6 nm) within the channels of SBA-15 having functionalized surface with a carboxylic acid using 7-25 wt. % of Cu loading. It was observed that Cu/SBA-15 with higher Cu loading of 7.6 and 11.9 wt. % created an abundant number of active sites that led to the high catalytic efficiency for water gas shift reaction. Other reports of fabrication of Cu/SBA-15 (Subbaramaiah et al. 2013; Ghosh et al. 2015; Harisekhar et al. 2014; Mondal et al. 2013) catalyst by conventional impregnation route are also available. However, Zhang et al. (2012) employed one pot direct method for synthesizing highly dispersed Cu NPs within mesochannels of SBA-15. The prepared materials showed highest rate (Turn over frequency TOF ~130.6 h^{-1}) of phenol hydroxylation in comparison to other reported conventional catalysts with highest phenol conversion (49.7 %), selectivity (55.1 %) and yield (27.4 %) of diphenol. Gu et al. (2011) synthesised Cu/SBA-15 nanomaterials by one pot method that showed exceptionally enhanced catalytic activity for cyclohexane oxidation, with an increase in conversion to about 11 % and cyclohexanol to cyclohexanone selectivity of ~80 %. Chen et al. (2009) also synthesized Cu/SBA-15 catalysts

using different chemical routes for catalyzing the hydrogenolysis of dimethyl maleate to 1-4 butanediol (BDO). Of various methods employed, the catalyst prepared by HDP method displayed 100 % conversion and highest selectivity (44.1 %) to BDO that attributed to the cooperative effect between various Cu (Cu^o and Cu^+) species in the catalyst. With a view to understanding the physicochemical differences between various analogues of Cu as catalysts towards chemical kinetics of the reaction, many reports are associated with the synthesis, characterisation and catalytic evaluation of supported CuO nanocomposites. Kong et al. (2009) proposed one pot direct method for the formation of CuO loaded hexagonal and cubic mesoporous silica (SBA-15 and KIT-6) with very high Cu loading (34-45 wt. %) for evaluating hydroxylation of benzene to phenol. The prepared catalysts showed improved catalytic activity in comparison to conventional impregnation methods. However, leaching of the Cu during successive recycles was a major concern. Patel et al. (2011) reported the synthesis of CuO/SBA-15 catalysts by impregnation method for catalytic reduction of NO by CO. Petre et al. (2013) studied the catalytic and non-catalytic ozonation of two refractory by-products, oxalic and mesoxalic acids by synthesizing CuO (~33 nm) supported mesoporous solid SBA-15 by impregnation method. Zhong et al. (2012) also prepared mesoporous silica supported CuO NPs by impregnation of aqueous copper nitrate on the preformed support using glycine as a complexing agent. The prepared copper-silica composites demonstrated high catalytic activity

Table 1.3 Characteristics and catalytic applications of Cu/CuO supported SBA-15 nanocomposites

Metal/ Metal oxide	Support	Loading (wt. %)	Size (nm)	Method	Application	Ref.
Cu	SBA-15	~17-18	~31-41	Various methods	Methyl acetate hydrogenation for ethanol production	Wang et al. (2014)
Cu	SBA-15	7.8-20	~35	Impregnation	Furfuryl alcohol from furfuryl hydrogenation	Hernandez et al. (2014)
Cu	SBA-15	7.6-25.2	2-6	Impregnation	Water gas shift reaction	Chen et al. (2013)
Cu	SBA-15	5, 10 and 20	------	Impregnation	Wet peroxidation of picoline	Subbaramaiah et al. (2013)
Cu	SBA-15	2.5-15	5-8	Impregnation	Reduction of dyes	Ghosh et al. (2015)

Cu	SBA-15	2.5-20	5-20	Impregnation	Vapour phase hydrogenolysis of glycerol	Harisekhar et al. (2014)
Cu	SBA-15	------	------	Impregnation	Cross coupling reaction	Mondal et al. (2013)
Cu	SBA-15	------	------	One pot method	Phenol hydroxylation	Zhang et al. (2012)
Cu	SBA-15	0.19-0.85	------	One pot method	Cyclohexane oxidation	Gu et al. (2011)
Cu	SBA-15	------	------	Various methods	hydrogenolysis of dimethyl maleate	Chen et al. (2009)
CuO	SBA-15	34-45	------	One pot method	Hydroxylation of benzene	Kong et al. (2009)
CuO	SBA-15	4, 8 and 10.1	------	Impregnation	Catalytic reduction of NO by CO	Patel et al. (2011)
CuO	SBA-15	4-10	~10	In-situ Auto combustion method	Catalytic wet peroxide oxidation of phenol	Zhong et al. (2012)
CuO	SBA-15	2.1-13.4	------	Ultrasonic post grafting treatment	Direct hydroxylation of benzene to phenol	Zhang et al. (2013)
CuO	SBA-15	8.3	~33	Impregnation	Heterogeneous ozonation	Petre et al. (2013)

for wet peroxide oxidation (WPO) of phenol that was related to Cu accessible active sites and Cu loading. Zhang et al. (2013) employed ultrasonic post grafting method for loading highly dispersed CuO within mesochannels of SBA-15 for catalyzing the direct hydroxylation of benzene to phenol. The catalyst showed optimum benzene conversion (28 %) and selectivity (95 %) for phenol with high stability and reusability.

1.2.6 Supported bimetallic Au-Ag nanocomposites

Advancement and development in the field of supported monometallic nanocomposites have led to the emergence of a new type of catalytic systems which is formed by mixing of two different metals within the same host viz., supported bimetallic or alloy nanostructures (Lin et al., 2001). These bimetallic nanocomposites exhibit unique electronic, magnetic and catalytic properties, different from those of their monometallic counterparts (Zheng et al., 2013) due to the synergistic effect between the two metals. The synergism arises due to the alloy formation that

leads to some electronic and geometric modifications (Wang et al., 2013) within the catalytic systems resulting in enhanced selectivity, stability and catalytic activity (Ferrando et al., 2008). Consequently, there has been an exponential increase in the publications based on supported bimetallic catalysts for a number of reactions such as hydrogen production (Carrero et al., 2007), hydrogenation of unsaturated aldehydes (Ungureanu et al., 2011) and N_2O decomposition (Wei et al., 2012). Among the various supported bimetallic nanostructures, the coinage metal systems such as Au-Ag (Liu et al., 2008; Nagy et al., 2014; Qu et al., 2013; Yen et al., 2009), Au-Cu ((Li et al., 2012; Della-Pina et al., 2008) and Ag-Cu (Czaplinska et al., 2014; Wang et al., 2012a) are widely studied. Even though these metals belong to the same group and have similar chemistries yet they show different catalytic activity. Moreover, the synthesis of bimetallic nanocatalyst is determined by the uniformity in particle shape, size, chemical composition, and structure. Since Au is miscible with Ag, it forms homogeneous bimetallic nanocatalysts with Ag in contrast to other transition metals. The bimetallic nanocomposites are prepared primarily by one pot method which involves the formation of bimetallic NPs in solution and then their deposition on the mesoporous support while the two pot method involves the deposition of two metal precursors on the support followed by co-reduction or sequential reduction. Although one pot method offers control over the shape and size of the particles deposited on the support yet their shape, size and chemical composition changes drastically. Moreover, sintering of the metallic NPs cannot be avoided at high temperature. On the other hand, highly stable, small sized NPs can be achieved by two pot method but the homogeneous distribution of bimetallic NPs is still a challenge. Several recent reports on Au supported bimetallic catalysts catalyzing a variety of reactions are summarized in Table 1.4. Mou's group (Lin et al., 2001) prepared bimetallic Au-Ag nanocomposites with MCM-41 as support using one pot method for catalyzing low temperature

Table 1.4 Characteristics and catalytic applications of supported bimetallic Au-Ag nanocomposites

Metal	Support	Size (nm)	Reaction	Method	Ref.
Au-Ag	MCM-41	20-30	CO oxidation	One -pot method	Lin et al. (2001)
Au-Ag	MCM-41	4-6	CO oxidation	Two-pot method	Yen et al. (2009)
Au-Ag	SBA-15	3.3-3.4	CO oxidation	Two-pot method	Liu et al. (2008)
Au-Ag	SBA-15	3-4	Hydrogenation of	Two-pot method	Zheng et al.

			esters		(2013)
Au-Ag	SBA-15	<7	CO oxidation	Two pot method	Qu et al. (2013)
Au-Ag	SiO_2	3-5	Oxidation of benzyl alcohol, glucose and CO oxidation	-----	Nagy et al. (2014)
Au-Cu	SiO_2	------	Oxidation of benzyl alcohol	Two-pot method	Pina et al. (2008)
Au-Cu	SBA-15	~3.7	Low temperature preferential oxidation (PROX) reaction	Two-pot method	Li et al. (2012)
Ag-Cu	SBA-15	-----	Methanol oxidation	Two-pot method	Wang et al. (2012)
Ag-Cu	alumina	Small and highly dispersed	Styrene oxidation	Microemulsion	Czaplinska et al. (2014)
Au-Pd	SBA-15	~5	Oxidation of benzyl alcohol	Two-pot method	Ma et al. (2009)
Au-Pd	SBA-15	2	N_2O decomposition	Two-pot method	Wei et al. (2012)

CO oxidation. The synthetic procedure involved the formation of Au-Ag bimetallic NPs with an average size of ~4.5 nm by co-reduction of aqueous solution of $HAuCl_4$ and $AgNO_3$ using CTAB that exhibited a dual role of stabilizing as well as structure directing agent. The bimetallic catalyst was found to be inactive for CO oxidation due to passivity offered by the CTAB present over the Au NPs surface. Moreover, the surfactant (CTAB) upon removal by calcination resulted in abrupt increase in the average size of the supported bimetallic Au-Ag NPs from ~4.5 nm to 20 nm, attributed to the sintering of Ag NPs leading to the formation of AgBr. However, the catalyst upon treatment with H_2 the catalyst became outstandingly active. Hence, bimetallic Au-Ag catalysts showed higher activity in comparison to their catalytically inactive (at room temperature) monometallic Au or Ag counterparts supported on MCM-41. However, in order to avoid sintering of the NPs during the activation step, two step method was developed (Liu et al., 2009). Though this method prevented aggregation of the embedded bimetallic NPs, uniform dispersal of the nanospecies within the mesoporous support remained a challenge which

completely relied on the metal support interaction. So, for achieving strong metal support interaction, surface modification of the support with organic groups (such as amines) either during synthesis (Guteirraz et al., 2011) or by post grafting (Chi et al., 2005) was carried out that resulted in the strong interaction between metal and the support, thus leading to better dispersal of Au NPs. It was achieved with $HAuCl_4$ followed by its reduction with $NaBH_4$ forming small and uniformly distributed Au NPs. Similarly, reduction of $AgNO_3$ was done for depositing Ag NPs on the Au loaded mesoporous host. Before Ag deposition, a thorough washing was done to remove the Cl^- ions (from Au surface or support) that may result in the sintering of Ag to AgCl. Amine was removed by calcination followed by reduction with H_2, resulting in the formation of supported Au-Ag alloy. Supported bimetallic Au-Ag catalysts prepared by two-step method appeared slightly more active for CO oxidation in comparison to the catalysts prepared by one step method (Yen et al., 2009). In addition to Au-Ag, other bimetallic Au systems like Au-Cu also displayed higher activity for low temperature CO oxidation but to a lesser extent in comparison to Ag (Liu et al., 2009). Besides CO oxidation, Au bimetallic systems have also been used for other oxidation as well as hydrogenation reactions. Like Au-Cu exhibited high catalytic activity and stability for the oxidation of benzyl alcohol to benzaldehyde (Pina et al., 2008) and selective hydrogenation of dimethyl oxalate to methyl glycolate and ethylene glycol (Wang et al., 2012b). Recently, Soule et al. (2011) prepared Au-Co supported nanocomposites that displayed improved selectivity and activity for the synthesis of amide from alcohols and amines Similarly, Au-Pt supported on various supports (silica, carbon and alumina) exhibited enhanced catalytic activity for the chemoselective hydrogenation of cinnamaldehyde to hydrocinnamaldehyde (Hong et al., 2011). Since Au is miscible with Pd in all compositions, Au-Pd nanoalloy also demonstrated higher catalytic activity for the oxidation of benzyl alcohol (Ma et al., 2009), selective hydrogenation of butadiene (El-Kolli et al., 2013) and *p*-chloronitrobenzene (Cardenas-Lizana et al., 2009).

1.2.7 Research gaps

Based on literature survey, following research gaps were identified:

1. Metal NPs confined in SBA-15 possess high catalytic activity because they are free of stabilizer and are confined, so there is a need to evaluate transition metal supported over other mesoporous materials as heterogeneous catalysts.

2. Metal NPs of different shapes have different crystallographic facets and have a different fraction of surface atoms on their corners and edges. So, more work needs to be done in this area as there have been only a few studies showing the shape and size dependent synthesis of transition metal inside the mesoporous sieves.

3. Major difficulties involved with the reported methods of preparation are the uncontrolled growth of metal NPs resulting in their agglomeration and the low amount of loading that restricts the catalytic efficiency of supported transition-metal nanocomposites. So, synthesis of well dispersed supported metal/metal oxide catalysts with high catalytic efficiency even at higher metal loading, by a simple, sustainable process involving green chemistry credentials is still a challenge.

4. The nature, as well as the oxidation state of the metal/metal-oxide incorporated over the support, have a significant effect on the kinetics of the reaction owing to the difference in their metal/support interaction/ adsorption behavior with the substrate. So, it is valuable to investigate the comparative catalytic influence of supported transition metal (Au, Ag, Cu) nanocomposites on the reaction rate to know the catalytic efficiency of the incorporated metals.

1.2.8 Objectives

- To optimize pore and surface structures of mesoporous materials (SBA-15, HMS, MCM-48 etc.)
- Preparation of transition metal NPs (Au, Ag etc.) and study of their incorporation into the mesoporous materials
- To investigate the catalytic activities of as synthesized materials for certain industrial reactions

1.3 Experimental section

1.3.1 Chemicals

Pluronic (M.W. 5800, $EO_{20}.PO_{70}.EO_{20}$), tetraethoxysilane (TEOS), hydrogen tetrachloroaurate ($HAuCl_4.3H_2O$, 99.99%), silver nitrate ($AgNO_3$, 99.0%), copper chloride ($CuCl_2.2H_2O$), copper nitrate [$Cu(NO_3)_2 .3H_2O$], sodium borohydride ($NaBH_4$), 3-aminopropyltriethoxysilane (APTES), 3-aminopropyltrimethoxysilane (APTMS), *m*-dinitrobenzene (*m*-DNB), *m*-phenylenediamine (*m*-PDA), *m*-nitroaniline (*m*-NA) were obtained from Sigma Aldrich. Aniline

(AN), *m*-chloronitrobenzene (*m*-CNB), *m*-chloronitroaniline (*m*-CAN), *m*-nitrotoluene (*m*-NT), *m*-aminotoluene (*m*-AT), *p*-dinitrobenzene (*p*-DNB), *p*-nitrophenol (*p*-NP), *p*-aminophenol (*p*-AP), *p*-phenylenediamine (*p*-PDA), *p*-nitroaniline (*p*-NA), ethanol (C_2H_5OH), methanol (CH_3OH), hydrochloric acid (HCl) were obtained from Loba Chemie, India and were used as received without further purification. Ultra-pure deionized water with (Milli-*Q*, Millipore) was used throughout all the experiments.

1.3.2 Preparation of mesoporous SBA-15

Mesoporous silica was prepared by reported method (Zhao et al., 1998) using nonionic triblock copolymer surfactant $EO_{20}PO_{70}EO_{20}$ (P123) as surface directing agent. In a typical synthesis, 2 g of nonionic triblock copolymer surfactant $EO_{20}PO_{70}EO_{20}$ (P123) was dispersed in 60 ml of 2M HCl under stirring at 40 °C until a clear solution was obtained. Then, 0.025 mol of TEOS were added to the above solution and the contents were stirred for 24h at 40 °C, transferred into an autoclave and aged at 95 °C for 72h. The suspension, thus obtained was filtered, dried at 60 °C and finally calcined at 550 °C for 8h resulting in SBA-15. For the synthesis of various mono as well as bimetallic materials, different samples of SBA-15 were prepared with the above reported procedure as a reference.

1.3.3 Surface modification of SBA-15

2 g of prepared SBA-15 was suspended in 100 ml of 2 wt. % of an ethanolic solution of APTES/APTMS under stirring for 3h to modify its surface. It was filtered, washed with ethanol, dried at 60^o C and was designated as ap-SBA-15.

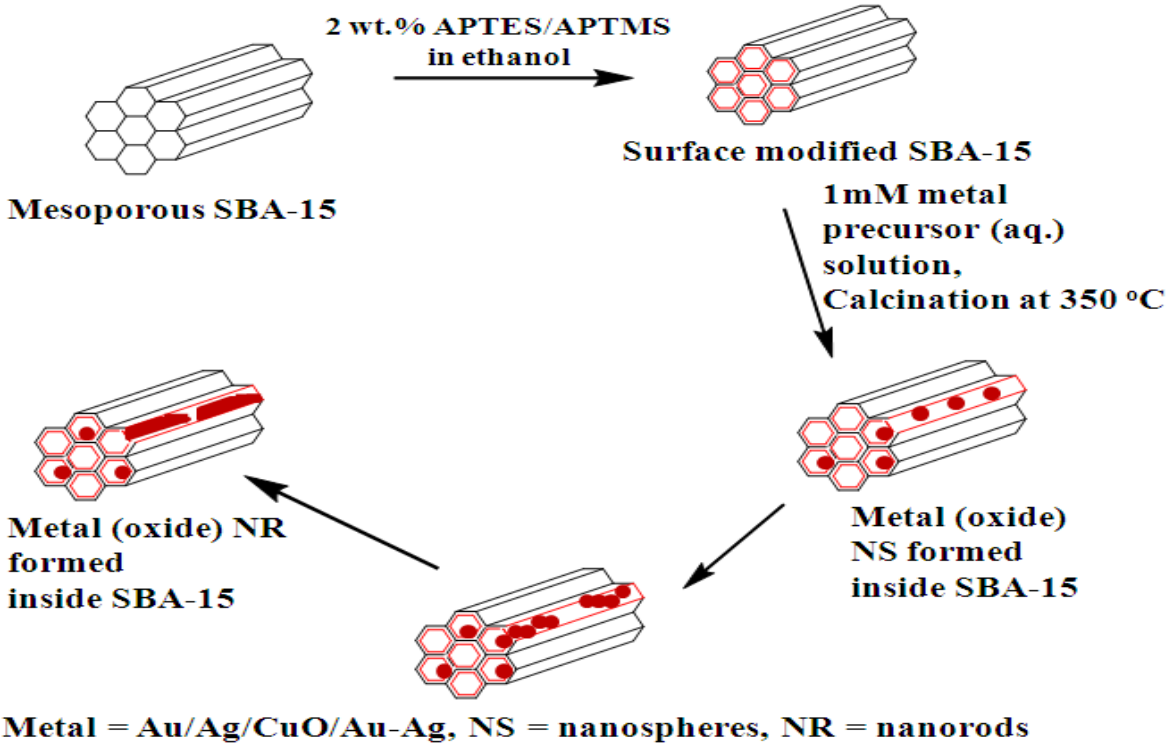

Scheme 1.1 Synthetic procedure for the formation of noble metal (Au, Ag and Cu) incorporated mesoporous SBA-15 catalysts.

1.3.4 Synthesis of M/ap-SBA-15 nanocomposites

The metal Au/Ag/CuO (1-5 wt. % and 10 wt. %) were incorporated in SBA-15 channels via wet-impregnation method (Scheme 1.1). For this purpose, 1 g of ap-SBA-15 was impregnated with an appropriate quantity of 1 mM metal precursor ($HAuCl_4 \cdot 3H_2O$, $AgNO_3$ and $Cu(NO_3)_2 \cdot 3H_2O$) solution. For the preparation of (1-5 and 10 wt. %), Au loaded SBA-15 composites, 50.7 ml, 101.4 ml, 152.1 ml, 202.8 ml, 253.5 ml and 507 ml of 1 mM $HAuCl_4 \cdot 3H_2O$ (aq.) solution was stirred with 1 g of ap-SBA-15 for 2h. The resulting solid was filtered, washed with deionized water and calcined at 350°C for 3h. Similarly, Ag and CuO loaded SBA-15 composites were synthesized by mixing 92.7 ml, 185.4 ml, 278.1 ml, 370.8 ml, 463.5 ml and 927 ml of 1mM $AgNO_3$ (aq.) solution and 157.4 ml, 314.8 ml, 472.2 ml, 629.6 ml, 787 ml and 1.57 l of $Cu(NO_3)_2 \cdot 3H_2O$ (aq.) solution with 1 g of ap-SBA-15 under stirring for 2h. Finally, the solid obtained was filtered, washed with deionized water and subjected to calcination at 350°C under an inert

atmosphere for 3h. The corresponding catalysts were named as M/ap-SBA-15 (M = Au, Ag or CuO).

1.3.5 Synthesis of binary mixture (Au-Ag) loaded SBA-15 nanocomposites

The bimetallic/binary mixture Au-Ag/*m*-SBA-15 nanocomposites were prepared by sequential impregnation method. Briefly to 0.5 g of *m*-SBA-15, 25.35 ml, 51 ml, 76 ml, 102 ml, 127 ml and 254 ml of 1 mM of $HAuCl_4$ solution was added under stirring followed by addition of fixed amount (23.15 ml) of solution of $AgNO_3$ (w.r.t 1 wt. % Ag loading), stirred for 3h at room temperature, filtered, washed with ammonia solution and deionized water and dried for overnight at 60 ^oC. The solid was calcined under H_2 at a rate of 1^oC/min till 350 ^oC and maintained for 3h, leading to the formation of light brown to dark purple colored samples designated as Au-Ag (x-y)/*m*-SBA-15 (x is the amount of Au loading varying from 1, 5 and 10 wt. % and y is the 1 wt. % loading of Ag).

1.3.6 Characterization techniques

1.3.6.1 Powder X-ray diffraction

It is an analytical technique applied for investigating surface structural studies of the prepared materials using X-rays, neutron or electron diffraction on powdered samples. It helps in providing information about the crystallanity, phase identification, determination of the lattice parameters as well as the size and strain broadening. The crystallite size of the samples is calculated using Scherrer equation, $D = k\lambda/\beta\cos\theta$ where k is a constant, λ is the X-ray wavelength, D is the average crystallite size, θ is the diffraction angle and β is full width at half maxima of the diffraction line. **PANalytical Expert Pro X-Ray diffractometer** was employed for obtaining Powder X-ray diffraction (XRD) patterns utilizing Cu-Kα radiation (λ=1. 54 Å) within the 2θ range of 0.5-5^o and 10-80^o.

Strain in the synthesized samples was calculated using **Williamson- Hall plot equation** (Grover et al., 2014) involving measurement of slope of line plotted between 4 sinθ along the x axis and β Cos θ along the y axis where β is full width at half maxima, θ (in radians) by taking half of 2θ (from XRD) diffraction line.

$$\beta hkl\, cos\theta \;=\; K\lambda/D \;+\; 4\varepsilon\, sin\theta$$

From the linear fit to the data, the crystalline size was estimated from the y-intercept, and the strain ε, from the slope of the fit.

1.3.6.2 Transmission electron microscopy (TEM)

TEM is a microscopic technique that provides an insight into the minute structural details viz., shape, size and distribution of the NPs present on the support. Low magnification transmission electron micrographs were obtained on **Hitachi (H-7500) 120 kW**. HR-TEM micrographs were obtained for visualing lattice fringes. HR-TEM and elemental mapping analysis were recorded on **FEI Tecnai F20 microscope** operated at 200 kV.

1.3.6.3 Energy Dispersive X-ray (EDX) Spectrophotometer Analysis

It helps in both the qualitative and quantitative determination of the chemical composition of the localized points or surface of the sample. Moreover, the presence of contaminants in the sample can also be identified. EDX analysis was carried out using **FEI Tecnai F20 microscope** operated at 200 kV and **JEOL JSM-6510LB**.

1.3.6.4 X-ray photoelectron spectroscopy (XPS)

XPS is most extensively used a surface analytical technique that measures the elemental composition of the sample, empirical formula, chemical state and electronic state of the elements present in the sample. XPS spectrum is generally plotted between the number of electrons detected versus the kinetic energies of the electrons detected. Each spectrum consists of peaks which are characteristic of an element and corresponds to the electronic configuration of electrons present in an atom. **KRATOS-AXIS DLD spectrometer (Kratos Analytical, U.K.)** equipped with monochromatic Al Kά radiation at 1486.6 eV operated at 10 kW was used for carrying out XPS studies.

1.3.6.5 Thermo Gravimetric Analysis (TGA)

TGA is a technique of thermal analysis that helps to measure the thermal stability of the materials as a function of time or increasing temperature under inert atmospheric conditions through characteristic decomposition patterns. **TGA-50 Shimadzu Thermogravimetric analyzer** was used for thermal analyses within the temperature range of 100-800 ^{o}C at a heating rate of 1 ^{o}C/min under nitrogen and ambient atmospheric pressure.

1.3.6.6 Fourier-Transform Infrared (FTIR) Spectroscopy

FT-IR spectroscopy imparts qualitative and quantitative information about organic and inorganic samples. The working principle is based on the fact that bonds and groups of bonds vibrate at characteristic frequencies. When a sample is exposed to infrared radiations, absorbed infrared energy excites molecules into higher vibrational states, which is characteristic of a particular molecule. IR studies were performed on **Cary 660 series Agilent FTIR spectrometer** within the range of 400-4000 cm^{-1}using KBr pellet method.

1.3.6.7 UV-Vis diffuse reflectance spectrophotometer

This technique is used for determining the surface plasmon band of the prepared materials, a tentative measure of the size of the incorporated metal NPs present within the sample. Solid state UV-visible absorption spectra of the synthesized powdered materials were recorded on **AVANTES diffuse reflectance spectrophotometer** at room temperature within the range of 400-800 nm using $BaSO_4$ as a reference. For analysis, 5-10 mg of the prepared powdered sample was placed on a glass-slide and the light source probe was placed over the sample for obtaining the absorbance as well as the reflectance spectra.

1.3.6.8 Microwave plasma-Atomic emission spectroscopy (MP-AES)

It is an elemental technique that is used for the quantitative estimation of the elements present in the sample. **AGILENT Microwave Plasma Atomic Emission Spectrometer (MP-AES)** was used for performing MP-AES analysis in order to determine the amount of metal loading in the synthesized samples. Prior to the determination, the samples were treated with aqua regia for 30 min. and heated till evaporation. Finally, the samples were diluted with 5 % HNO_3 and filtrated to 20 ml volumetric flask.

1.3.6.9 Surface area analysis

Surface area (S_{BET}) studies were performed by pretreating 20 mg of all samples at the 200 ^oC under vacuum for 2h using a **BET surface area analyzer (BEL Sorp-max)**. Surface area analysis was done within the p/p_o range of 0.000026652-0.9901 for the adsorption branch and 0.9799-0.1 for the desorption branch whereas total pore volume was estimated within the p/p_o range of 0.99-0.385.

1.3.6.10 Gas chromatography-mass spectroscopy (GC-MS)

GC-MS was employed to determine the reaction intermediates or any side products formed during the course of the reaction in the reaction mixture. For this purpose, the reaction mixture was withdrawn at regular intervals of time, filtered using cellulose filter (0.22 μm) and the clear solution was used for analysis. Gas chromatography-mass spectroscopy (GC-MS) studies were carried out on **Shimadzu, GC-2010 and GC-MS-QP 2010 plus with RTX-5Sil-MS column** (30 mm × 0.25 mm × 0.25 μm) using Helium as a carrier gas with a flow of 1ml/min through capillary column. The injector was maintained at 240 °C. Oven was programmed at 60 °C to 300 °C at 6 °C/min rise of temperature.

1.3.6.11 High pressure liquid chromatography (HPLC)

An analytical technique used for the differentiation and quantification of various components in a reaction mixture. HPLC analysis was performed on HPLC **(AGILENT, 1120 compact LC using using QUASIL BDS C-18 column)** at wavelengths λ = 220 nm and 254 nm with a mobile phase consisting of MeOH: H_2O (70:30) ratio at a flow rate of 1ml/min for the detection of nitrobenzene, *m*- and *p*- dinitrobenzene, *m*-chloronitrobenzene, *m*-nitrotoluene, *p*-nitrophenol, *p*-nitroacetophenone respectively. For analysis, 20 μl of the reaction mixture was injected into the loop, after filtration by cellulose filter of 0.22 μm.

1.3.7 Catalytic reaction

Catalytic activity of various prepared M/ap-SBA-15 catalysts (Scheme 1.2) was evaluated for the reduction of various nitroaromatics (Table 1.5) by mixing catalyst, substrate in ethanol and ice cold sodium borohydride aqueous solution with constant stirring at room temperature (for supported Au and Ag nanocomposites) and at 70 ^oC (for supported CuO and Au:Ag nanocomposites). For Au and Ag-loaded SBA-15 nanocomposites, the catalytic activity was evaluated by mixing together catalyst (5 mg for Au and 10 mg for Ag), substrate (5ml, 5 mM for Au/ap-SBA-15 and 5 ml, 3 mM for Ag/ap-SBA-15 composites) and ice-cold $NaBH_4$ (1ml, 0.5 m Au/ap-SBA-15 and 1 ml,0.3M for Ag/ap-SBA-15 composites) under stirring at room temperature. However, for CuO/m-SBA-15 composites, 10 mg catalyst was stirred with 5 ml, 3 mM substrate solution in ethanol and 1 ml, 0.3M $NaBH_4$ solution at 70 ^oC for investigating their catalytic efficiency. The progress of the reaction was monitored by HPLC (Agilent, 1120 compact LC using C-18 column) at wavelength λ = 220 nm and 254 nm with a flow rate of

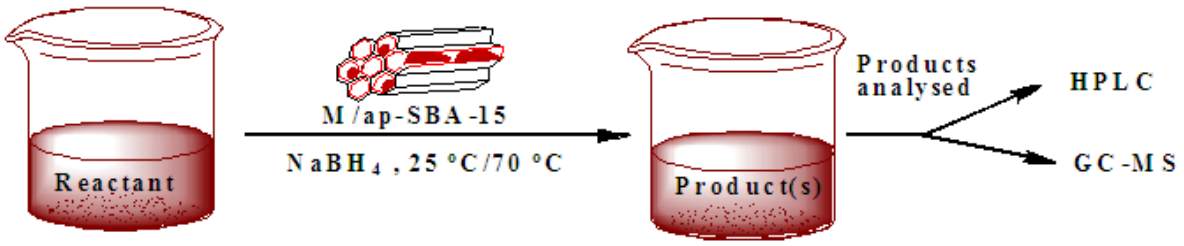

Scheme 1.2 Experimental set up for catalytic reduction with various metal supported catalysts

1ml/min using MeOH: H_2O (70:30) as the mobile phase. The intermediates were confirmed by GC-MS analysis. The reusability and stability studies of the synthesized catalysts were investigated by recovering the catalyst by filtration, washing with ethanol and deionized water followed by drying in air at 60 ^oC for 8h.

Table 1.5 Nitroaromatics studied for reduction with various metal supported SBA-15 catalysts

S.No.	Substrate studied	Products analyzed
1.	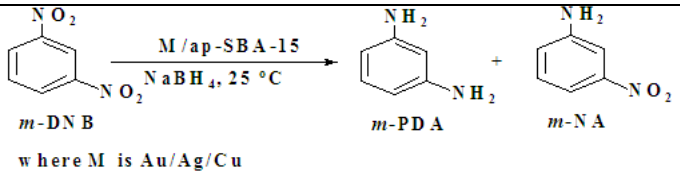 where M is Au/Ag/Cu	
2.	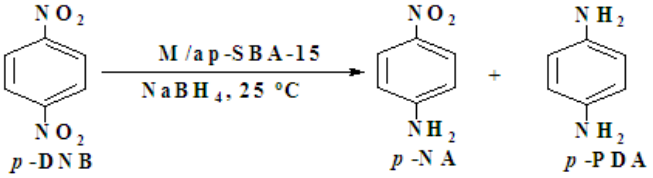 where M is Au/Ag	
3.	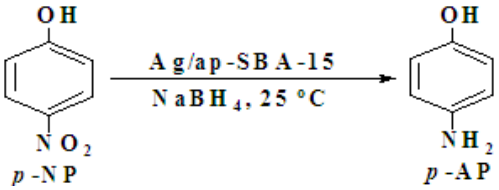	
4.	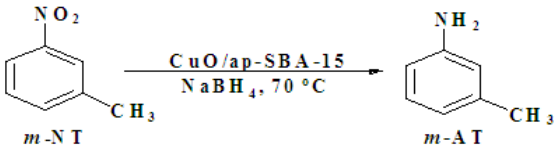	

5.

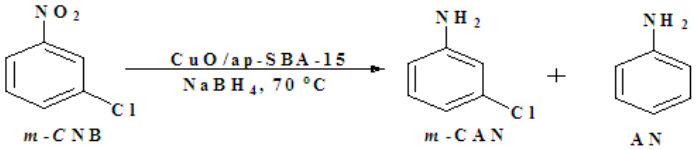
NO2
Cl
m-CNB
CuO/ap-SBA-15
NaBH4, 70 °C
NH2
Cl
m-CAN
+
NH2
AN

6.

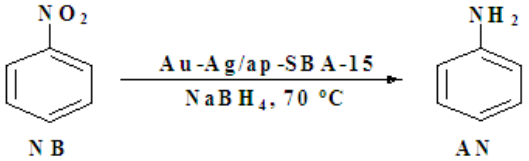
NO2
NB
Au-Ag/ap-SBA-15
NaBH4, 70 °C
NH2
AN

7.

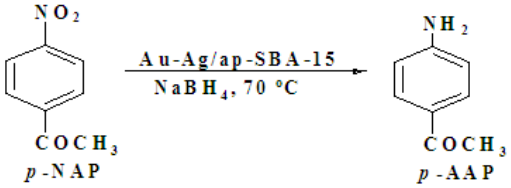
NO2
COCH3
p-NAP
Au-Ag/ap-SBA-15
NaBH4, 70 °C
NH2
COCH3
p-AAP

1.4 References

Alothman, Z.A. and Apblett, A.W., 2010. Synthesis and characterization of a hexagonal mesoporous silica with enhanced thermal and hydrothermal stabilities. Applied Surface Science, 256(11), pp.3573-3580.

Attard, G.S., Leclerc, S.A., Maniguet, S., Russell, A.E., Nandhakumar, I. and Bartlett, P.N., 2001. Mesoporous Pt/Ru alloy from the hexagonal lyotropic liquid crystalline phase of a nonionic surfactant. Chemistry of materials, 13(5), pp.1444-1446.

Bagshaw, S.A., Prouzet, E. and Pinnavaia, T.J., 1995. Templating of mesoporous molecular sieves by nonionic polyethylene oxide surfactants.Science, 269(5228), pp.1242-1244.

Barrer, R.M., 1982. Hydrothermal chemistry of zeolites. Academic Press.

Beck, J.S., Vartuli, J.C., Roth, W.J., Leonowicz, M.E., Kresge, C.T., Schmitt, K.D., Chu, C.T.W., Olson, D.H. and Sheppard, E.W., 1992. A new family of mesoporous molecular sieves prepared with liquid crystal templates. Journal of the American Chemical Society, 114(27), pp.10834-10843.

Binder, A.J., Qiao, Z.A., Veith, G.M. and Dai, S., 2013. Deposition-Precipitation and Stabilization of a Silica-Supported Au Catalyst by Surface Modification with Carbon Nitride. Catalysis letters, 143(12), pp.1339-1345.

Breck, D.W., 1974. Zeolite molecular sieves: structure. Chemistry and Use, Wiley, New York, 636.

Campelo, J.M., Luna, D., Luque, R., Marinas, J.M. and Romero, A.A., 2009. Sustainable preparation of supported metal NPs and their applications in catalysis. ChemSusChem, 2(1), pp.18-45.

Cardenas-Lizana, F., Gomez-Quero, S., Hugon, A., Delannoy, L., Louis, C. and Keane, M.A., 2009. Pd-promoted selective gas phase hydrogenation of p-chloronitrobenzene over alumina supported Au. Journal of Catalysis, 262(2), pp.235-243.

Carrero, A., Calles, J.A. and Vizcaino, A.J., 2007. Hydrogen production by ethanol steam reforming over Cu-Ni/SBA-15 supported catalysts prepared by direct synthesis and impregnation. Applied Catalysis A: General, 327, pp. 82-94.

Chen, C.S., Lai, Y.T., Lai, T.W., Wu, J.H., Chen, C.H., Lee, J.F. and Kao, H.M., 2013. Formation of Cu NPs in SBA-15 Functionalized with Carboxylic Acid Groups and Their Application in the Water–Gas Shift Reaction. ACS Catalysis, 3(4), pp.667-677.

Chen, D., Qu, Z., Shen, S., Li, X., Shi, Y., Wang, Y., Fu, Q. and Wu, J., 2011. Comparative studies of silver based catalysts supported on different supports for the oxidation of formaldehyde. Catalysis Today, 175(1), pp.338-345.

Chen, L.F., Guo, P.J., Zhu, L.J., Qiao, M.H., Shen, W., Xu, H.L. and Fan, K.N., 2009. Preparation of Cu/SBA-15 catalysts by different methods for the hydrogenolysis of dimethyl maleate to 1, 4-butanediol. Applied Catalysis A: General, 356(2), pp.129-136.

Chen, S.Y., Huang, C.Y., Yokoi, T., Tang, C.Y., Huang, S.J., Lee, J.J., Chan, J.C., Tatsumi, T. and Cheng, S., 2012. Synthesis and catalytic activity of amino-functionalized SBA-15 materials with controllable channel lengths and amino loadings. Journal of Materials Chemistry, 22(5), pp.2233-2243.

Chi, Y.S., Lin, H.P. and Mou, C.Y., 2005. CO oxidation over gold nanocatalyst confined in mesoporous silica. Applied Catalysis A: General, 284(1), pp.199-206.

Czaplinska, J., Sobczak, I. and Ziolek, M., 2014. Bimetallic Ag-Cu/SBA-15 System: The Effect of Metal Loading and Treatment of Catalyst on Surface Properties. The Journal of Physical Chemistry C, 118(24), pp.12796-12810.

Davis, M.E., 2002. Ordered porous materials for emerging applications. Nature, 417(6891), pp.813-821.

Della Pina, C., Falletta, E. and Rossi, M., 2008. Highly selective oxidation of benzyl alcohol to benzaldehyde catalyzed by bimetallic gold–copper catalyst. Journal of Catalysis, 260(2), pp.384-386.

Deng, Y., Cai, Y., Sun, Z., Liu, J., Liu, C., Wei, J., Li, W., Liu, C., Wang, Y. and Zhao, D., 2010. Multifunctional mesoporous composite microspheres with well-designed nanostructure: a highly integrated catalyst system. Journal of the American Chemical Society, 132(24), pp.8466-8473.

Dirin, D.N., Dreyfuss, S., Bodnarchuk, M.I., Nedelcu, G., Papagiorgis, P., Itskos, G. and Kovalenko, M.V., 2014. Lead halide perovskites and other metal halide complexes as

inorganic capping ligands for colloidal nanocrystals. Journal of the American Chemical Society, 136(18), pp.6550-6553.

El-Kolli, N., Delannoy, L. and Louis, C., 2013. Bimetallic Au–Pd catalysts for selective hydrogenation of butadiene: Influence of the preparation method on catalytic properties. Journal of Catalysis, 297, pp.79-92.

El-Sheikh, S.M., Ismail, A.A. and Al-Sharab, J.F., 2013. Catalytic reduction of p-nitrophenol over precious metals/highly ordered mesoporous silica. New Journal of Chemistry, 37(8), pp.2399-2407.

Elyassi, B., Al Wahedi, Y., Rajabbeigi, N., Kumar, P., Jeong, J.S., Zhang, X., Kumar, P., Balasubramanian, V.V., Katsiotis, M.S., Mkhoyan, K.A. and Boukos, N., 2014. A high-performance adsorbent for hydrogen sulfide removal. Microporous and Mesoporous Materials, 190, pp.152-155.

Fattori, N., Maroneze, C.M., da Costa, L.P., Strauss, M., Sigoli, F.A., Mazali, I.O. and Gushikem, Y., 2012. Ion-Exchange properties of Imidazolium-Grafted SBA-15 toward $AuCl_4^-$Anions and their conversion into supported gold NPs. Langmuir, 28(27), pp.10281-10288.

Ferrando, R., Jellinek, J. and Johnston, R.L., 2008. Nanoalloys: from theory to applications of alloy clusters and NPs. Chemical reviews, 108(3), pp.845-910.

Fuku, K., Hayashi, R., Takakura, S., Kamegawa, T., Mori, K. and Yamashita, H., 2013. The Synthesis of Size-and Color-Controlled Silver NPs by Using Microwave Heating and their Enhanced Catalytic Activity by Localized Surface Plasmon Resonance. Angewandte Chemie International Edition, 52(29), pp.7446-7450.

Gavia, D.J. and Shon, Y.S., 2015. Catalytic Properties of Unsupported Palladium Nanoparticle Surfaces Capped with Small Organic Ligands. ChemCatChem, 7(6), pp.892-900.

Ghosh, B.K., Hazra, S., Naik, B. and Ghosh, N.N., 2015. Preparation of Cu nanoparticle loaded SBA-15 and their excellent catalytic activity in reduction of variety of dyes. Powder Technology, 269, pp.371-378.

Grover, I.S., Singh, S. and Pal, B., 2015. Influence of Thermal Treatment and Fe-Loading on Morphology, Crystal Structure, and Photocatalytic Activity of Sodium Titanate Nanotubes. Particulate Science and Technology, 33(2), pp.132-138.

Gu, J., Fan, W., Shimojima, A. and Okubo, T., 2008. Microwave-induced synthesis of highly dispersed gold NPs within the pore channels of mesoporous silica. Journal of Solid State Chemistry, 181(4), pp.957-963.

Gu, J., Huang, Y., Elangovan, S.P., Li, Y., Zhao, W., Toshio, I., Yamazaki, Y. and Shi, J., 2011. Highly dispersed copper species within SBA-15 introduced by the hydrophobic core of a surfactant micelle as a carrier and their enhanced catalytic activity for cyclohexane oxidation. The Journal of Physical Chemistry C, 115(43), pp.21211-21217.

Gutierrez, L.F., Hamoudi, S. and Belkacemi, K., 2011. Synthesis of gold catalysts supported on mesoporous silica materials: Recent developments.Catalysts, 1(1), pp.97-154.

Han, J., Fang, P., Jiang, W., Li, L. and Guo, R., 2012. Ag-nanoparticle-loaded mesoporous silica: spontaneous formation of Ag NPs and mesoporous silica SBA-15 by a one-pot strategy and their catalytic applications. Langmuir, 28(10), pp.4768-4775.

Harisekhar, M., Pavan Kumar, V., Shanthi Priya, S. and Chary, K.V., 2015. Vapour phase hydrogenolysis of glycerol to propanediols over Cu/SBA-15 catalysts. Journal of Chemical Technology and Biotechnology, 90(10), pp.1906-1917.

Haruta, M., Kobayashi, T., Sano, H. and Yamada, N., 1987. Novel gold catalysts for the oxidation of carbon monoxide at a temperature far below 0 ^{o}C. Chemistry Letters, (2), pp.405-408.

Hong, Y.C., Sun, K.Q., Zhang, G.R., Zhong, R.Y. and Xu, B.Q., 2011. Fully dispersed Pt entities on nano-Au dramatically enhance the activity of gold for chemoselective hydrogenation catalysis. Chemical Communications, 47(4), pp.1300-1302.

Huang, X., Dong, W., Wang, G., Yang, M., Tan, L., Feng, Y. and Zhang, X., 2011. Synthesis of confined Ag nanowires within mesoporous silica via double solvent technique and their catalytic properties. Journal of Colloid and Interface Science, 359, pp.40-46.

Huo, Q., Margolese, D.I., Ciesia, U., Feng, P., Gier, T.E., Sieger, P., Leon, R., Petroff, P.M., Schuth, F., Stucky, G.D., 1994a. Generalized synthesis of periodic surfactant/inorganic composite materials. Nature, 368, pp. 317-321.

Huo, Q., Margolese, D.I., Ciesla, U., Demuth, D.G., Feng, P., Gier, T.E., Sieger, P., Firouzi, A. and Chmelka, B.F., 1994b. Organization of organic molecules with inorganic molecular species into nanocomposite biphase arrays. Chemistry of Materials, 6(8), pp.1176-1191.

Hutchings, G.J. and Haruta, M., 2005. A golden age of catalysis: A perspective. Applied Catalysis A: General, 291(1), pp.2-5.

Hutchings, G.J., 1985. Vapor phase hydrochlorination of acetylene: correlation of catalytic activity of supported metal chloride catalysts. Journal of Catalysis, 96(1), pp.292-295.

Jia, L., Zhang, S., Gu, F., Ping, Y., Guo, X., Zhong, Z. and Su, F., 2012. Highly selective gas-phase oxidation of benzyl alcohol to benzaldehyde over silver-containing hexagonal mesoporous silica. Microporous and Mesoporous Materials, 149(1), pp.158-165.

Khodakov, A.Y., Zholobenko, V.L., Bechara, R. and Durand, D., 2005. Impact of aqueous impregnation on the long-range ordering and mesoporous structure of cobalt containing MCM-41 and SBA-15 materials. Microporous and Mesoporous Materials, 79(1), pp.29-39.

Kong, A., Wang, H., Yang, X., Hou, Y. and Shan, Y., 2009. A facile direct route to synthesize large-pore mesoporous silica incorporating high CuO loading with special catalytic property. Microporous and Mesoporous Materials, 118(1), pp.348-353.

Kresge, C.T., Leonowicz, M.E., Roth, W.J., Vartuli, J.C. and Beck, J.S., 1992. Ordered mesoporous molecular sieves synthesized by a liquid-crystal template mechanism. Nature, 359(6397), pp.710-712.

Li, X., Fang, S.S.S., Teo, J., Foo, Y.L., Borgna, A., Lin, M. and Zhong, Z., 2012. Activation and Deactivation of Au-Cu/SBA-15 Catalyst for Preferential Oxidation of CO in H_2-Rich Gas. ACS Catalysis, 2(3), pp.360-369.

Lin, H.P., Chi, Y.S., Lin, J.N., Mou, C.Y. and Wan, B.Z., 2001. Direct Synthesis of MCM-41 Mesoporous Aluminosilicates Containing Au NPs in Aqueous Solution. Chemistry Letters, (11), pp.1116-1117.

Linssen, T., Cassiers, K., Cool, P. and Vansant, E.F., 2003. Mesoporous templated silicates: an overview of their synthesis, catalytic activation and evaluation of the stability. Advances in colloid and interface science, 103(2), pp.121-147.

Liu, X., Wang, A., Yang, X., Zhang, T., Mou, C.Y., Su, D.S. and Li, J., 2008. Synthesis of thermally stable and highly active bimetallic Au-Ag NPs on inert supports. Chemistry of Materials, 21(2), pp.410-418.

Liu, X., Wang, A., Zhang, T., Su, D.S. and Mou, C.Y., 2011. Au-Cu alloy NPs supported on silica gel as catalyst for CO oxidation: Effects of Au/Cu ratios. Catalysis today, 160(1), pp.103-108.

Liu, Y., Tsunoyama, H., Akita, T. and Tsukuda, T., 2009. Preparation of ∼1 nm Gold Clusters Confined within Mesoporous Silica and Microwave-Assisted Catalytic Application for Alcohol Oxidation. The Journal of Physical Chemistry C, 113(31), pp.13457-13461.

Ma, C.Y., Dou, B.J., Li, J.J., Cheng, J., Hu, Q., Hao, Z.P. and Qiao, S.Z., 2009. Catalytic oxidation of benzyl alcohol on Au or Au-Pd NPs confined in mesoporous silica. Applied Catalysis B: Environmental, 92(1), pp.202-208.

Ma, G., Binder, A., Chi, M., Liu, C., Jin, R., Jiang, D.E., Fan, J. and Dai, S., 2012. Stabilizing gold clusters by heterostructured transition-metal oxide-mesoporous silica supports for enhanced catalytic activities for CO oxidation. Chemical Communications, 48(93), pp.11413-11415.

Ma, L., Guo, X. and Xiang, L., 2014. Catalytic activity of Ag/SBA-15 for low-temperature gas-phase selective oxidation of benzyl alcohol to benzaldehyde. Chinese Journal of Catalysis, 35(1), pp.108-119.

Margolese, D., Melero, J.A., Christiansen, S.C., Chmelka, B.F. and Stucky, G.D., 2000. Direct Syntheses of Ordered SBA-15 Mesoporous Silica Containing Sulfonic Acid Groups. Chem. Mater. 12, (8), 2448–2459.

Mondal, J., Borah, P., Modak, A., Zhao, Y. and Bhaumik, A., 2013. Cu-Grafted Functionalized Mesoporous SBA-15: A Novel Heterogeneous Catalyst for Facile One-Pot Three-Component C–S Cross-Coupling Reaction of Aryl Halides in Water. Organic Process Research & Development, 18(1), pp.257-265.

Nagy, G., Benko, T., Borko, L., Csay, T., Horvath, A., Frey, K. and Beck, A., Bimetallic Au-Ag/SiO_2 catalysts: comparison in glucose, benzyl alcohol and CO oxidation reactions. Reaction Kinetics, Mechanisms and Catalysis, 115(1), pp.45-65.

Naik, B., Hazra, S., Prasad, V.S. and Ghosh, N.N., 2011. Synthesis of Ag NPs within the pores of SBA-15: an efficient catalyst for reduction of 4-nitrophenol. Catalysis Communications, 12(12), pp.1104-1108.

Okumura, M., Tsubota, S. and Haruta, M., 2003. Preparation of supported gold catalysts by gas-phase grafting of gold acethylacetonate for low-temperature oxidation of CO and of H_2. Journal of Molecular Catalysis A: Chemical, 199(1), pp.73-84.

Ovoshchnikov, D.S., Donoeva, B.G., Williamson, B.E. and Golovko, V.B., 2014. Tuning the selectivity of a supported gold catalyst in solvent-and radical initiator-free aerobic oxidation of cyclohexene. Catalysis Science & Technology, 4(3), pp.752-757.

Parida, K.M. and Dash, S.S., 2009. Manganese containing MCM-41: Synthesis, characterization and catalytic activity in the oxidation of ethylbenzene. Journal of Molecular Catalysis A: Chemical, 306(1), pp.54-61.

Park, S.J., Lee, D.H. and Kang, Y.S., 2010. High temperature proton exchange membranes based on triazoles attached onto SBA-15 type mesoporous silica. Journal of Membrane Science, 357(1), pp.1-5.

Patel, A., Rufford, T.E., Rudolph, V. and Zhu, Z., 2011. Selective catalytic reduction of NO by CO over CuO supported on SBA-15: Effect of CuO loading on the activity of catalysts. Catalysis today, 166(1), pp.188-193.

Petre, A.L., Carbajo, J.B., Rosal, R., Garcia-Calvo, E. and Perdigón-Melón, J.A., 2013. CuO/SBA-15 catalyst for the catalytic ozonation of mesoxalic and oxalic acids. Water matrix effects. Chemical Engineering Journal, 225, pp.164-173.

Prouzet, E. and Pinnavaia, T.J., 1997. Assembly of mesoporous molecular sieves containing wormhole motifs by a nonionic surfactant pathway: control of pore size by synthesis temperature. Angewandte Chemie International Edition in English, 36(5), pp.516-518.

Qu, Z., Ke, G., Wang, Y., Liu, M., Jiang, T. and Gao, J., 2013. Investigation of factors influencing the catalytic performance of CO oxidation over Au-Ag/SBA-15 catalyst. Applied Surface Science, 277, pp.293-301.

Ren, L.H., Zhang, H.L., Lu, A.H., Hao, Y. and Li, W.C., 2012. Porous silica as supports for controlled fabrication of $Au/CeO_2/SiO_2$ catalysts for CO oxidation: Influence of the silica nanostructures. Microporous and Mesoporous Materials, 158, pp.7-12.

Ressler, T., Walter, A., Huang, Z.D. and Bensch, W., 2008. Structure and properties of a supported MoO_3-SBA-15 catalyst for selective oxidation of propene. Journal of catalysis, 254(2), pp.170-179.

Schimpf, S., Lucas, M., Mohr, C., Rodemerck, U., Brückner, A., Radnik, J., Hofmeister, H. and Claus, P., 2002. Supported gold NPs: in-depth catalyst characterization and application in hydrogenation and oxidation reactions. Catalysis Today, 72(1), pp.63-78.

Schunemann, S., Dodekatos, G. and Tuysuz, H., 2015. Mesoporous Silica Supported Au and AuCu NPs for Surface Plasmon Driven Glycerol Oxidation. Chemistry of Materials. 27(22), pp. 7743-7750.

Sekhar, A.S., Sivaranjani, K., Gopinath, C.S. and Vinod, C.P., 2012. A simple one pot synthesis of nano gold–mesoporous silica and its oxidation catalysis. Catalysis Today, 198(1), pp.92-97.

Selvakannan, P.R., Mantri, K., Tardio, J. and Bhargava, S.K., 2013. High surface area Au-SBA-15 and Au–MCM-41 materials synthesis: Tryptophan amino acid mediated confinement of gold nanostructures within the mesoporous silica pore walls. Journal of colloid and interface science, 394, pp.475-484.

Shu, X.Z., Nguyen, S.C., He, Y., Oba, F., Zhang, Q., Canlas, C., Somorjai, G.A., Alivisatos, A.P. and Toste, F.D., 2015. Silica-Supported Cationic Gold (I) Complexes as Heterogeneous Catalysts for Regio-and Enantioselective Lactonization Reactions. Journal of the American Chemical Society. 137(22), pp.7083-7086.

SikáYun, Y. and SungáPark, D., 2014. A facile approach for the preparation of tunable acid nano-catalysts with a hierarchically mesoporous structure.Chemical Communications, 50(57), pp.7652-7655.

Sing, K.S., 1985. Reporting physisorption data for gas/solid systems with special reference to the determination of surface area and porosity (Recommendations 1984). Pure and applied chemistry, 57(4), pp.603-619.

Slowing, I.I., Trewyn, B.G., Giri, S. and Lin, V.Y., 2007. Mesoporous silica NPs for drug delivery and biosensing applications. Advanced Functional Materials, 17(8), pp.1225-1236.

Soule, J.F., Miyamura, H. and Kobayashi, S., 2011. Powerful amide synthesis from alcohols and amines under aerobic conditions catalyzed by gold or gold/iron,-nickel or-cobalt NPs. Journal of the American Chemical Society, 133(46), pp.18550-18553.

Subbaramaiah, V., Srivastava, V.C. and Mall, I.D., 2013. Optimization of reaction parameters and kinetic modeling of catalytic wet peroxidation of picoline by Cu/SBA-15. Industrial & Engineering Chemistry Research, 52(26), pp.9021-9029.

Szegedi, Á., Popova, M., Valyon, J., Guarnaccio, A., De Stefanis, A., De Bonis, A., Orlando, S., Sansone, M., Teghil, R. and Santagata, A., 2014. Comparison of silver NPs confined in nanoporous silica prepared by chemical synthesis and by ultra-short pulsed laser ablation in liquid. Applied Physics A, 117(1), pp.55-62.

Szostak, R., Molecular Sieves-Principles of Synthesis and Identification, 1st ed.; Van Nostrand Reinhold: New York, 1989; 2nd ed.; Blackie: London, 1998.

Takai, A., Doi, Y., Yamauchi, Y. and Kuroda, K., 2010. Soft-chemical approach of noble metal nanowires templated from mesoporous Silica (SBA-15) through vapor infiltration of a reducing agent. *The Journal of Physical Chemistry C*, *114*(17), pp.7586-7593.

Ungureanu, A., Dragoi, B., Chirieac, A., Royer, S., Duprez, D. and Dumitriu, E., 2011. Synthesis of highly thermostable copper-nickel NPs confined in the channels of ordered mesoporous SBA-15 silica. Journal of Materials Chemistry, 21(33), pp.12529-12541.

Vargas-Hernandez, D., Rubio-Caballero, J.M., Santamaria-Gonzalez, J., Moreno-Tost, R., Merida-Robles, J.M., Perez-Cruz, M.A., Jimenez-Lopez, A., Hernandez-Huesca, R. and Maireles-Torres, P., 2014. Furfuryl alcohol from furfural hydrogenation over copper supported on SBA-15 silica catalysts. Journal of Molecular Catalysis A: Chemical, 383, pp.106-113.

Walcarius, A., Mandler, D., Cox, J.A., Collinson, M. and Lev, O., 2005. Exciting new directions in the intersection of functionalized sol–gel materials with electrochemistry. Journal of Materials Chemistry, 15(35-36), pp.3663-3689.

Wang, A., Liu, X.Y., Mou, C.Y. and Zhang, T., 2013. Understanding the synergistic effects of gold bimetallic catalysts. Journal of Catalysis, 308, pp.258-271.

Wang, H.K., Yi, C.Y., Tian, L., Wang, W.J., Fang, J., Zhao, J.H. and Shen, W.G., 2012a. Ag-Cu bimetallic NPs prepared by Microemulsion method as catalyst for epoxidation of styrene. Journal of Nanomaterials, 2012, p.4

Wang, S., Guo, W., Wang, H., Zhu, L., Yin, S. and Qiu, K., 2014. Effect of the Cu/SBA-15 catalyst preparation method on methyl acetate hydrogenation for ethanol production. New Journal of Chemistry, 38(7), pp.2792-2800.

Wang, T., Yuan, X., Li, S., Zeng, L. and Gong, J., 2015. CeO_2 modified Au@SBA-15 nanocatalysts for liquid-phase selective oxidation of benzyl alcohol. Nanoscale, 7(17), pp.7593-7602.

Wang, Y.N., Duan, X., Zheng, J., Lin, H., Yuan, Y., Ariga, H., Takakusagi, S. and Asakura, K., 2012b. Remarkable enhancement of Cu catalyst activity in hydrogenation of dimethyl oxalate to ethylene glycol using gold. Catalysis Science & Technology, 2(8), pp.1637-1639.

Wei, X., Yang, X.F., Wang, A.Q., Li, L., Liu, X.Y., Zhang, T., Mou, C.Y. and Li, J., 2012. Bimetallic Au-Pd Alloy Catalysts for N_2O Decomposition: Effects of Surface Structures on Catalytic Activity. The Journal of Physical Chemistry C, 116(10), pp.6222-6232.

Wu, P., Bai, P., Loh, K.P. and Zhao, X.S., 2010. Au NPs dispersed on functionalized mesoporous silica for selective oxidation of cyclohexane. Catalysis Today, 158(3), pp.220-227.

Xu, C., De, S., Balu, A.M., Ojeda, M. and Luque, R., 2015. Mechanochemical synthesis of advanced nanomaterials for catalytic applications. Chemical Communications, 51(31), pp.6698-6713.

Yen, C.W., Lin, M.L., Wang, A., Chen, S.A., Chen, J.M. and Mou, C.Y., 2009. CO oxidation catalyzed by Au-Ag bimetallic NPs supported in mesoporous silica. The Journal of Physical Chemistry C, 113(41), pp.17831-17839.

Yin, A., Wen, C., Dai, W.L. and Fan, K., 2011. Ag/MCM-41 as a highly efficient mesostructured catalyst for the chemoselective synthesis of methyl glycolate and ethylene glycol. Applied Catalysis B: Environmental, 108, pp.90-99.

Yin, H., Ma, Z., Zhu, H., Chi, M. and Dai, S., 2010. Evidence for and mitigation of the encapsulation of gold NPs within silica supports upon high-temperature treatment of Au/SiO_2 catalysts: Implication to catalyst deactivation. Applied Catalysis A: General, 386(1), pp.147-156.

Zhang, H., Tang, C., Lv, Y., Sun, C., Gao, F., Dong, L. and Chen, Y., 2012. Synthesis, characterization, and catalytic performance of copper-containing SBA-15 in the phenol hydroxylation. Journal of colloid and interface science, 380(1), pp.16-24.

Zhang, R., Shi, D., Liu, N., Cao, Y. and Chen, B., 2014b. Mesoporous SBA-15 promoted by 3d-transition and noble metals for catalytic combustion of acetonitrile. Applied Catalysis B: Environmental, 146, pp.79-93.

Zhang, W., Wang, Q., Wu, H., Wu, P. and He, M., 2014a. A highly ordered mesoporous polymer supported imidazolium-based ionic liquid: an efficient catalyst for cycloaddition of CO_2 with epoxides to produce cyclic carbonates. Green Chemistry, 16(11), pp.4767-4774.

Zhang, X., Huang, N., Wang, G., Dong, W., Yang, M., Luan, Y. and Shi, Z., 2013. Synthesis of highly loaded and well dispersed CuO/SBA-15 via an ultrasonic post-grafting method and its application as a catalyst for the direct hydroxylation of benzene to phenol. Microporous and Mesoporous Materials, 177, pp.47-53.

Zhang, X., Qu, Z., Li, X., Zhao, Q., Wang, Y. and Quan, X., 2011. Low temperature CO oxidation over Ag/SBA-15 nanocomposites prepared via in-situ "pH-adjusting" method. Catalysis Communications, 16(1), pp.11-14.

Zhao, D., Feng, J., Huo, Q., Melosh, N., Fredrickson, G.H., Chmelka, B.F. and Stucky, G.D., 1998. Triblock copolymer syntheses of mesoporous silica with periodic 50 to 300 angstrom pores. Science, 279(5350), pp.548-552.

Zhao, X.S., Lu, G.Q. and Millar, G.J., 1996. Advances in mesoporous molecular sieve MCM-41. Industrial & Engineering Chemistry Research, 35(7), pp.2075-2090.

Zheng, J., Lin, H., Wang, Y.N., Zheng, X., Duan, X. and Yuan, Y., 2013. Efficient low-temperature selective hydrogenation of esters on bimetallic Au-Ag/SBA-15 catalyst. Journal of Catalysis, 297, pp.110-118.

Zheng, N. and Stucky, G.D., 2006. A general synthetic strategy for oxide-supported metal nanoparticle catalysts. Journal of the American Chemical Society, 128(44), pp.14278-14280.

Zhong, X., Barbier, J., Duprez, D., Zhang, H. and Royer, S., 2012. Modulating the copper oxide morphology and accessibility by using micro-mesoporous SBA-15 structures as host support: effect on the activity for the CWPO of phenol reaction. Applied Catalysis B: Environmental, 121, pp.123-134.

Zhu, Y., Morisato, K., Li, W., Kanamori, K. and Nakanishi, K., 2013. Synthesis of silver NPs confined in hierarchically porous monolithic silica: a new function in aromatic hydrocarbon separations. ACS applied materials & interfaces, 5(6), pp.2118-2125.

Zienkiewicz-Strzalka, M., Pasieczna-Patkowska, S., Kozak, M. and Pikus, S., 2013. Silver NPs incorporated onto ordered mesoporous silica from Tollen's reagent. Applied Surface Science, 266, pp.337-343.

Chapter 2

Homogeneous dispersion of Au nanoparticles into mesoporous SBA-15 exhibiting improved catalytic activity for nitroaromatic reduction

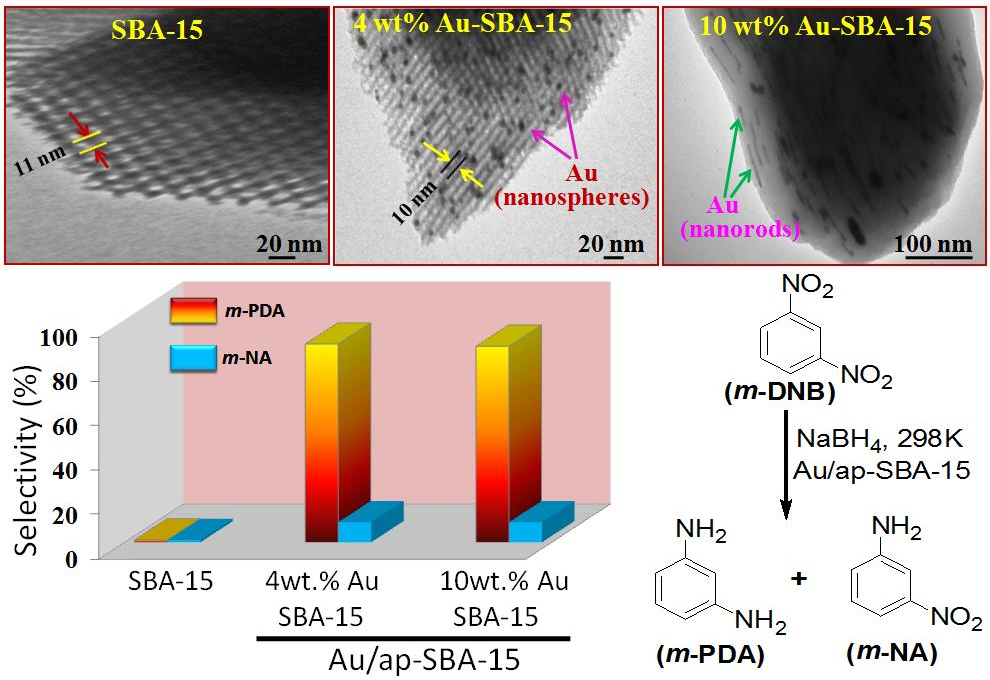

2.1 Introduction

In order to enhance the applications of SBA-15 in catalysis, modification of the siliceous mesoporous surface by loading metals, metal oxides, acid groups and organic functionalities such as $–NH_2$, -SH either by direct synthesis (one-pot method) or post-synthesis approach has been reported. The most widely employed method is impregnation with solutions of thermally unstable precursor salts (e.g. nitrates, chlorides and acetates) (Schuth et al. 2001; Sauer et al. 2002). There are reports regarding the incorporation of different metal species like Au, Ag, Pt, Pd into these mesoporous supports either through physical adsorption or chemical adsorption between noble metal ions and functionalized mesoporous channels (Naik et al. 2010 and 2011). A great amount of research has been dedicated to the synthesis of Au incorporated SBA-15 nanocomposites as Au exhibits exceptional optical, electrical and catalytic properties in comparison to bulk metals. SBA-15 modified with N-trimethoxysilylpropyl-N,N,N-trimethylammonium chloride (TPTAC) (Takai et al., 2010) and 3-aminopropyltriethoxysilane (APTES) (Xie et al., 2008) has been used as a template for the incorporation of gold nanowires (AuNW) and gold nanorods (AuNR). Moreover, this association of the highly active noble metal nanostructures within heterogeneous support conforms to the greener approach with increased selectivity, yield, conversion and catalyst recovery. Attempts have been made for the synthesis of non-aggregated stable metal nanostructures inside the mesoporous support. Several recent reports regarding the formation of Au supported SBA-15 nanocomposites have already been described in section 1.2.3 (chapter 1). It is observed that most of these synthetic procedures utilize organic solvents, toxic chelating agents, strong reducing agents like $NaBH_4$, hydrazine etc. Hence, spontaneous formation of homogeneously dispersed noble metal NPs of controlled morphology like NR and NW within mesoporous silica by a benign synthetic procedure is still a challenge. In this respect, the current report deals with a greener approach of wet-impregnation (without the use of any reducing agent) for the synthesis of well dispersed, quantum sized Au nanostructures of different morphologies i.e., Au nanospheres (AuNS) and Au nanorods (AuNR) stabilized within the channels of SBA-15 for catalyzing nitroaromatic reductions.

2.2 Experimental Section

2.2.1 Synthesis and characterization of Au/ap-SBA-15 catalysts

The synthesis and characterization of Au/ap-SBA-15 catalysts have already been described in section 1.3.2-1.3.4 and 1.3.6 (Chapter 1).

2.2.2 Catalytic activity

The catalytic activity of prepared Au/ap-SBA-15 nanocomposites was evaluated for the reduction of *m*- and *p*-DNB (5 mM) as per procedure given in section (section 1.3.7, chapter 1). Reaction samples were analyzed by GC-MS and HPLC (section 1.3.6.10 and 1.3.6.11, chapter 1).

2.3 Results and discussion

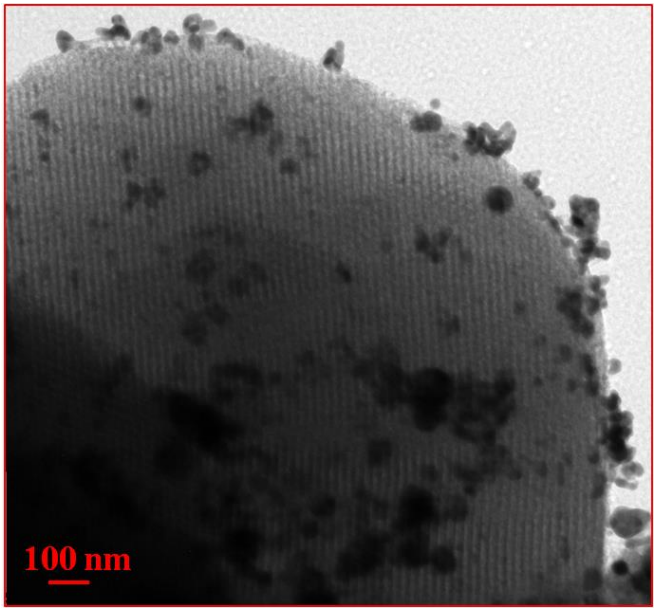

Fig. 2.1 TEM image of Au loaded SBA-15 nanocomposite without surface modification.

Initially, Au loaded SBA-15 nanocomposites were prepared by loading bare SBA-15 with an aqueous solution of Au precursor and it was found that large aggregates were formed on the surface of SBA-15 (Fig. 2.1). So, for the formation of small sized and uniformly dispersed Au nano species within the mesoporous support, the surface of SBA-15 was modified with APTES. Surface modification helped in the creation of anchoring sites for Au precursor. After surface modification, SBA-15 was impregnated with Au precursor followed by autoclaving for 24h. Finally, it was calcined at 550 ^{o}C leading to the formation of fine and well dispersed Au nanostructures. However, the prepared Au loaded SBA-15 nanocomposites exhibited moderate catalytic activity (with 50 % selectivity for *m*-PDA) for the reduction of *m*-DNB. Then, the autoclaving time was increased to 48h when a small increase in the catalytic activity (with 55 % selectivity for *m*-PDA) was observed. Further, highest catalytic activity (89 % selectivity for *m*-PDA) was obtained when the autoclaving period was increased to 72h. Moreover, all the prepared nanocomposites retained mesoporous structure based on optical studies, surface structural morphology, TEM and N_2 sorption isotherms and are being described.

2.3.1 Absorbance spectroscopic studies

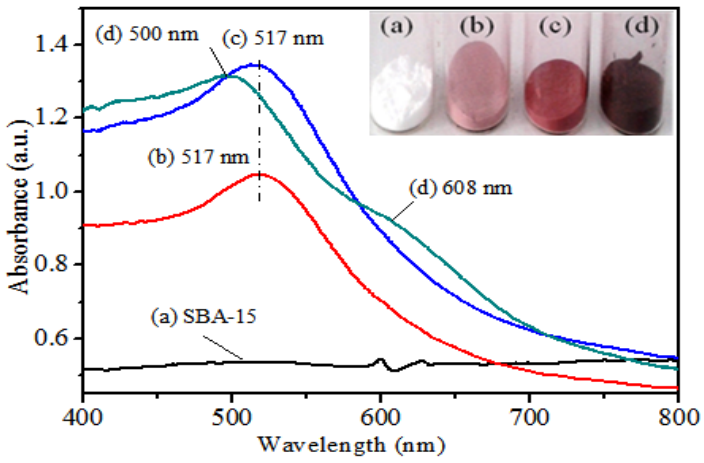

Fig. 2.2 Solid state absorption spectra of **(a)** bare SBA-15, **(b)** 1 wt.% Au/ap-SBA-15, **(c)** 4 wt.% Au/ap-SBA-15 and **(d)** 10 wt. % Au/ap-SBA-15.

Solid state UV-vis absorbance spectra of the X wt.% Au/ap-SBA-15 catalysts (Fig. 2.2) showed the appearance of surface plasmon resonance (SPR) band centered at 517 nm for both 1 wt.% and 4 wt.% Au/ap-SBA-15 samples confirming the presence of small sized AuNS (Link et al., 1999) while no band was observed for bare SBA-15. Generally, the absorption band at 528 nm corresponds to the formation of surface passivated quantum size (5-10 nm) AuNS (Gu et al., 2008) stabilized by surfactant coating that prevents their agglomeration. However, in the present case the absorption band is blue shifted to 517 nm indicating the formation of very small AuNS of size < 5 nm incorporated in the channels of mesoporous SBA-15 as evident in the TEM images (Fig. 2.5c-d) where nanoparticles (NPs) are fixed in solid support having fewer chances of agglomeration. On increasing Au loading (10 wt. %), the transverse band at 500 nm and a broad hump at ~608 nm indicated the presence of anisotropic NPs. Generally, the formation of anisotropic NPs like NR is exhibited by the appearance of two absorption bands in the spectra i.e. transverse band at ~526 nm and longitudinal band within the range of 650-850 nm respectively (Yang et al., 2008). But the spectra at higher Au loading revealed that perfect NR may not have been formed but AuNS within the mesoporous channels may have got aligned/packed one after another resulting in the formation of NR like shape as also reported by Gao et al. (2011) and Rioux et al. (2005). Moreover, a change in the color of as-prepared Au/ap-SBA-15 samples was observed from white (bare SBA-15) to dark purple (10 wt. % Au loading) further indicating incorporation of Au in mesoporous SBA-15.

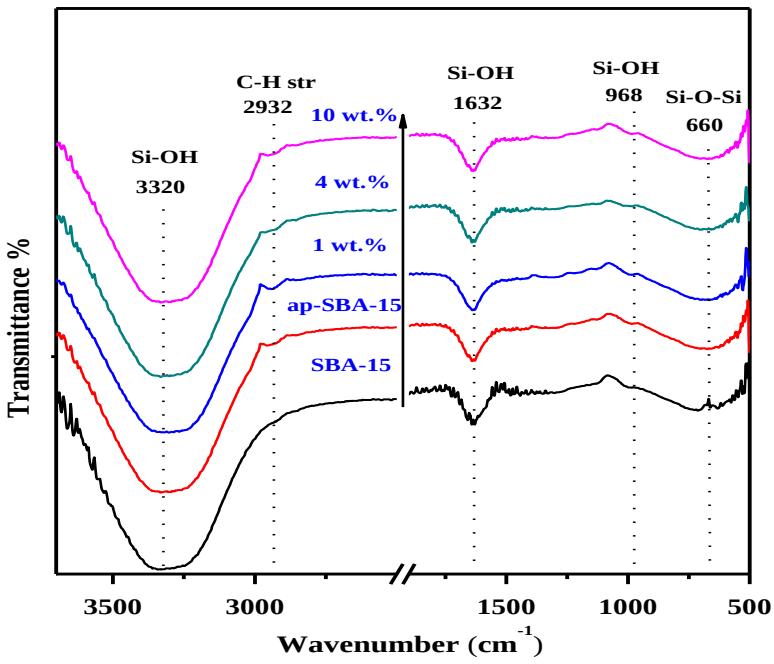

Fig. 2.3 FT-IR spectra of SBA-15, ap-SBA-15 and various wt. % Au/ap-SBA-15 catalysts.

The FTIR spectra of bare SBA-15, ap-SBA-15 and Au/ap-SBA 15 catalysts (Fig. 2.3) showed the appearance of two broad bands at 3320 cm^{-1} and 1632 cm^{-1} assignable to the stretching and another weak band at 968 cm^{-1} due to the bending vibrations of silanol groups (Han et al., 2012; Viswanathan et al., 2014). Another weak band at 660 cm^{-1} can be assigned to Si-O-Si linkage. An additional band at 2932 cm^{-1} attributed to the C-H stretching modes of $-CH_2$ in APTES (Lin et al., 2008) is seen in ap-SBA-15 and X wt. % Au/ap-SBA-15 samples, indicating that there is no deformation in the basic structure of ap-SBA-15 on Au loading.

2.3.2 Powder XRD studies

The low angle powder XRD patterns of prepared samples (Fig. 2.4a) show well resolved peaks at 0.9°, 1.5° and 1.8° having hkl values (100), (110) and (200) respectively (Wang et al., 2006) assignable to highly ordered 2D-hexagonal symmetry characteristic of MMs (Zhao et al., 1998) indicating retention of mesoporous structure even after surface modification with APTES and Au loading. With the increase in Au loading, a decrease in the structural parameters viz., d-spacing is observed from 10.9 nm to 9.51 nm (Table 2.1) in comparison to SBA-15. Decrease in d-spacing and unit cell parameters signify contraction due to the development of compressive strain that resulted due to the encapsulation of metal NPs inside the host pores.

Wide angle XRD patterns of the prepared samples (Fig. 2.4b) show a characteristic band at $2\theta = 22°$ between 15° and 35° (Zhang et al., 2000) corresponding to the amorphous silica walls

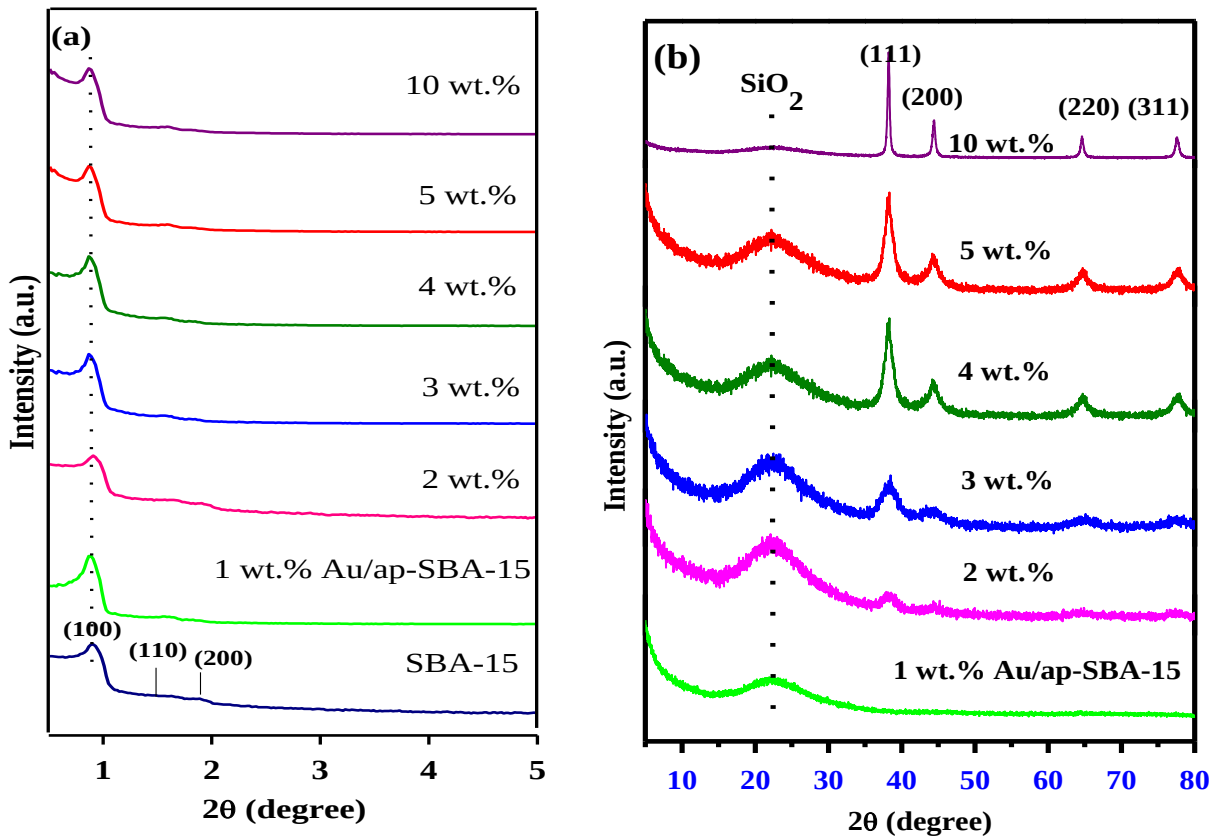

Fig. 2.4 (a) Low angle and **(b)** wide angle XRD patterns of bare SBA-15 and various wt. % Au/ap-SBA-15 catalysts.

of SBA-15. In addition to the broadband, four distinct diffractions at 38°, 44.3°, 64.3° and 77.3° were observed corresponding to (111), (200), (220) and (311) planes indicating nanocrystalline nature of gold (JCPDS: 4-784). These peaks become more intense and narrower with an increase in Au loading from 1 wt. % to 10 wt. % suggesting an increase in the size of the embedded AuNPs and that the increased amount of AuNS fuse together to form AuNR within the channels of SBA-15. Further, the crystallite size of Au/ap-SBA-15 nanocomposites calculated from (111) peak using Scherrer equation was found to be 5.5 nm for AuNS (4 wt. % Au loading) and vary between 90-180 nm for AuNR (10 wt. % Au loading). This has been further supported by findings of Xie et al. (2008) that as AgNPs grow to form NR at higher $AgNO_3$ concentration, the peaks corresponding to Ag become more intense and sharper. Moreover, solid state UV-visible absorbance studies (Fig. 2.2), also showed the presence of anisotropic AuNPs at higher (4 and 10 wt. %) Au loading.

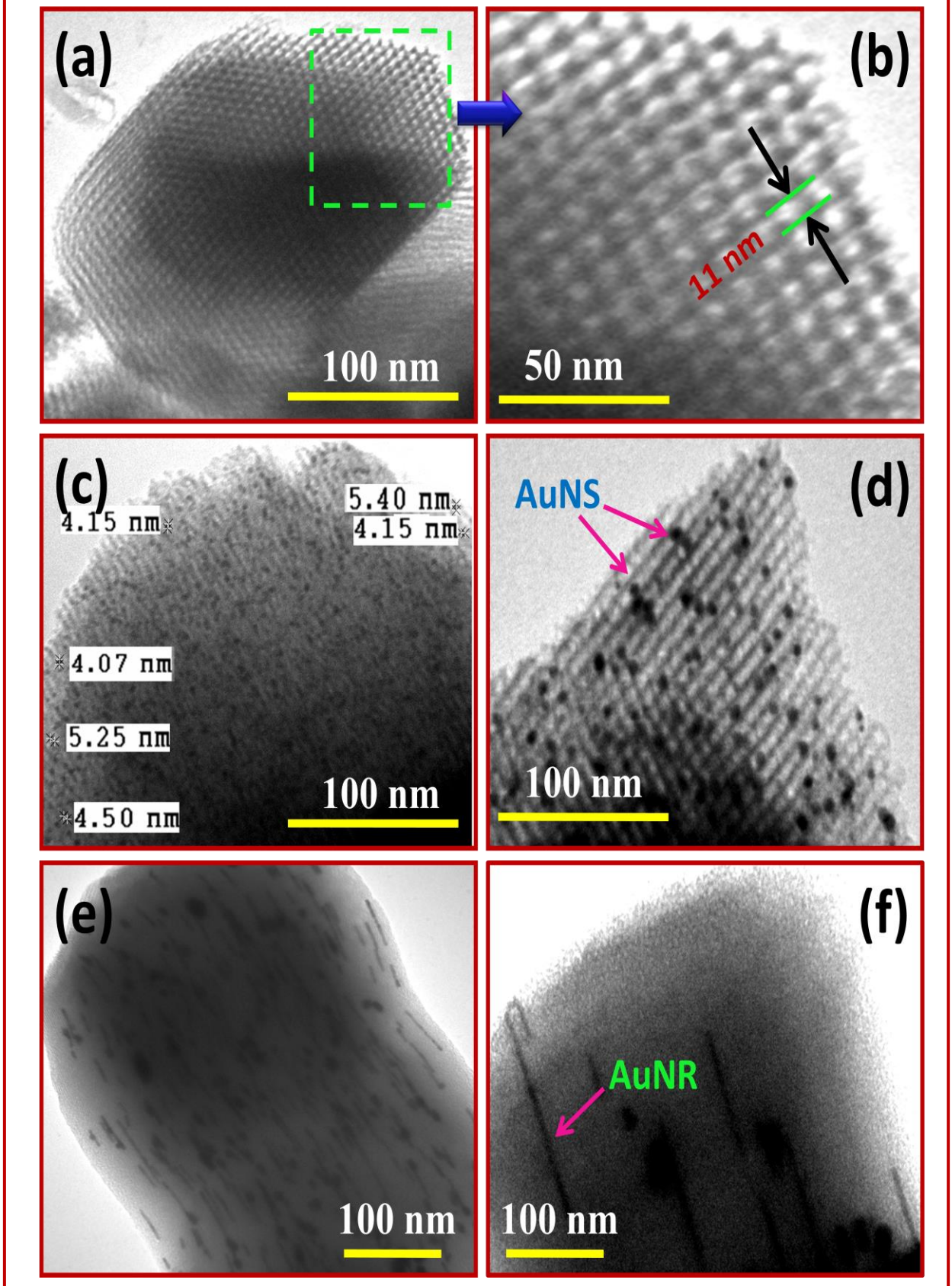

Fig. 2.5 TEM images of **(a)** SBA-15, **(b)** enlarged portion of (a), **(c)** 1 wt.% Au/ap-SBA-15, **(d)** 4 wt.% Au/ap-SBA-15 and **(e, f)** 10 wt.% Au/ap-SBA-15.

2.3.3 TEM

TEM micrographs (Fig. 2.5a, b) displayed a regular hexagonal pore structure of SBA-15 with pore diameter ~8 nm. Incorporation of 1 wt. % of Au onto the support resulted in the formation of smaller AuNS (~5 nm) homogeneously dispersed within the SBA-15 channels. The presence of AuNS in the matrix was depicted in the form of dark black dots against the light background of the SBA-15 matrix (Fig. 2.5c). With an increase in Au loading from 1 to 4 wt. %, an increase in the size of AuNS (~6 nm) was observed (marked in Fig. 2.5d). On further increasing Au loading (to 10 wt. %), neighboring AuNS fused to form fine AuNR (average aspect ratio ~17 nm) evenly scattered throughout the entire framework of SBA-15 (Fig. 2.5e). Thus, the pore-size of the mesoporous channels indirectly controlled and acted as a limiting factor in promoting the growth of embedded AuNPs. Moreover, these channels remained well intact even with 10 wt. % of Au loading. Rioux et al. (2005) also demonstrated the aggregation of neighboring particles to form nanorods in alignment with the mesoporous channels at higher Pt content of 14.4 wt. % followed by heat treatment. However, higher Au loading (~10 wt. %) led to inhomogeneous filling of the mesoporous channels as depicted in Fig. 2.5f. This may be due to the fact that the filling of the channels depend on the synthesis procedure i.e. orientation and distribution of nano species under stirring and thermal treatments. Moreno et al. (2006) also reported that anisotropic distribution of NPs within mesoporous silica depends on the behavior of their distribution under thermal treatment. However, in the present study, for the preparation of samples, the surface of the SBA-15 was modified with APTES and then the appropriate quantity of Au was impregnated on surface modified SBA-15 by continuous stirring for 2h followed by calcination at 350 ^{o}C for 3h. Since higher metal loading (10 wt. %) resulted in the formation of anisotropic NPs that may occupy different orientations and result in the inhomogeneous distribution of nano species within the channels. It was thus observed that dispersion density of Au NPs into mesopores of SBA-15 was always increased as a function of the amount of Au loading.

2.3.4 Textural properties

Nitrogen adsorption-desorption isotherms and pore size distributions of all materials are shown in Fig. 2.6. The hysteresis loop at relative pressures p/p_o between 0.6-0.8 (Fig. 2.6a) indicated their mesoporous character with narrow pore size distribution corresponding to type IV isotherms according to IUPAC classification (Rouquerol et al., 1999), characteristic of SBA-15 type materials (Thielemann et al., 2011). Identical shape of all the isotherms indicates that the

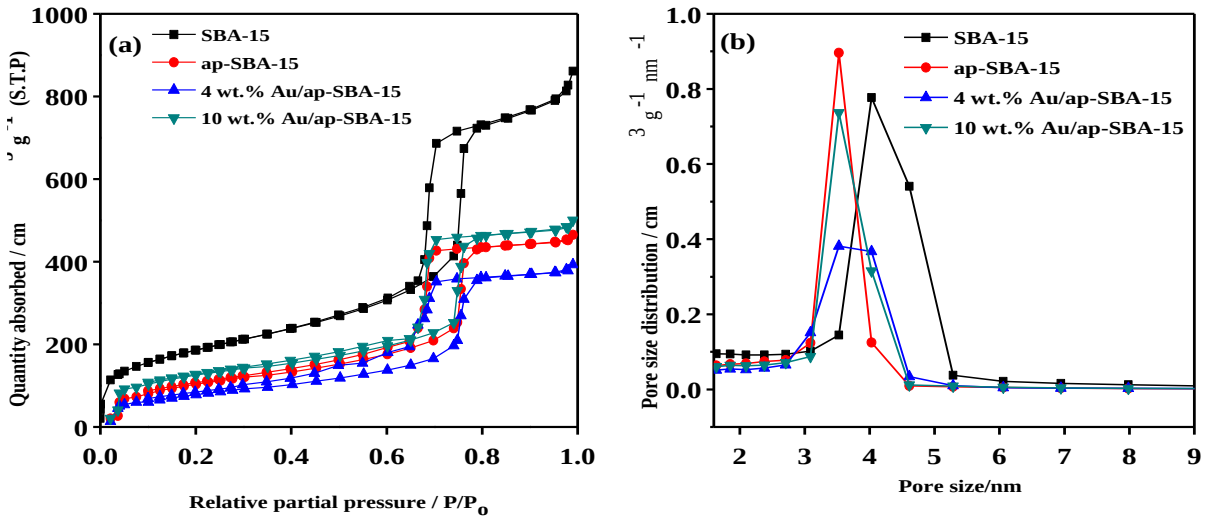

Fig. 2.6 (a) Nitrogen adsorption-desorption isotherms and **(b)** pore size distribution of SBA-15, ap-SBA-15 and various wt. % Au/ap-SBA-15 catalysts.

structure of mesoporous host was still maintained even after its modification with APTES and Au loading. Further, the surface area of bare SBA-15 i.e., 664 m^2/g was decreased to 373 m^2/g upon its modification with APTES. A similar trend was observed for pore volume and pore size (Table 2.1). The BET profile for ap-SBA-15 illustrated decrease in the amount of adsorbed nitrogen and shifting of the inflection point of the step to the lower p/p_o region (0.8 to 0.5) signifying the reduction in surface area (Fig. 2.6a) and decrease in pore size (Fig. 2.6b) respectively. This indicated that organic moieties may be present as a thick layer covering the silica surface. Similar findings have also been reported by Petkov et al. (2005) for Au supported SBA-15 nanocomposites having a surface of SBA-15 modified with 3-mercaptopropyltrimethoxysilane (MPS). Impregnation of Au (from 1 to 4 wt. %) onto the support further decreased the surface area, pore volume and pore size. These results were further supported by the decrease in the volume of adsorbed nitrogen indicating decreased surface area due to the existence of metal species inside the pores i.e. pore filling effect (Li et al., 2009) by the formation of NPs inside SBA-15. channels. Taghavimoghaddam et al. (2012) also reported similar results for various cobalt loadings (≥ 30 wt % Co). Zhu et al. (2005) also reported a significant decrease in surface area and pore volume for metal loaded APTES functionalized samples attributed to the partial blockage of mesochannels of SBA-15 due to the sporadic dispersion of metal NPs. Moreover, 4 wt. % Au loaded

Table 2.1 Physicochemical parameters for pure SBA-15 and X wt. % Au/ap-SBA-15 nanocomposites

Sample	d-spacing, d_{100} (nm)	unit cell parameter, a_o (nm)[a]	wall thickness, d_w (nm)[b]	Surface area (m^2/g)	Pore volume (cm^3/g)	Pore size (nm)	Strain
SBA-15	10.92	12.6	1.6	664	1.33	8.02	
ap-SBA-15	9.93	11.47	1.49	373	0.71	7.64	-1.51
1 wt.% Au/ap-SBA-15	9.89	11.42	1.52	356	0.70	7.61	-1.79
2 wt.% Au/ap-SBA-15	9.51	10.99	1.47	343	0.68	7.89	-1.77
3 wt.% Au/ap-SBA-15	9.93	11.47	1.53	312	0.65	8.12	-1.82
4 wt.% Au/ap-SBA-15	9.91	11.44	1.53	292	0.60	8.24	-1.76
5 wt.% Au/ap-SBA-15	9.89	11.42	1.53	371	0.62	7.12	-1.29
10 wt.% Au/ap-SBA-15	9.71	11.21	1.53	457	0.76	6.72	-1.25

[a] $a_0 = 2/3^{1/2} d_{100}$. [b] $d_w = a_0 - d_{100,}$

ap-SBA-15 displayed the expected H1 hysteresis curve but with a pronounced tailing at the closing of the hysteresis curve i.e. at p/p_o ~0.4 indicating plugging of pores of SBA-15 up to some extent, attributed to the pore blocking effect due to the incorporating Au nano species within the pores. The curve showed one step capillary condensation which indicated uniform mesopores while a two-step capillary evaporation was observed in the desorption branch due to plugging of channels of SBA-15 with Au nano species. Similar findings have also been reported by Wu et al. (2008) in the adsorption isotherms of copper and chromium incorporated mesoporous SBA-15 nanocomposites. As Au loading was increased to 10 wt. %, an increase in the surface area and pore volume (Table 2.1) were observed probably due to the formation and deposition of nano species even on the outer surface of the mesoporous material.

2.3.5 Catalytic activity

2.3.5.1 Reduction of m-DNB and p-DNB

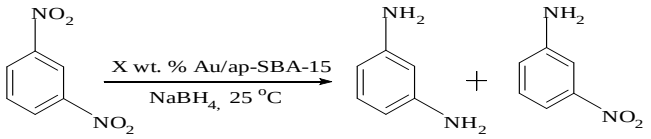

Scheme 2.1 Reduction of *m*-dinitrobenzene (*m*-DNB).

The reduction of *m*-DNB in ethanol with $NaBH_4$ and Au/ap-SBA-15 (1-10 wt. %) nanocomposites (Scheme 2.1, Fig. 2.7a) showed a linear relationship for change in concentration of *m*-DNB (-ln C/C_o v/s time) indicating pseudo first order kinetics. However, no change in concentration of *m*-DNB was observed with bare SBA-15. With the use of Au loaded materials, catalytic activity improved abruptly and maximum selectivity (~89%) obtained for *m*-PDA was with 4 wt. % Au loadings. A color change from light yellow to dark brown was observed due to the formation of *m*-PDA and the reaction was completed in less than 30 min. This gave unambiguous evidence that AuNPs were the real active sites. The reduction of *m*-DNB to *m*-PDA proceeded via the formation of *m*-NA as an intermediate confirmed by the GC-MS analysis (Fig. 2.8). A comparison of different catalysts (Fig. 2.7b) showed a gradual increase in selectivity with an increase in Au loading from 1-4 wt. % and then slight decrease with 5 and 10 wt. % of Au loading. The highest selectivity (~89 %) for *m*-PDA exhibited by 4 wt. % Au/ap-SBA-15 can be attributed to the high Au loading and uniform dispersion of optimum particle size (~5-6 nm) of AuNS within SBA-15 channels.

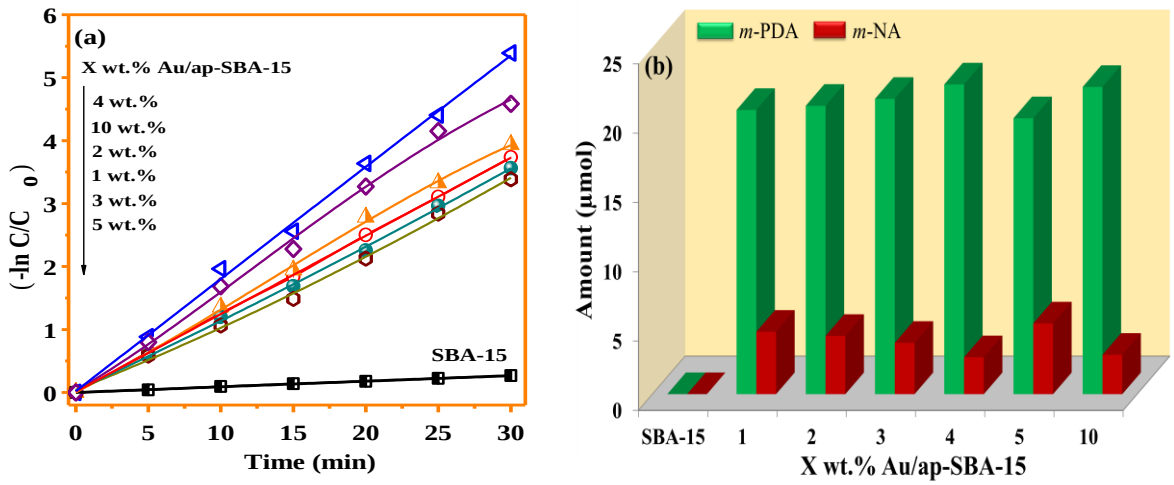

Fig. 2.7 (a) Change in the concentration of *m*-DNB (-ln C/C_o) as a function of time and **(b)** Reduction of *m*-dinitrobenzene (5 mM) to *m*-phenylenediamine (*m*-PDA) and *m*-nitroaniline (*m*-NA) by various wt.% Au/ap-SBA-15 catalysts.

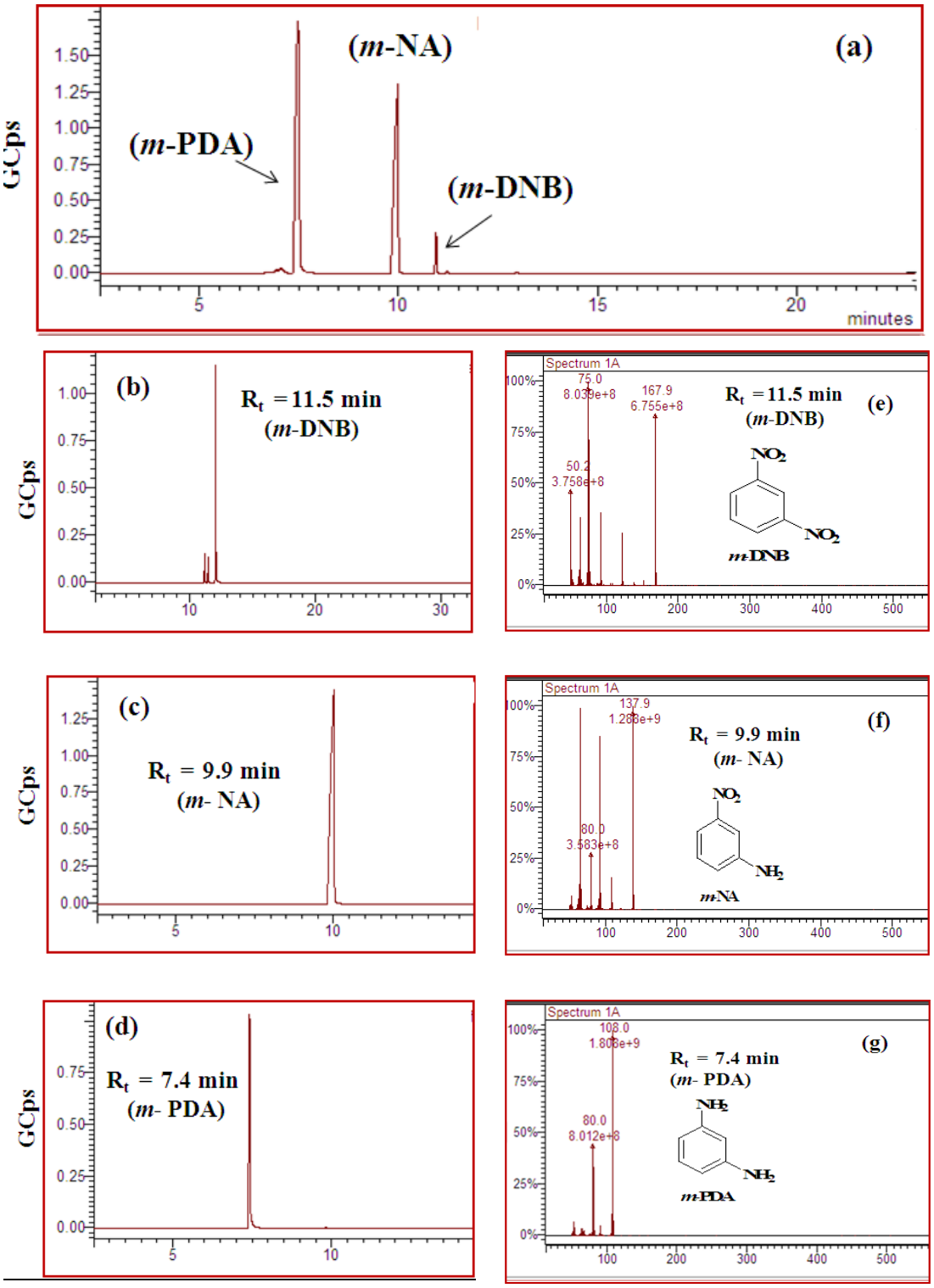

Fig. 2.8 GC of authentic 5 mM *m*-DNB **(b)**, *m*-NA **(c)** and *m*-PDA **(d) and** GC (a) and Mass spectra **(e-f and g)** of the reaction mixture at 15 min. interval.

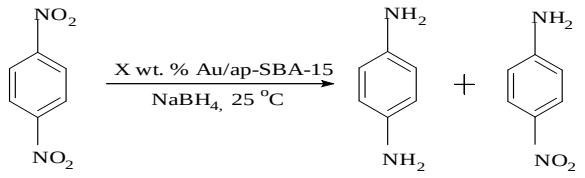

Scheme 2.2 Reduction of *p*-dinitrobenzene.

Small particle size and homogeneous metallic dispersion resulted in a large number of exposed active sites for favoring easy access of reactants that contributed towards efficient catalytic activity. Rojas et al. (2011) during liquid phase hydrogenation of *m*-DNB also found that particle size and metal dispersion greatly influenced the catalytic activity of supported platinum catalyst. In our study, however, a slight decrease in the catalytic activity for 5 and 10 wt. % of Au/ap-SBA-15 can be accounted for high metal loading, leading to pore blockage as well as a reduction in the number of available catalytic active sites for the reaction and is further confirmed by BET studies. For the synthesis of *m*-PDA from *m*-DNB over Ni/SiO_2, Liu et al. (2006) also reported a decrease in catalytic activity at high (20 wt. %) metal loading due to a reduction in the number of sufficient active sites.

Similarly, Au/ap-SBA-15 composites were also used for the reduction of *p*-DNB (Scheme 2.2). Again, linear plots were obtained for all Au loaded catalysts indicating pseudo first order kinetics of the reaction (Fig. 2.9a). The rate constants (Fig. 2.9c) varied from 8.96×10^{-3} for SBA-15 to 1.765×10^{-3} and 1.579×10^{-1} corresponding to 4 wt. % Au loading for the reduction of *m*- and *p*-DNB respectively. However, for the reduction of *p*-DNB, selectivity was reversed with highest selectivity (81%) obtained for *p*-NA using 4 wt. % Au/ap-SBA-15 (Fig. 2.9b). This was in contrast to the observed selectivity for *m*-DNB reduction. The product

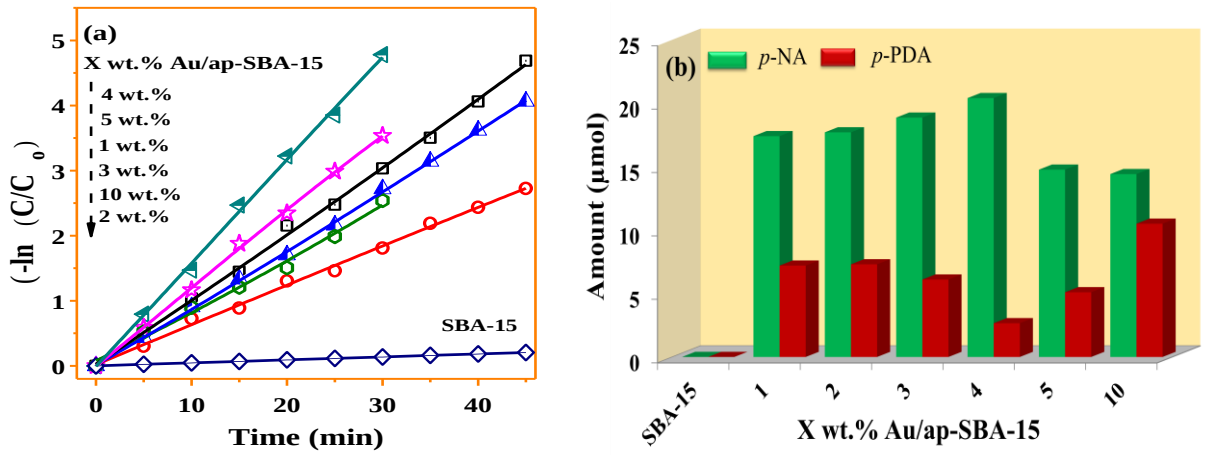

Fig. 2.9 (a) Change in the concentration of *p*-DNB (-ln C/C_o) as a function of time and **(b)** Reduction of *p*-dinitrobenzene (*p*-DNB) (5 mM) to *p*-phenylenediamine (*p*-PDA) and *p*-nitroaniline (*p*-NA) by various wt.% Au/ap-SBA-15 catalysts.

selectivity of dinitrobenzene reduction depends on the *m*- or *p*- substitution of groups that

strongly influences the formation of reduction products. In *m*-DNB, two electron withdrawing

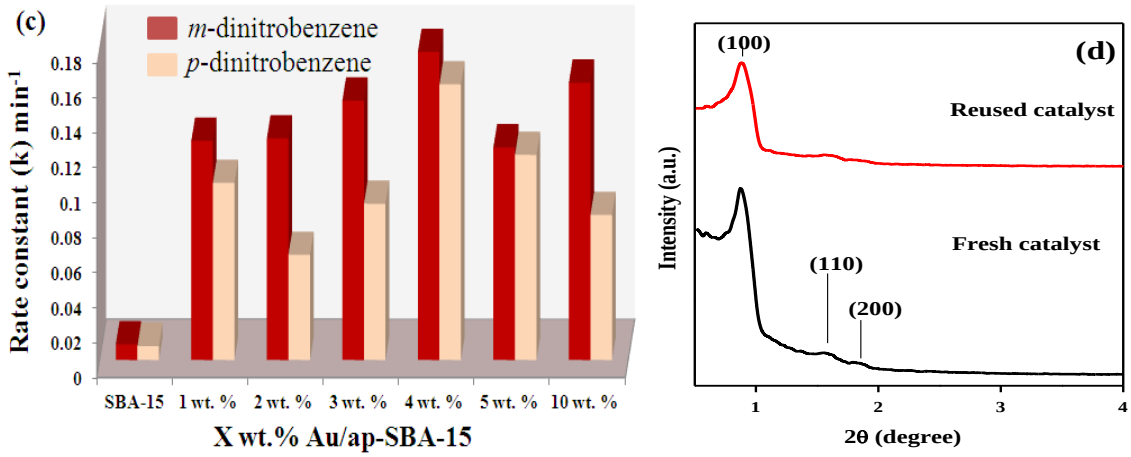

Fig. 2.9 (c) Rates of reaction for the reduction of *m*- and *p*-DNB using various wt. % Au/ap-SBA-15 catalysts and **(d)** Low angle XRD of reused catalyst (4 wt. % Au/ap-SBA-15) after fifth catalytic cycle.

groups ($–NO_2$) at *m*-position lowers the electron density and favor rapid conversion of both $–NO_2$ to $–NH_2$ groups resulting in higher selectivity of *m*-PDA. On the other hand, the presence of two $–NO_2$ groups at *p*-position (in *p*-DNB) results in lesser electronic induction thereby hampering reduction of the nitro group providing greater product selectivity as *p*-NA. Kaur et al. (2014) demonstrated similar results for photoreduction of dinitrobenzene by rutile TiO_2 and P25 TiO_2. The reusability of 4 wt. % Au/ap-SBA-15 catalyst was studied for the reduction of *m*-DNB. There was no significant loss of catalytic activity even after five recycles. Low angle XRD of the reused catalyst (Fig. 2.9d) displayed a small decrease in the intensity of the peak at 0.9^o corresponding to the (100) plane suggesting no significant change in the morphology and size of the metal nano species in the mesopores thus establishing high stability and reusability of prepared catalysts.

It is thus illustrated that the monodispersed AuNS and AuNR have been successfully synthesized within the channels of SBA-15 using facile post modified approach. The quantum sized, non-aggregated Au nanostructures stabilized within the mesochannels of SBA-15 exhibited improved catalytic activity over catalytically inactive bare SBA-15. The small size, better dispersion density and greater number of available active sites for 4 wt. % Au loading resulted in its higher catalytic activity for reduction of m- and p-dinitrobenzene. Moreover, excellent stability and reusability of the catalyst even after five recycle offers a great scope for extending it

to other noble metals promising greater opportunities for designing novel materials for various applications.

2.4 References

Gao, C., Zhang, Q., Lu, Z. and Yin, Y., 2011. Templated synthesis of metal nanorods in silica nanotubes. Journal of the American Chemical Society, 133(49), pp.19706-19709.

Gu, J., Fan, W., Shimojima, A. and Okubo, T., 2008. Microwave-induced synthesis of highly dispersed gold nanoparticles within the pore channels of mesoporous silica. Journal of Solid State Chemistry, 181(4), pp.957-963.

Han, J., Fang, P., Jiang, W., Li, L. and Guo, R., 2012. Ag-nanoparticle-loaded mesoporous silica: spontaneous formation of Ag nanoparticles and mesoporous silica SBA-15 by a one-pot strategy and their catalytic applications. Langmuir, 28(10), pp.4768-4775.

Kaur, J. and Pal, B., 2014. 100% selective yield of m-nitroaniline by rutile TiO_2 and *m*-phenylenediamine by P25-TiO_2 during m-dinitrobenzene photoreduction. Catalysis Communications, 53, pp.25-28.

Li, L., Jin, C., Wang, X., Ji, W., Pan, Y., Van der Knaap, T., Van der Stoel, R. and Au, C.T., 2009. Cyclohexane oxidation over size-uniform Au nanoparticles (SBA-15 hosted) in a continuously stirred tank reactor under mild conditions. Catalysis letters, 129(3-4), pp.303-311.

Lin, D.H., Jiang, Y.X., Wang, Y. and Sun, S.G., 2008. Silver nanoparticles confined in SBA-15 mesoporous silica and the application as a sensor for detecting hydrogen peroxide. Journal of Nanomaterials, 2008, p.12.

Link, S. and El-Sayed, M.A., 1999. Size and temperature dependence of the plasmon absorption of colloidal gold nanoparticles. The Journal of Physical Chemistry B, 103(21), pp.4212-4217.

Liu, Y., Wei, Z. and Zhang, J., 2006. Synthesis of m-phenylenediamine from m-dinitrobenzene over silica-supported nickel catalyst. Korean Journal of Chemical Engineering, 23(6), pp.902-907.

Moreno, M.S., Weyland, M., Midgley, P.A., Bengoa, J.F., Cagnoli, M.V., Gallegos, N.G., Alvarez, A.M. and Marchetti, S.G., 2006. Highly anisotropic distribution of iron nanoparticles within MCM-41 mesoporous silica. Micron, 37(1), pp.52-56.

Naik, B., Hazra, S., Prasad, V.S. and Ghosh, N.N., 2011. Synthesis of Ag nanoparticles within the pores of SBA-15: an efficient catalyst for reduction of 4-nitrophenol. Catalysis Communications, 12(12), pp.1104-1108.

Naik, B., Prasad, V.S. and Ghosh, N.N., 2010. A simple aqueous solution based chemical methodology for synthesis of Ag nanoparticles dispersed on mesoporous silicate matrix. Powder Technology, 199(2), pp.197-201.

Petkov, N., Stock, N. and Bein, T., 2005. Gold electroless reduction in nanosized channels of thiol-modified SBA-15 material. The Journal of Physical Chemistry B, 109(21), pp.10737-10743.

Rioux, R.M., Song, H., Hoefelmeyer, J.D., Yang, P. and Somorjai, G.A., 2005. High-surface-area catalyst design: synthesis, characterization, and reaction studies of platinum nanoparticles in mesoporous SBA-15 silica. The Journal of Physical Chemistry B, 109(6), pp.2192-2202.

Rojas, H., Borda, G., Reyes, P., Brijaldo, M. and Valencia, J., 2011. Liquid-phase hydrogenation of m-dinitrobenzene over platinum catalysts. Journal of the Chilean Chemical Society, 56(3), pp.793-798.

Rouquerol, F., Rouquerol, J. and Sing, K., 1999. Adsorption by Powders and Porous Solids Academic. New York, p.15.

Sauer, J., Marlow, F., Spliethoff, B. and Schuth, F., 2002. Rare earth oxide coating of the walls of SBA-15. Chemistry of materials, 14(1), pp.217-224.

Schuth, F., Wingen, A. and Sauer, J., 2001. Oxide loaded ordered mesoporous oxides for catalytic applications. Microporous and Mesoporous Materials, 44, pp.465-476.

Taghavimoghaddam, J., Knowles, G.P. and Chaffee, A.L., 2012. Preparation and characterization of mesoporous silica supported cobalt oxide as a catalyst for the oxidation of cyclohexanol. Journal of Molecular Catalysis A: Chemical, 358, pp.79-88.

Takai, A., Doi, Y., Yamauchi, Y. and Kuroda, K., 2010. Soft-chemical approach of noble metal nanowires templated from mesoporous silica (SBA-15) through vapor infiltration of a reducing agent. The Journal of Physical Chemistry C, 114(17), pp.7586-7593.

Thielemann, J.P., Girgsdies, F., Schlogl, R. and Hess, C., 2011. Pore structure and surface area of silica SBA-15: influence of washing and scale-up. Beilstein journal of nanotechnology, 2(1), pp.110-118.

Viswanathan, S., Narayanan, B., Yaakob, Z., Periyat, P. and Padikkaparambil, S., 2014. Selective formation of aniline over nanogold incorporated cobalt loaded SBA 15 catalysts. Journal of Porous Materials, 21(3), pp.251-262.

Wang, L., Qi, T., Zhang, Y. and Chu, J., 2006. Morphosynthesis route to large-pore SBA-15 microspheres. Microporous and mesoporous materials, 91(1), pp.156-160.

Wu, Z.Y., Wang, H.J., Zhuang, T.T., Sun, L.B., Wang, Y.M. and Zhu, J.H., 2008. Multiple Functionalization of Mesoporous Silica in One-Pot: Direct Synthesis of Aluminum-Containing Plugged SBA-15 from Aqueous Nitrate Solutions. Advanced Functional Materials, 18(1), pp.82-94.

Xie, Y., Quinlivan, S. and Asefa, T., 2008. Tuning metal nanostructures in mesoporous silica by a simple change of metal complexes and by reduction with grafted imines and hemiaminals. The Journal of Physical Chemistry C, 112(27), pp.9996-10003.

Yang, Z., Ni, W., Kou, X., Zhang, S., Sun, Z., Sun, L.D., Wang, J. and Yan, C.H., 2008. Incorporation of gold nanorods and their enhancement of fluorescence in mesostructured silica thin films. The Journal of Physical Chemistry C, 112(48), pp.18895-18903.

Zhang, W.H., Shi, J.L., Wang, L.Z. and Yan, D.S., 2000. Preparation and characterization of ZnO clusters inside mesoporous silica. Chemistry of materials, 12(5), pp.1408-1413.

Zhao, D., Feng, J., Huo, Q., Melosh, N., Fredrickson, G.H., Chmelka, B.F. and Stucky, G.D., 1998. Triblock copolymer syntheses of mesoporous silica with periodic 50 to 300 angstrom pores. Science, 279(5350), pp.548-552.

Zhu, K., Hu, J. and Richards, R., 2005. Aerobic oxidation of cyclohexane by gold nanoparticles immobilized upon mesoporous silica. Catalysis letters, 100(3), pp.195-199.

Chapter 3

Preparation, surface structural morphology and catalytic properties of uniformly dispersed Ag nanoparticle loaded mesoporous SBA-15

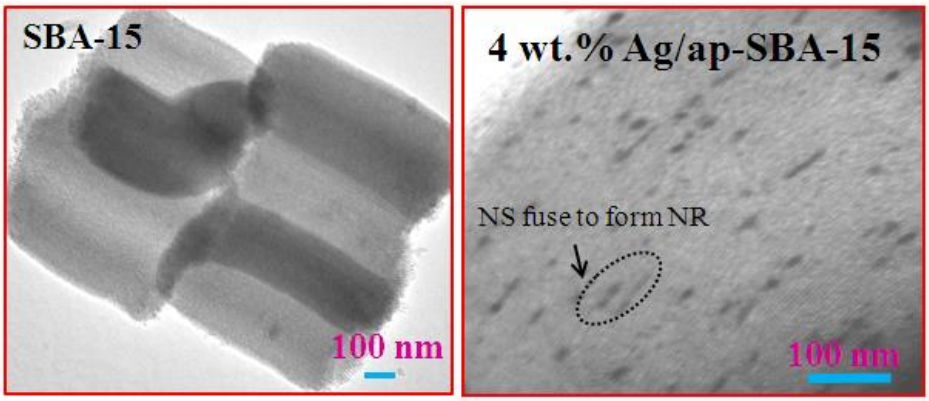

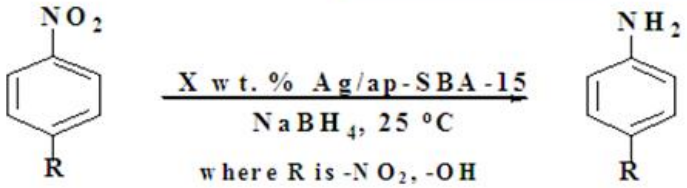

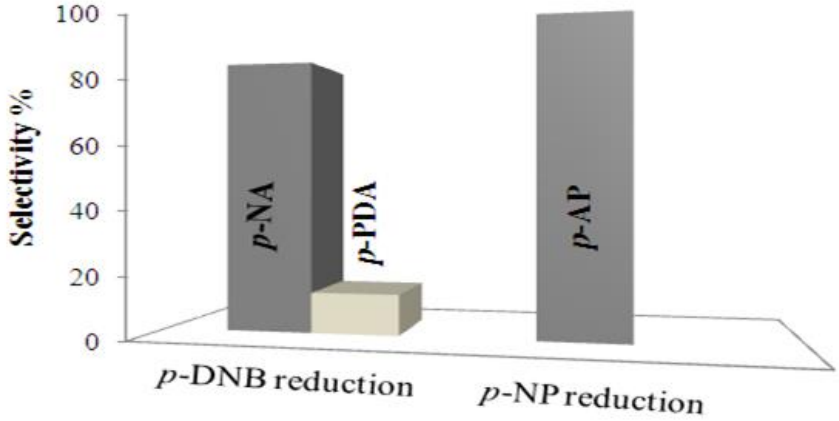

3.1 Introduction

Mesoporous silica like SBA-15 offers to be an ideal hard template and host for supporting metal NPs owing to its easy synthesis, tunable pore size and high hydrothermal stability. Since SBA-15 is inert, so the incorporation of metal NPs within silica framework create active sites, thus transforming it into a potential heterogeneous catalyst to be used for a variety of reactions. There have been reports of immobilizing Ag nanostructures on SBA-15 by different methods as discussed in section 1.2.4 (chapter 1). Ag-based catalysts have been extensively employed for oxidation reactions such as oxidation of toluene (Szegedi et al., 2014), selective oxidation of 1,2-propanediol (Yang et al., 2015), partial oxidation of benzyl alcohols (Jia et al., 2012) and oxidation of carbon monoxide (Zhang et al., 2011) as Ag effectively provides surface oxygen adsorbed species which are significant for oxidation reactions. Moreover, in comparison to other transition metals, Ag has been less explored for hydrogenation particularly reduction of nitroaromatics. The hydrogenation of nitroaromatics leads to the formation of functionalized anilines that form important intermediates in the field of pharmaceuticals, agrochemicals, polymers, dyes and pigments (Downing et al., 1997). These anilines are generated either through the catalytic or non-catalytic process. The non-catalytic process is associated with the generation of hazardous waste and limitations of product isolation, whereas the catalytic reduction involves the use of harsh reaction conditions (e.g., 100 ^{o}C temperature, hydrogen sources such as CO/H_2O, NH_2NH_2) with prolonged reaction times and poor reducibility. Furthermore, due to high surface energy Ag NPs tend to form large agglomerates on the surface of support leading to a reduction of surface area and active sites for catalytic reactions. Thus, the size, as well as the diversity of the NPs incorporated within the support are the crucial factors governing their catalytic efficiency for different industrially important reactions, which are indirectly influenced by the amount of metal loaded on the siliceous host. In this context, to gain insight into the changes associated with the surface, shape, size and dispersion ability of metal loaded SBA-15 nanocomposites as a result of a change in metal loading, Ag-loaded SBA-15 nanocomposites with 1-5 and 10 wt. % loading was prepared under inert atmosphere (nitrogen) and their catalytic activity was evaluated for nitroaromatic reduction. Moreover, changes in the various physicochemical and catalytic parameters of Au, Ag and Cu loaded SBA-15 nanocomposites pertaining to 4 wt. % metal impregnation has also been compared.

3.2 Experimental Section

3.2.1 Synthesis and characterization of Ag/ap-SBA-15 nanocomposites

The preparation and characterization techniques used for the synthesis of Ag/ap-SBA-15 nanocomposites have been described in section 1.3.2-1.3.4 and 1.3.6 (Chapter 1).

3.2.2 Catalytic activity

The catalytic activity of the Ag/ap-SBA-15 nanocomposites has been evaluated for the reduction of *p*-DNB and *p*-NP (3 mM) as per procedure given in section 1.3.7 (chapter 1). Reaction samples were analyzed by HPLC as explained in section 1.3.6.11 (chapter 1).

3.3 Results and discussion

3.3.1 Physicochemical properties of Ag/ap-SBA-15 nanocomposites

A series of Ag/ap-SBA-15 nanocomposites with Ag loadings varying from 1-5 and 10 wt. % were prepared by a post modified approach. The actual loading of Ag was found to be very close to the amount of preparation (Table 3.1), as anticipated indicating quantitative Ag deposition on the mesoporous support.

3.3.2 Optical properties

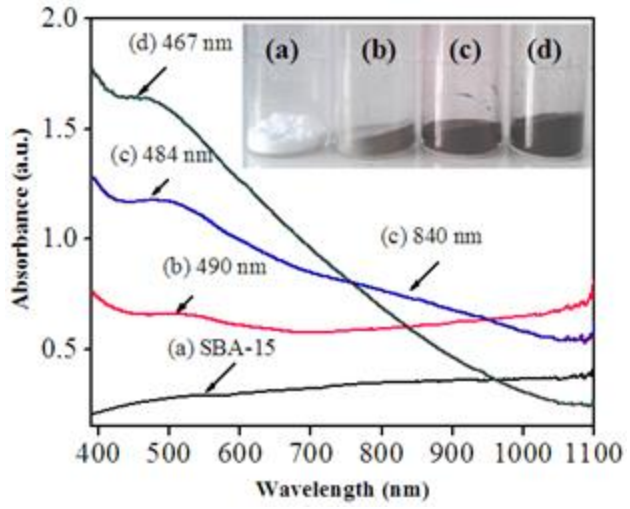

Fig. 3.1 Solid state absorption spectra of **(a)** bare SBA-15, **(b)** 1 wt. % Ag/ap-SBA-15, **(c)** 4 wt. % Ag/ap-SBA-15 and **(d)** 10 wt. % Ag/ap-SBA-15 catalysts.

Solid state UV-visible absorbance spectra of prepared nanocomposites (Fig. 3.1) displayed a broad band at 490 nm for 1 wt. % Ag impregnation while no band was observed for bare SBA-15. The appearance of a broad band in the range of 450-500 nm is in conformity with the characteristic absorbance of metallic Ag NPs (Chen et al., 2011). As the Ag loading was increased to 4 wt. %, this band blue shifted from 490 nm to 484 nm and a weak absorption band also appeared at ~840 nm indicating the formation of anisotropic NPs within the mesoporous matrix. Such differences in absorption spectra indicate that with the increase in Ag loading change in the morphology of Ag nanostructures takes place. The analogous report has been published in the literature (Huang et al., 2011). With increased

Ag loading to 10 wt. %, the transverse band at 480 nm further blue shifted to 467 nm indicating a decrease in the diameter of anisotropic Ag NPs formed within the mesoporous channels with a red shift of longitudinal band expected to be present above 1100 nm. Similarly, change in the shape of Au nano species loaded on SBA-15 nanocomposites from nanospheres (NS) to nanorods (NR) was observed at higher Au loading (section 2.3.1, chapter 2). Gao et al., (2011) also reported that an increase in the aspect ratio of Au, Ag, Pt and Pd NR was accompanied by the blue shift of transverse band and red shift of longitudinal band for template synthesis of metal NR in silica nanotubes. Moreover, with an increase in Ag loading from 1 to 10 wt. %, an increase in absorption intensity of prepared materials and change in the color of prepared materials to fine dark gray colored (10 wt. % Ag loading) in comparison to white colored bare SBA-15 was observed implying the inclusion of Ag within mesoporous sieves.

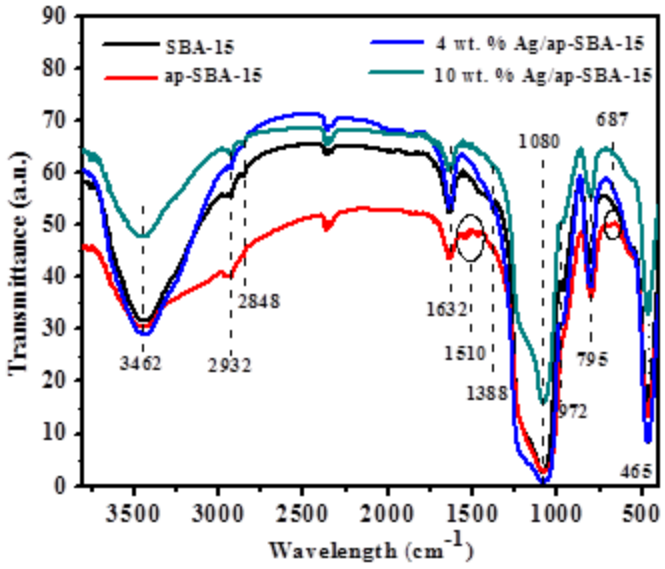

Fig. 3.2 FTIR spectra of SBA-15, ap-SBA-15 and various wt. % Ag/ap-SBA-15 catalysts.

The FTIR spectra of SBA-15 (Fig. 3.2) represented its characteristic bands as discussed in section 2.3.1 (chapter 2). However, the three weak absorption bands at 1080, 795 and 465 cm^{-1} conformed to asymmetric and symmetric stretching vibration of Si-O-Si framework of SBA-15 (Han et al., 2012). Moreover, SBA-15 modified with APTMS showed weak additional bands at 687 and 1510 cm^{-1} assigned to N-H and $–NH_2$ bending vibrations of $–NH_2$ groups and a peak at 2932 cm^{-1} and 2848 cm^{-1} assignable to the C-H stretching modes of $–CH_2$ in ap-SBA-15 in comparison to bare SBA-15 (Wang et al., 2005). As Ag does not exhibit any absorption in the IR region (Chi et al., 2012), similar spectra were observed for 4 wt. % and 10 wt. % Ag/ap-SBA-15 indicating no structural deformation of SBA-15 after surface functionalization with APTMS and Ag loading. However, the decrease in the absorption intensities with increased Ag loading was observed, suggesting the onset of crystallinity due to

the incorporation of Ag within the mesoporous sieves. Decrease in intensity due to the onset of crystallization has also been reported in SBA-15 loaded Au, Pd and Pt nanocomposites (El-Sheikh et al., 2013).

3.3.3 Surface structural morphology:

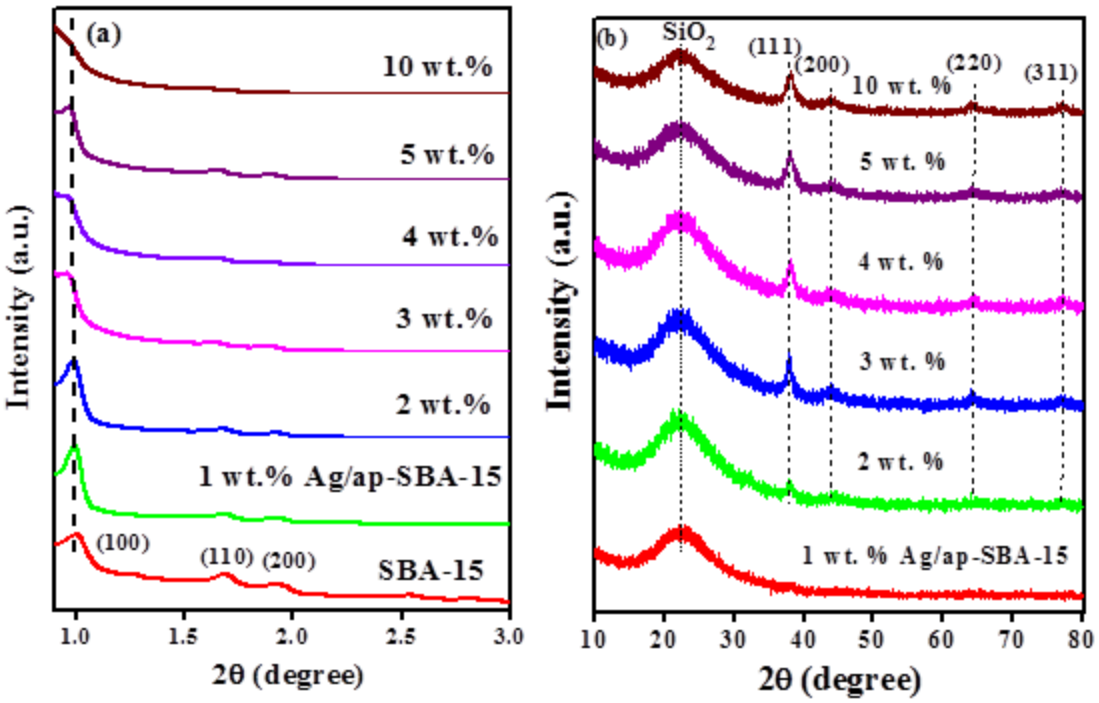

Fig. 3.3 (a) Low angle and **(b)** wide angle XRD patterns of bare SBA-15 and various wt. % Ag loaded ap-SBA-15 catalysts.

Low angle XRD patterns of all samples (Fig. 3.3a) exhibited three characteristic peaks of SBA-15 (as discussed in chapter 2, section 2.3.2) indicating retention of long range ordering of mesoporous structure after functionalization with APTMS and Ag loading. However, a decrease in the diffraction intensities of the peaks was observed with Ag loading in comparison to SBA-15 which is attributed to the pore filling effect, well consistent with the previous reports (Petkov et al., 2005; Yang et al., 2002). These results are in consonance with the FTIR studies. With the increase in Ag content, the peak corresponding to 100 plane shifted to the lower angle from 1.00^{o} to 0.96^{o} suggesting the development of tensile strain (Table 3.1) possibly due to the introduction of Ag NPs within the mesopores of SBA-15 leading to their slight expansion. This is further supported by the observed increase in structural parameters viz., unit cell parameter (a_o), pore wall thickness and d-spacing (Table 3.1) of various wt. % Ag/ap-SBA-15 samples

relative to SBA-15. An increase in the structural parameters further indicates the different dispersibility as well as the arrangement of Ag NPs within/outside the mesopores, which is greatly influenced by Ag loading. The maximum increase in d_{100} spacing and unit cell parameter (a_o) to 9.11 nm and 10.51 nm was observed for nanocomposites with 4 wt. % Ag loading relative to 8.79 nm and 10.15 nm of bare SBA-15 respectively.

Wide angle XRD patterns of 1-10 wt. % Ag-loaded ap-SBA-15 nanocomposites (Fig. 3.3b) exhibited a characteristic band of silica at $2\theta = 22^o$ and four diffraction peaks at 38.3^o, 44.3^o, 64.6^o, 77.5^o indexed to (111), (200), (220) and (311) lattice planes of cubic structure of Ag [JCPDS: 04–0783] respectively, confirming the presence of Ag NPs in SBA-15. No diffraction peaks were observed for 1 wt. % of Ag loading implying that highly dispersed Ag species may be present in the silica framework. Zhang et al., (2012) and Taghavimoghaddam et al., (2012) also observed no peaks for samples with low metal content for nanocomposites of Cu/SBA-15 and CoO/SBA-15 respectively, suggesting the successful incorporation of highly dispersed Cu and CoO species in the silica framework. However, in the present study, with an increase in Ag loading, the spectra illustrated an increase in intensity and decrease in the FWHM (Full width at half maxima) of peaks indicating an increase in the size of incorporating Ag NPs and increased crystallinity of the prepared materials. Xie et al., (2008) and Yin et al., (2011) also reported the increase in the intensities, sharpness, and a decrease in FWHM of peaks with increased Ag loading for Ag/SBA-15 and Ag/MCM-41 materials. Moreover, the average particle size of prepared Ag/ap-SBA-15 samples was found to be 6.7 nm, 7.7 nm, 8.1 nm, 7.6 nm, 7.6 nm for 2, 3, 4, 5 and 10 wt. % Ag loading as estimated from the Scherer equation for Ag (111) peak. However, the presence of an intensified (111) peak to a much broader (200) peak in the diffraction pattern of 4 wt. % Ag/ap-SBA-15 implied a difference in particle sizes of embedded Ag NPs depending upon crystal planes. The average particle size calculated from the (111) and (200) diffraction peak was estimated to be 8.1 nm and 4.57 nm respectively, suggesting the occurrence of anisotropic Ag NPs within/on the surface of the mesoporous host. These findings are supported by absorbance studies (section 3.3.2). However for 5 and 10 wt. % Ag loading, a further change in FWHM of (111) peak was not observed, indicating no significant change in average particle size. It could thus be concluded that the 4 wt. % is the maximum amount of Ag loading that can be highly dispersed on the support. With further increase (5 and 10 wt. %) in Ag loading, incorporating Ag NPs get packed one after the other due to the restriction from the

mesochannels of the host leading to the change in the shape of NPs. These results are in

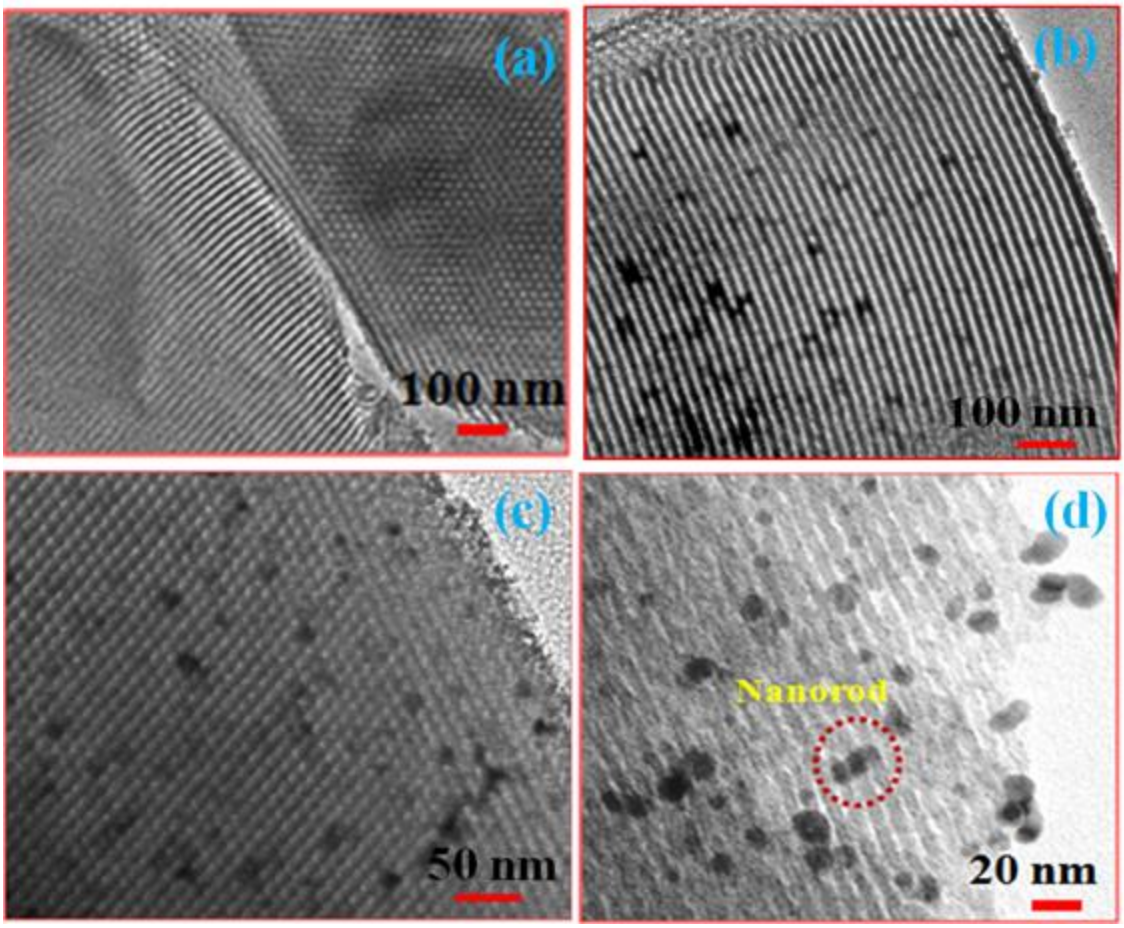

Fig. 3.4 TEM images of **(a)** SBA-15, **(b)** 1 wt. % Ag/ap-SBA-15, **(c)** 2 wt. % Ag/ap-SBA-15, and **(d)** 4 wt. % Ag/ap-SBA-15 catalyst.

agreement with TEM studies as discussed below.

TEM micrographs of SBA-15 (Fig. 3.4a) depicted 2D p6mm hexagonal pore structure with long mesochannels. Small NS of size (~7 nm) and (~8 nm) were formed by impregnating 1 wt. % and 2 wt. % Ag on the mesoporous support which were dispersed and fixed evenly as dark spots within the mesochannels of SBA-15 (Fig. 3.4b, c). This further confirmed that long range ordering of mesoporous channels was not disturbed on Ag loading. These results are in agreement with low angle XRD studies. As the Ag loading was increased to 4 wt. %, some of the NS were observed on the outer surface of the support (Fig. 3.4d) whereas small NR along with NS were formed (Fig. 3.4e) within the matrix. Formation of NR resulted from the alignment of Ag NS one after the other throughout the mesoporous channels due to increased amount of Ag

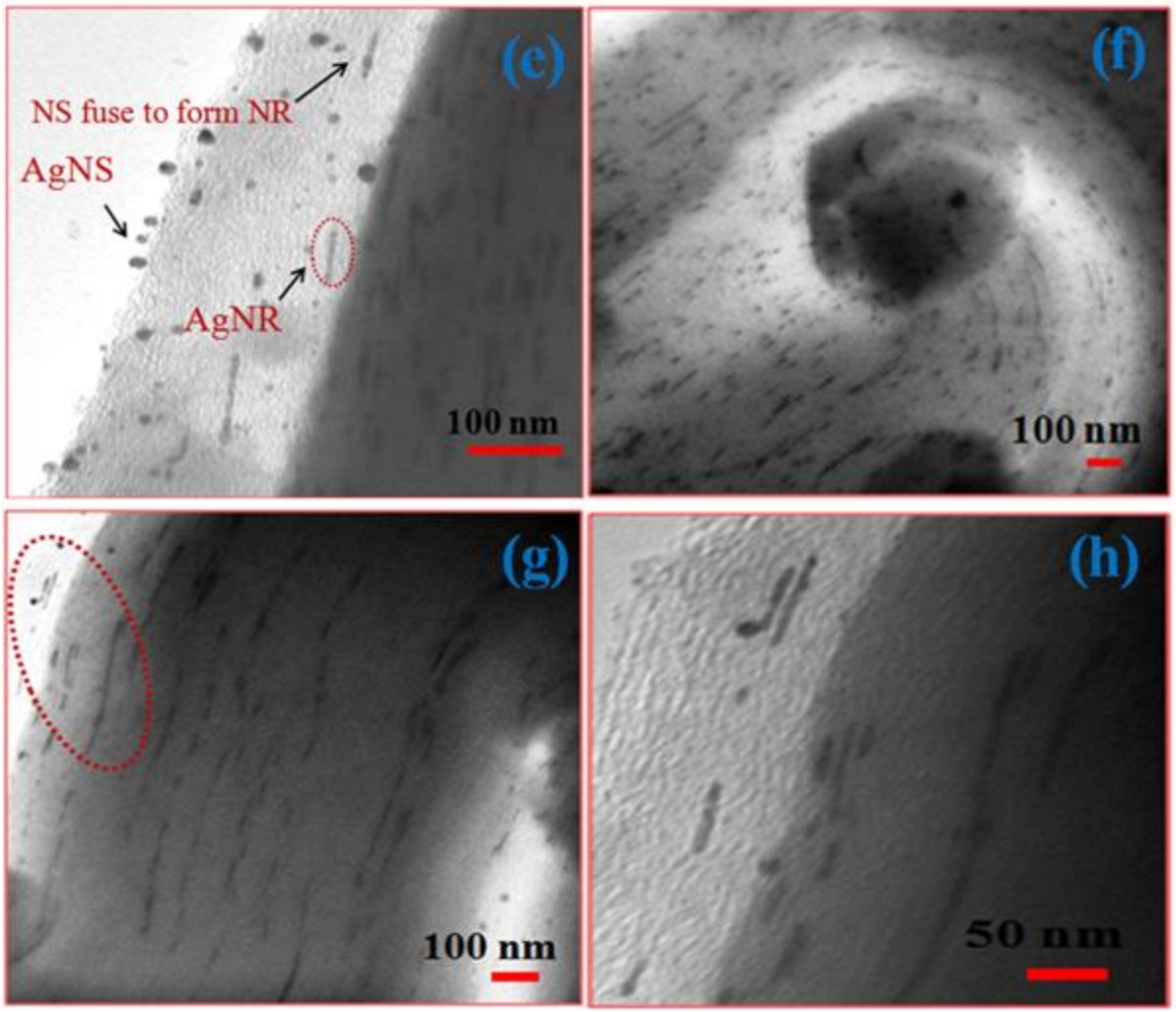

Fig. 3.4 TEM images of **(e)** 4 wt. % Ag/ap-SBA-15, **(f)** 5 wt. % Ag/ap-SBA-15 and **(g-h)** 10 wt. % Ag/ap-SBA-15 catalyst.

loading (marked in Fig. 3.4e). This can be explained as that mesoporous host acted as a limiting factor in restraining the growth of Ag nanostructures in one dimension. On the other hand, with an increase in the amount of incorporating Ag, the strain is also generated in the system. As a result of strain development and restraining behavior of the support, Ag NS gets packed one after the other throughout the host channels leading to the formation of NR. This is further supported by the presence of a weak absorption band at 840 nm in addition to the transverse band at 484 nm, for 4 wt. % Ag/ap-SBA-15 in the solid state UV-vis absorbance spectra (Fig. 3.1) justifying the formation of anisotropic nanostructures in the SBA-15 matrix. With further increase to 5 wt. % Ag loading (Fig. 3.4f), the number of small NR (aspect ratio ~12 nm) increased in the matrix resulting in the formation of larger NR (diameter ~5-8 nm and length varying from 70-300 nm)

for 10 wt. % Ag loading (Fig. 3.4g-h). Moreover, these channels remained well intact even for 10 wt. % of metal loading.

The nitrogen adsorption-desorption isotherms of SBA-15 and various wt. % Ag/ap-SBA-15 catalysts (Fig. 3.5a) depicted type IV isotherms with H1 hysteresis curves, a typical 1D hexagonal cylindrical channel of mesoporous materials (Zhao et al., 1998; Han et al., 2012). The various textural properties (Table 3.1) viz., Surface area (680 m^2/g), average pore diameter (8.2 nm) and total pore volume (1.35 cm^3/g) of bare SBA-15 were found to decrease with 1 wt. % Ag impregnation indicating partial filling of mesopores of SBA-15 with Ag NPs. However, an unexpected increase in the surface area of 4 wt. % Ag/ap-SBA-15 (708 m^2/g) relative to SBA-15 (680 m^2/g) was observed which may be due to the fact that with the increased amount of Ag impregnation, some of Ag NPs may have deposited on the external surface besides partial filling up of pores which are also clearly visible in the TEM micrographs (Fig. 3.4e). With further increase in Ag loading to 10 wt. % decrease in surface area was observed, attributed to the blocking of mesopores with the increased amount of silver. Similar findings have been reported by Wang et al., (2010) for higher loadings of cobalt on mesoporous silica.

Table 3.1 Physicochemical parameters for bare SBA-15 and various wt. % Ag-loaded ap/SBA-15 nanocomposites

Sample	Ag[a] (wt. %)	d-spacing d_{100} (nm)	Unit cell parameter a_o (nm)[b]	Wall thickness d_w (nm)[c]	Surface area (m^2/g)	Pore volume (cm^3/g)	Pore size (nm)	Strain
SBA-15		8.79	10.15	1.36	680	1.35	8.21	
1 wt. % Ag/ap-SBA-15	0.76	8.89	10.26	1.37	466	0.79	7.31	0.0387
2 wt. % Ag/ap-SBA-15	2.27	8.91	10.28	1.37	440	0.76	7.29	0.0387
3 wt.% Ag/ap-SBA-15	2.98	9.08	10.48	1.40	409	0.74	7.21	0.0388
4 wt. % Ag/ap-SBA-15	4.12	9.11	10.51	140	708	1.27	7.44	0.0483
5 wt.% Ag/ap-SBA-15	4.88	9.10	10.50	1.40	424	0.73	7.39	0.0482
10 wt.% Ag/ap-SBA-15	8.21	9.06	10.46	1.40	385	0.71	7.36	0.0396

[a] Ag loading determined by MP-AES
[b] $a_0 = 2/3^{1/2} d_{100}$, [c] $d_w = a_0 - d_{100}$

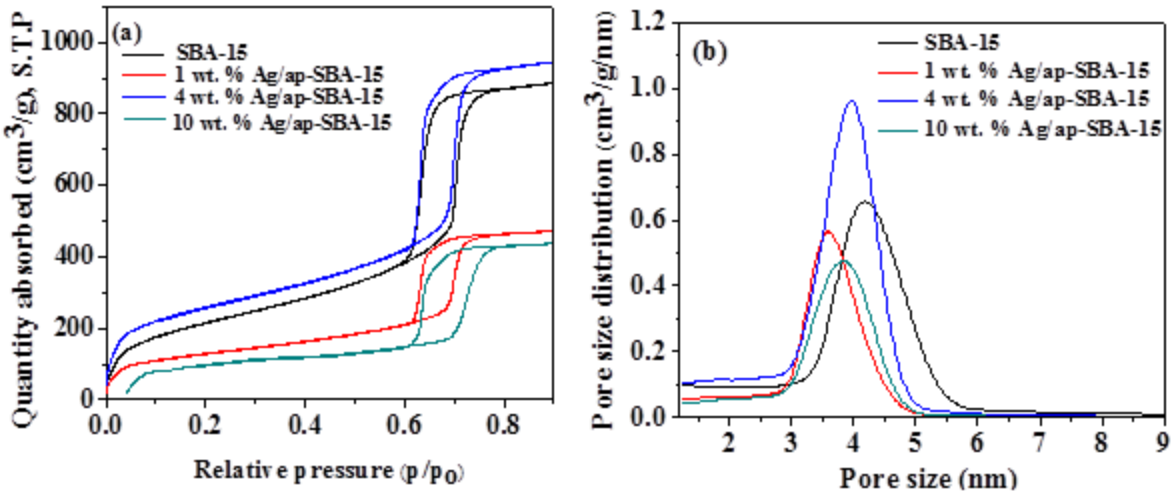

Fig. 3.5 (a) Nitrogen adsorption- desorption isotherms and **(b)** pore size distribution of bare SBA-15 and various wt. % Ag/ap-SBA-15 catalyst.

3.3.4 Thermal properties

The thermogravimetric analysis, curve (Fig. 3.6) is divided into three weight loss zones. The first weight loss zone showed a degradation up to 100 ^{o}C with a weight loss of 5 % for ap-SBA-15, 12 % and ~14 % for 4 wt. % and 10 wt. % Ag/ap-SBA-15 respectively that can be assigned to the loss of physically absorbed water on the surface of silica. The second wt. loss (~ 2-3 % for ap-SBA-15, 4 wt. % and 10 wt. % Ag/ap-SBA-15) within a range of 100-300 ^{o}C can be

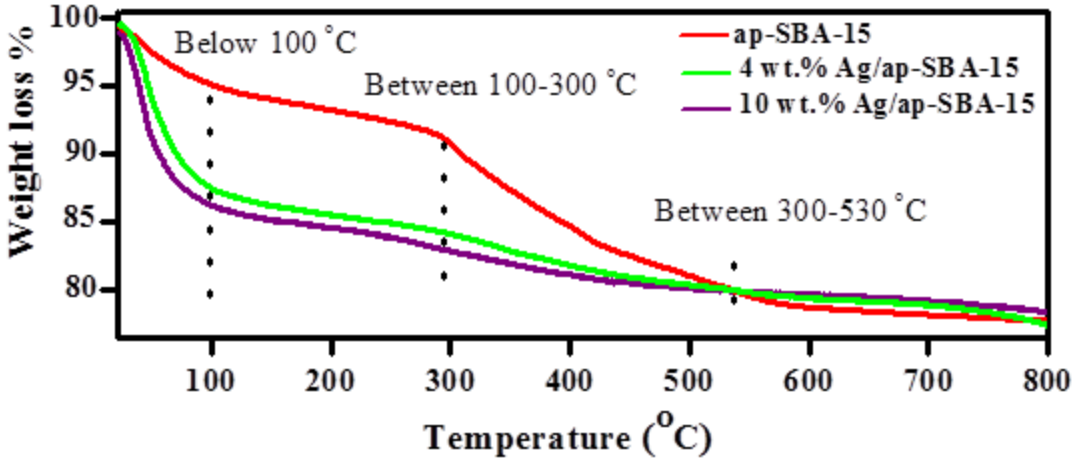

Fig. 3.6 TGA curve of ap-SBA-15, 4 wt. % Ag/ap-SBA-15 and 10 wt. % Ag/ap-SBA-15 catalysts.

associated with the decomposition of copolymer surfactant respectively (Zhu et al., 2013). However, third weight loss (~ 12 %, ~5 % and ~3 % for ap-SBA-15, 4 wt. % and 10 wt. % Ag/ap-SBA-15) was observed between 300-530 ^{o}C, due to the decomposition of aminopropyl groups incorporated in ap-SBA-15 (Subbaramaiah et al., 2013; Wang et al., 2005). Further weight loss above 530 ^{o}C can be attributed to the decomposition of carbon species derived from aminopropyl groups (Zhao et al., 1997). It is thus concluded that the prepared materials were found to be thermally stable at a temperature ≤ 550 ^{o}C and can also be employed as catalysts for reactions taking place at high temperatures.

3.3.5 Catalytic activity

The various wt. % Ag/ap-SBA-15 composites exhibited linear plots for change in concentration ($-\ln C/C_o$ versus time) of *p*-DNB (Scheme 3.1, Fig. 3.7a) and *p*-NP (Scheme 3.2, Fig. 3.9a) indicating pseudo first order kinetics of the reaction. All the prepared nanocomposites showed efficient catalytic activity in comparison to SBA-15 for the selective reduction of *p*-DNB to *p*-NA and *p*-PDA (Fig. 3.7b) and *p*-NP to *p*-AP (Fig. 3.9a) at room temperature with 100 % conversion in less than 40 min. and 25 min. respectively. The reduction reaction took place due to the transfer of electrons from the donor BH_4^- (adsorbed on the surface of the catalyst) to the

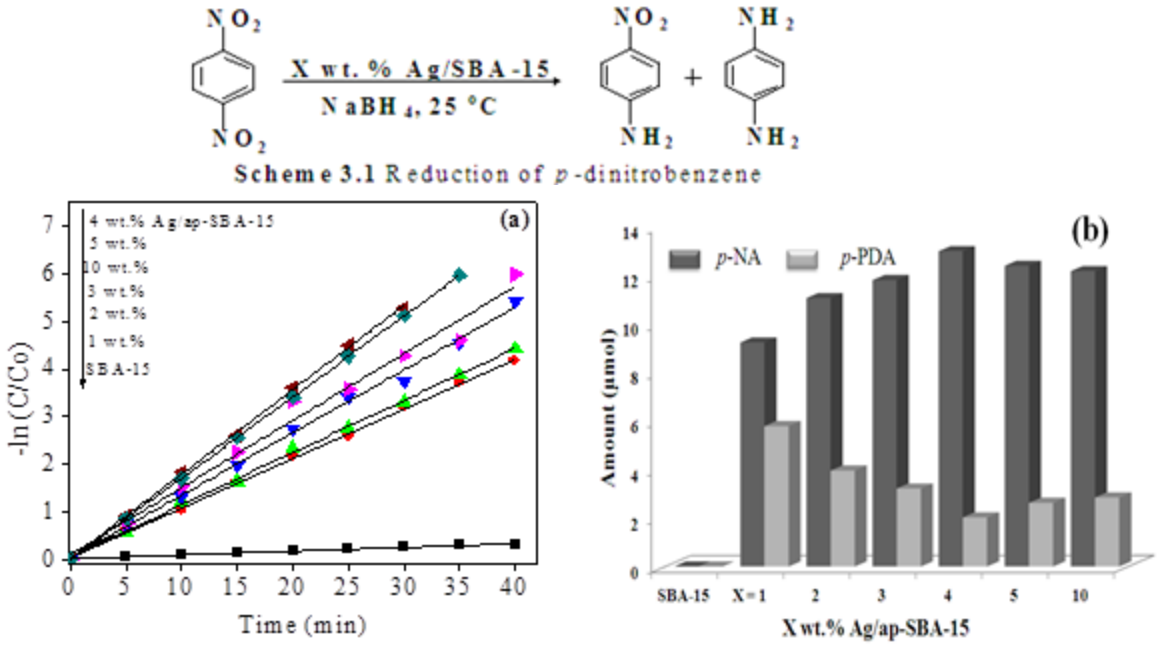

Fig. 3.7 (a) Time course graph of *p*-DNB reduction by bare and various wt. % Ag loaded ap-SBA-15 catalysts and **(b)** Product distribution of *p*-DNB reduction (3 mM) to *p*-NA and *p*-PDA respectively by bare and different wt. % Ag loaded ap-SBA-15 catalysts.

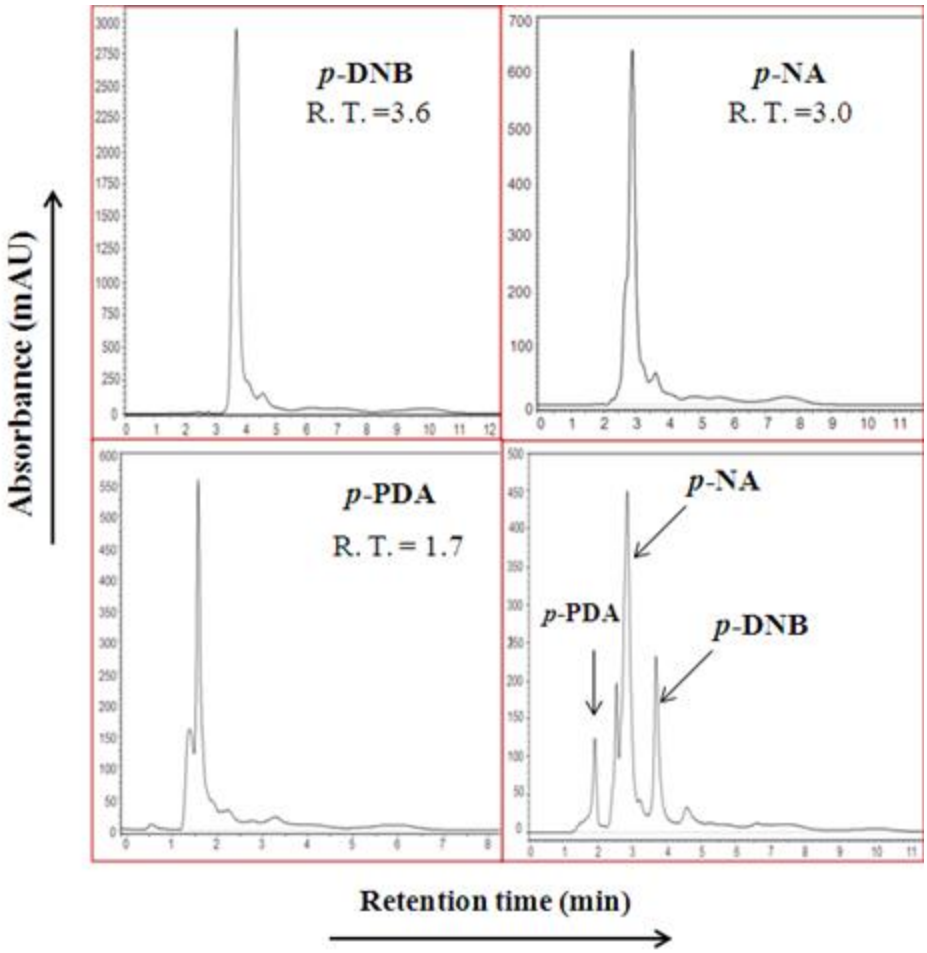

Fig. 3.8 HPLC chromatograms of reaction sample for *p*-dinitrobenzene reduction at 20 min catalyzed by 4 wt. % Ag/ap-SBA-15 catalyst.

acceptor substrate molecules, via the metal NPs, leading to the formation of hydrogen which then reduces the substrate molecules (Naik et al., 2011). So, the greater the surface area of the catalyst, the greater number of donor BH_4^- molecules will be adsorbed, faster will be the electron transfer and faster will be the catalytic process of reduction. As discussed in chapter 2, 4 wt. % Au loaded SBA-15 exhibited highest catalytic activity for the reduction of *m*-DNB with 89 % selectivity for *m*-PDA formation. Moreover, in our current study, the highest catalytic activity was exhibited by catalyst with 4 wt. % Ag loading, but with reversed selectivity (87 % selectivity for *p*-NA) for the reduction of *p*-DNB as confirmed by HPLC analysis (Fig. 3.8). Similar catalyst displayed optimum activity for *p*-NP reduction (as confirmed by HPLC analysis, Fig. 3.10) with 100% selectivity and the total time for completion of the reaction decreased till 4 wt. % Ag

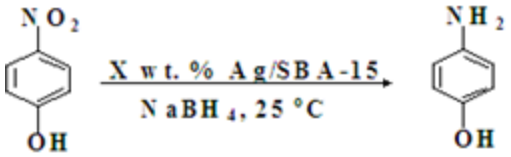

Scheme 3.2 Reduction of *p*-nitrophenol

loading and then again increased for 5 and 10 wt. %, respectively (Fig. 3.9b). The value of the rate constant was found to be 4.7×10^{-3} s^{-1} for *p*-NP and 1.803×10^{-1} s^{-1} for *p*-DNB, quite comparable with the reported rate constants (Cardenas-Lizana et al., 2010; Naik et al., 2011; Panigrahi et al., 2007) where supported Ag catalysts were used, signifying the high efficiency of the prepared catalyst. The highest catalytic activity exhibited by 4 wt. % Ag/ap-SBA-15 nanocomposite could be credited to the increase in

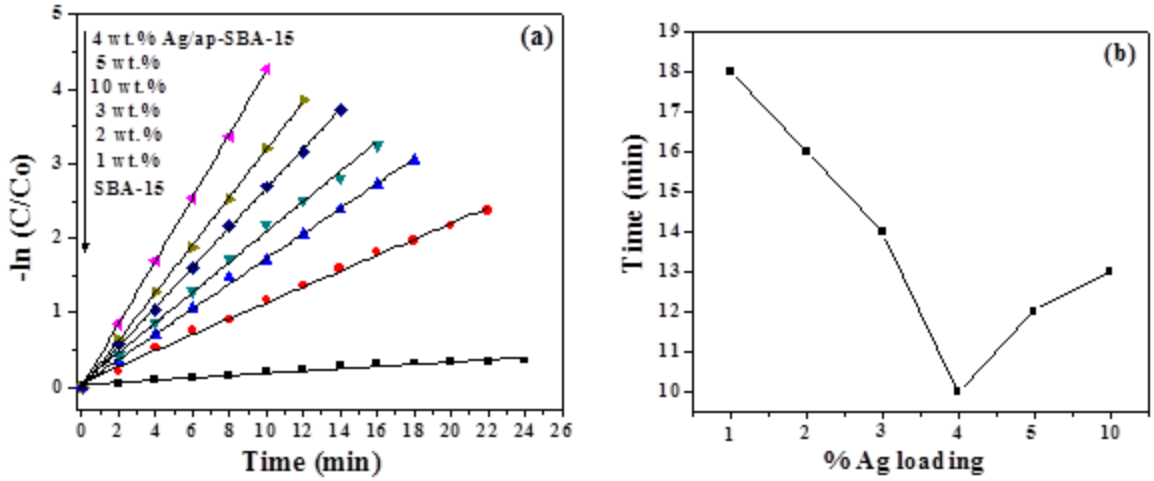

Fig. 3.9 (a) Time course graph of *p*-NP reduction by bare and various wt. % Ag loaded ap-SBA-15 catalyst and **(b)** Effect of % Ag loading on time required for completion of reduction of *p*-NP

the amount of Ag loading (till 4 wt. %) that resulted in the formation of well dispersed Ag NPs (active sites) within/on the surface of the mesopores (as suggested by TEM studies). Moreover, due to the presence of Ag NPs on the external surface besides being present within the pores (Patel et al., 2011), 4 wt. % Ag/ap-SBA-15 exhibited the unexpectedly high surface area (708 m^2/g) more than SBA-15 that resulted in comfortable accessibility of catalytically active species to the substrate molecules leading to improved catalytic activity. Similar findings have been reported by Kundu et al. (2009) that the rate of reaction is increased with the increase in surface area of the catalyst. Moreover, XRD patterns also showed 4 wt. % Ag loading to be the maximum dispersion capacity of Ag NPs on the SBA-15 support. Beyond this value, the particles get aligned and packed one after the other in the form of rod-like morphology leading to

blockage of mesopores resulting in a decrease in the catalytic activity. Thus, the decrease in catalytic activity for higher wt. % of Ag loading can be attributed to the pore blocking by an inhomogeneous distribution of the larger number of anisotropic Ag NPs within the SBA-15 matrix.

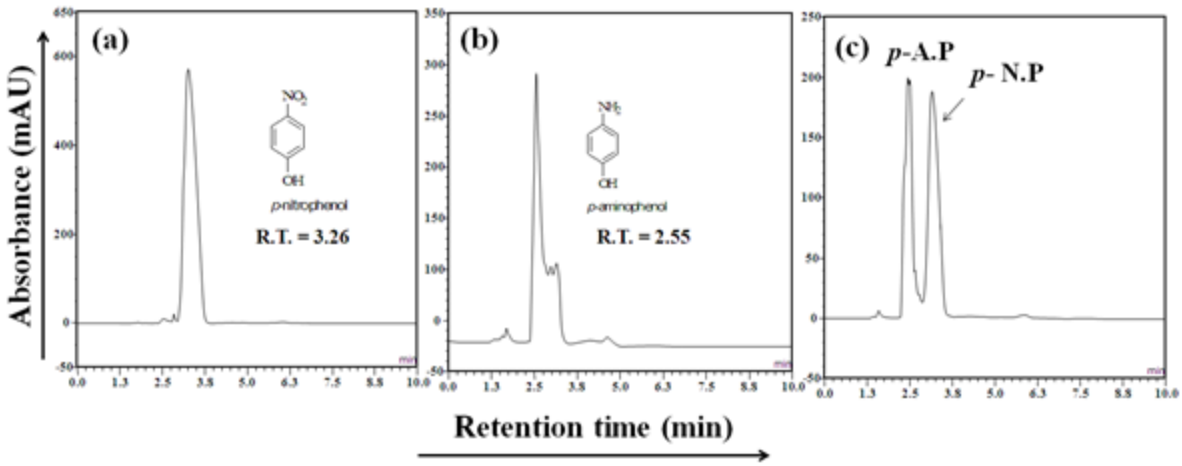

Fig. 3.10 HPLC chromatograms of reaction sample for *p*-nitrophenol reduction at 8 min. catalysed by 4 wt. % Ag/ap-SBA-15 catalyst.

This is also supported by an abrupt decrease in surface area, pore volume and pore size as illustrated by the BET studies. Liu et al. (2006) also reported the decrease in the catalytic activity for higher metal loading using Ni/SiO_2 as a catalyst for the reduction of *m*-DNB. As preparation of samples involves metal impregnation under stirring followed by thermal treatment, so different anisotropical NPs may occupy different orientations and distribution resulting in an inhomogeneous distribution of metal nano species within the support. Taghavimoghaddam et al. (2012) also reported that decrease in catalytic activity with increased Co-loading is due to the inhomogeneous distribution of CoO nano species loaded on SBA-15. In contrast, in the case of low Ag loadings, an insufficient amount of Ag dispersed within the support probably led to the generation of a lesser number of active sites that may have resulted in the lower catalytic activity. Anand et al. (2012) also reported that lower conversion observed for benzylic oxidation of alkyl substituted aromatics to ketones was due to the lower metal loading resulting in lower catalytic activity for Ag/SBA-15 nanocomposites. Moreover, the recyclability of the 4 wt. % Ag/ap-SBA-15 catalyst for *p*-DNB reduction was studied by recovering it from the reaction mixture through filtration, washing with deionized water and drying at $60^{o}C$ for 8h and a small

decrease in selectivity of 85, 82 and 79 % was observed after first, second and third successive run. These results implied that the catalyst was stable and can be reused even after three recycles. However, a small decrease in the selectivity may conform to the blockage of some of the mesopores by organic molecules during the catalytic reaction.

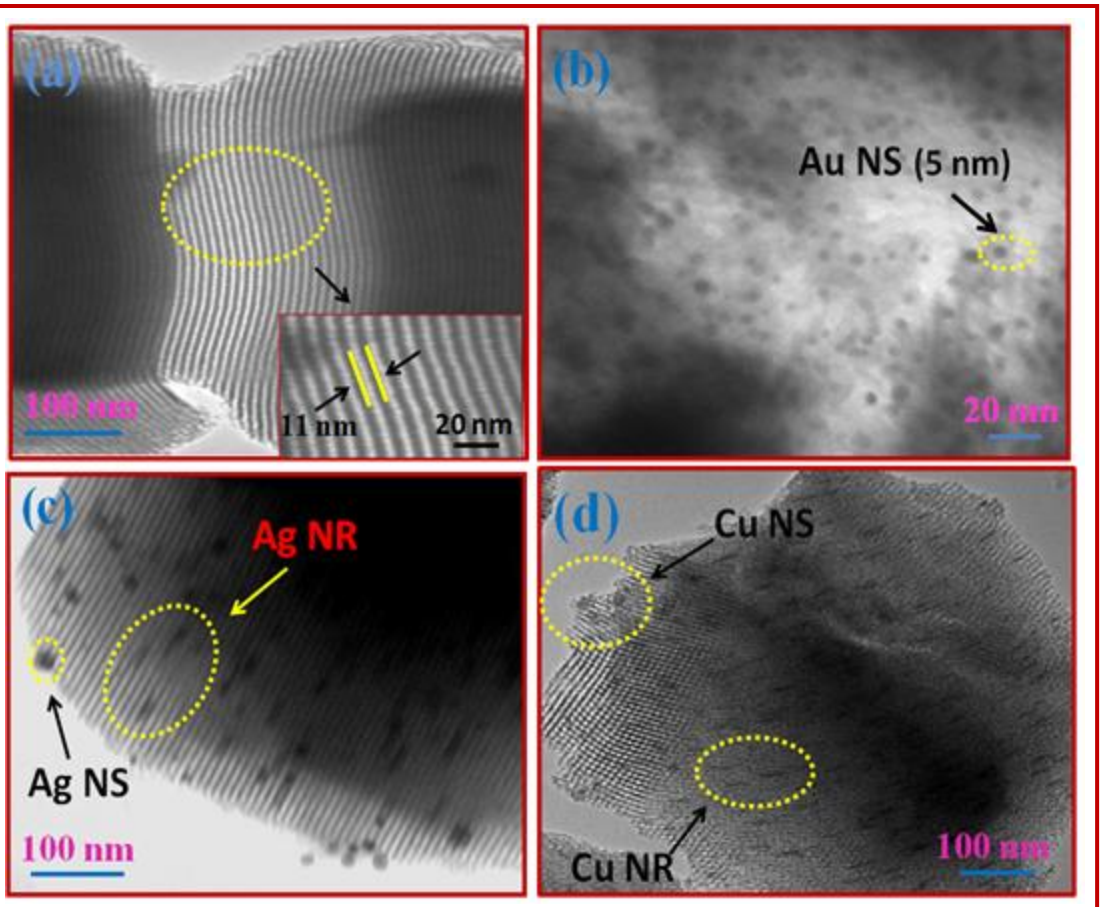

Fig. 3.12 TEM images of **(a)** SBA-15, **(b)** Au/ap-SBA-15, **(c)** Ag/ap-SBA-15 and **(d)** Cu/ap-SBA-15 catalyst.

3.3.6 Comparison of physicochemical and catalytic parameters of mesoporous SBA-15 supported coinage metal (Au, Ag and Cu) nanocomposites

Since, our studies based on SBA-15 supported Au and Ag nanocomposites showed that the catalytic activity, shape, size and dispersion density of incorporated metal NPs were significantly affected by varying the metal loading from 1-5 and 10 wt. %, respectively. Furthermore, of the prepared series of Au and Ag-loaded SBA-15 catalysts, composite with 4 wt. % Au/Ag loading exhibited efficient catalytic activity for the nitroaromatic reduction. Thus, it was interesting to compare the properties of supported Au and Ag-loaded nanocomposites

with other metals of the group as the comparison of the morphological features, physicochemical properties and catalytic activity of coinage metal loaded SBA-15 nanocomposites has seldom been reported. Moreover, progressive developments in tuning the shape and size of coinage metal NPs have also increased the chances of optimizing their geometry which ultimately affects their catalytic efficiency. Therefore, highly dispersed Au, Ag and Cu NPs pertaining to 4 wt. % metal impregnation was prepared within the channels of SBA-15 and studied for their comparative surface structural morphology and catalytic activity for dinitrobenzene reduction.

3.3.6.1 Surface structural morphology

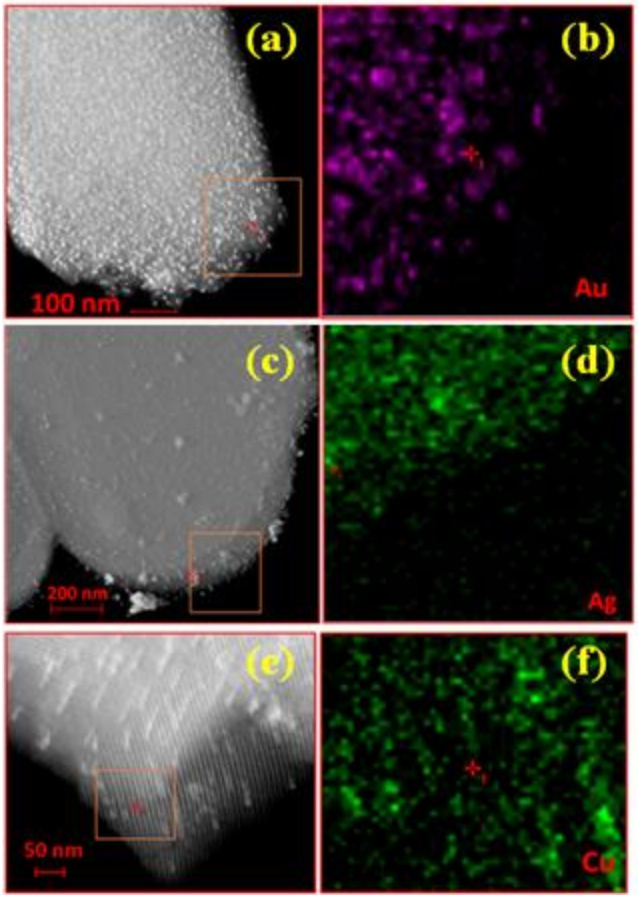

Fig. 3.13 STEM images and elemental mapping of **(a-b)** Au/ap-SBA-15, **(c-d)** Ag/ap-SBA-15 and **(e-f)** Cu/ap-SBA-15 catalyst.

TEM micrographs (Fig. 3.12) of SBA-15 depicted uniform vertical mesochannels with long range ordering without any disruption in the basic structure of siliceous host. Nanospheres (NS) were observed with Au loading where as loading of Ag and Cu resulted in the formation of small nanorod (NR) of the aspect ratio of 2 - 4 nm along with the NS depicted as dark structures homogeneously dispersed against the lighter background of the SBA-15 matrix. The average particle size of NS for Cu, Ag and Au were found to be 13, 11 and 5.5 nm respectively. Moreover, STEM images and corresponding elemental mapping of the M/ap-SBA-15 catalysts (Fig. 3.13) demonstrated the uniform dispersion of metallic NPs over the mesoporous host. HR-TEM micrographs

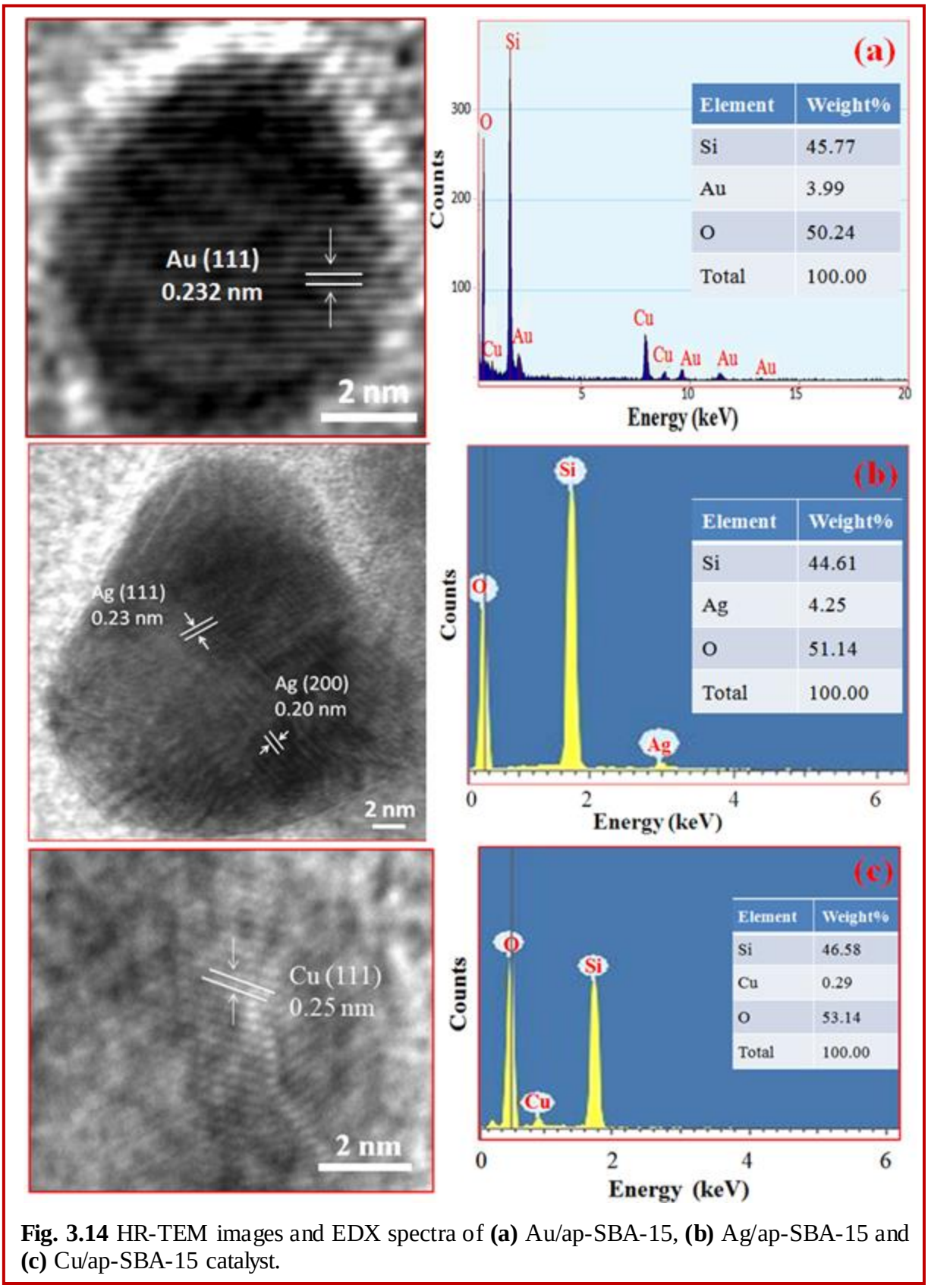

Fig. 3.14 HR-TEM images and EDX spectra of **(a)** Au/ap-SBA-15, **(b)** Ag/ap-SBA-15 and **(c)** Cu/ap-SBA-15 catalyst.

of various catalysts (Fig. 3.14) revealed that particles exhibited single crystalline structures with lattice fringes having d-spacing of 0.232 nm which is close to the spacing of 0.236 nm for Au (111) planes (Fig. 3.14a), 0.23 nm and 0.20 nm for Ag (111) and (200) planes (Fig. 3.14b). However, lattice fringes giving d-spacing of 0.25 nm were observed for Cu/ap-SBA-15 catalyst in agreement with that of crystalline CuO (111) plane (Fig. 3.14c) revealing that metallic CuNPs may not be formed, but due to oxidation of Cu highly dispersed and crystalline CuO may have been formed within/on the surface of the SBA-15. The corresponding EDX analysis further confirmed the presence of Au, Ag and CuO on the mesoporous support with Au, Ag and Cu showing 3.9, 4.25 and 0.29 wt. % loading.

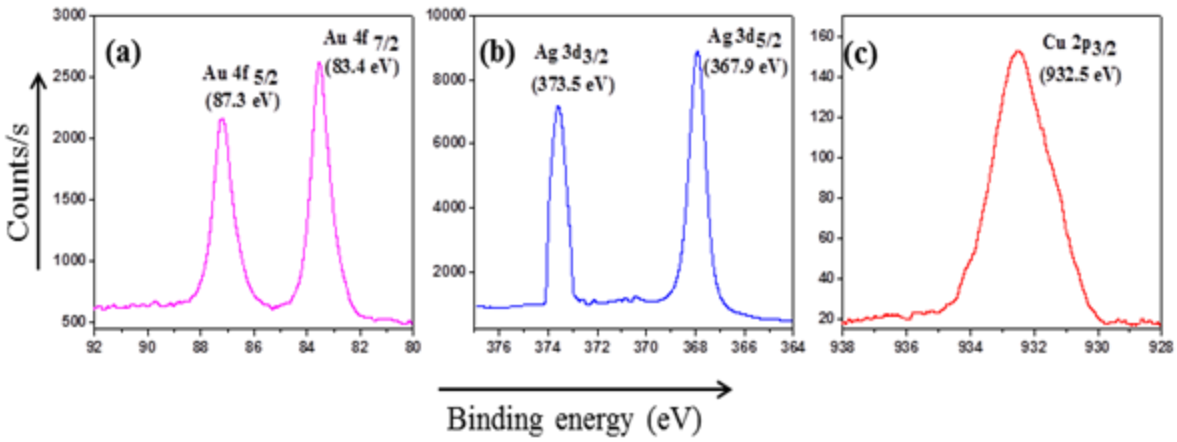

Fig. 3.15 XPS spectra of **(a)** Au/ap-SBA-15, **(b)** Ag/ap-SBA-15 and **(c)** Cu/ap-SBA-15 catalyst.

The incorporation of metallic species within SBA-15 and the elemental state of the nanocomposite materials was analyzed using XPS (Fig. 3.15). Au/ap-SBA-15 catalyst (Fig. 3.15a) showed a doublet at 83.4 eV and 87.3 eV corresponding to Au $4f_{7/2}$ and Au $4f_{5/2}$ peaks respectively, implying the presence of metallic Au^{o} within the catalyst (Liu et al., 2008; El-Sheikh et al., 2013). Moreover, Ag/ap-SBA-15 catalyst exhibited binding energy of 367.9 eV and 373.5 eV that corresponds to Ag $3d_{5/2}$ and Ag $3d_{3/2}$ indicating Ag^{o} state and is in consonance with the reported data (Strzałka et al., 2013; Xie et al., 2014) of metallic Ag (Fig. 3.15b). However, in Cu/ap-SBA-15 (Fig. 3.15c), the Cu $2p_{3/2}$ peak appeared at a binding energy of 932.5 eV implying the presence of either Cu^{0} or Cu^{+1} species (Sarkar et al., 2014) suggesting that Cu

may have been oxidized to Cu^{+1} by oxygen at high temperature. Moreover, being highly susceptible to oxidation, there is a possibility that it may further oxidize back to Cu^{+2} species

3.3.6.2 ***Catalytic activity***

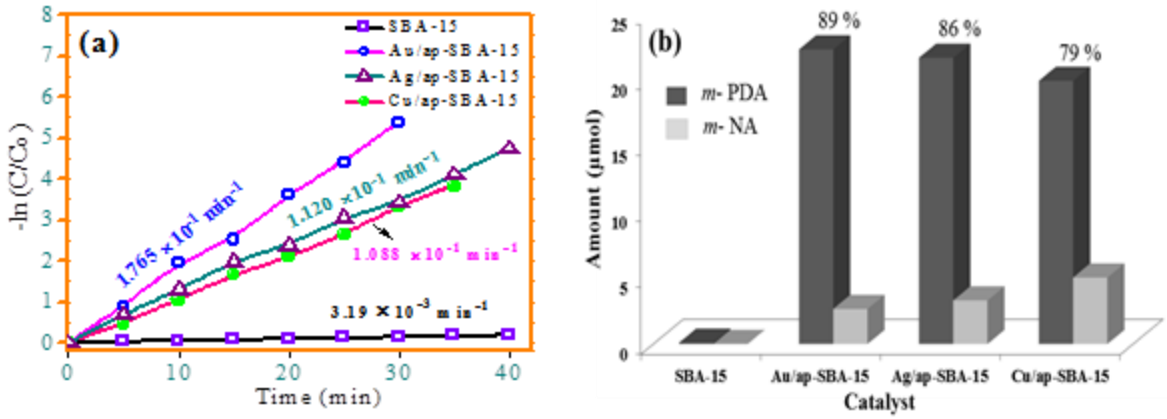

Fig. 3.16 (a) Time course graph of reduction of *m*-DNB (-ln C/C_o) by SBA-15 and M/ap-SBA-15 catalysts and **(b)** Product distribution of *m*-DNB reduction (5 mM) to *m*-PDA and *m*-NA by SBA-15 and M/ap-SBA-15 catalysts.

Comparison of catalytic activity of coinage metal loaded SBA-15 nanocomposites showed linear plots (Fig. 3.16a) for change in concentration of *m*-DNB (–ln C/C_o versus time) for all metal loaded catalysts indicating pseudo first order kinetics. With metal loading catalytic activity improved abruptly in comparison to SBA-15 establishing the fact that metal NPs were real active sites. However, the order of catalytic activity was found to be dependent upon nature of metal, size and metallic dispersion which in turn rely on the synthetic conditions. Among all the prepared catalysts, Au and Ag were reduced to the metallic state with Au exhibiting the smallest particle size, whereas Cu being susceptible to oxidation formed large CuO NPs (as revealed by EDX analysis). Thus, Au with smallest particle size and better metallic dispersion produced the greatest number of active metal sites resulting in an enhanced reaction rate and selectivity. Rojas et al. (2011) also reported the influence of particle size and metal dispersion on the catalytic activity of supported platinum catalyst for the reduction of *m*-DNB. However, lower catalytic activity for Ag/ap-SBA-15 in comparison to Au/ap-SBA-15 can be explained on the basis of comparatively large sized NPs embedded on the external surface resulting in lesser number of exposed active sites and hence decreased reaction rate. In the case of Cu/ap-SBA-15, Cu is being highly reactive got oxidized to large CuO NPs, present on the external surface that does not allow reactant molecules to access all the reaction sites resulting in lower catalytic activity.

It is thus represented that mesoporous SBA-15 having negligible reactivity could be effectively utilized by metal nanoparticles dispersion into pores of SBA-15 and its catalytic activity could be well tuned to the desired reach as a function of metal loading, nature of metal and its dispersion density. Of the Ag/ap-SBA-15 nanocomposites, a catalyst with 4 wt. % Ag loading is found to be catalytically most active exhibiting 87 % selectivity for p-nitroaniline and 100 % selectivity for p-aminophenol formation. Moreover, comparison of physicochemical properties and reactivity of supported coinage metal nanocomposites demonstrated Au loaded SBA-15 as catalytically most active, as compared to Ag and Cu loaded SBA-15 for nitroaromatic reduction. The conversion of nitro compounds to their corresponding amines and high recyclability further established high activity of the catalyst.

3.4 References

Anand, N., Reddy, K.H.P., Prasad, G.V.S., Rao, K.S.R. and Burri, D.R., 2012. Selective benzylic oxidation of alkyl substituted aromatics to ketones over Ag/SBA-15 catalysts. Catalysis Communications, 23, pp.5-9.

Cárdenas-Lizana, F., de Pedro, Z.M., Gomez-Quero, S. and Keane, M.A., 2010. Gas phase hydrogenation of nitroarenes: A comparison of the catalytic action of titania supported gold and silver. Journal of Molecular Catalysis A: Chemical, 326(1), pp.48-54.

Chen, D., Qu, Z., Shen, S., Li, X., Shi, Y., Wang, Y., Fu, Q. and Wu, J., 2011. Comparative studies of silver based catalysts supported on different supports for the oxidation of formaldehyde. Catalysis Today, 175(1), pp.338-345.

Chi, Y., Zhao, L., Yuan, Q., Li, Y., Zhang, J., Tu, J., Li, N. and Li, X., 2012. Facile encapsulation of monodispersed silver nanoparticles in mesoporous compounds. Chemical Engineering Journal, 195, pp.254-260.

Downing, R.S., Kunkeler, P.J. and Van Bekkum, H., 1997. Catalytic syntheses of aromatic amines. Catalysis Today, 37(2), pp.121-136.

El-Sheikh, S.M., Ismail, A.A. and Al-Sharab, J.F., 2013. Catalytic reduction of p-nitrophenol over precious metals/highly ordered mesoporous silica. New Journal of Chemistry, 37(8), pp.2399-2407.

Gao, C., Zhang, Q., Lu, Z. and Yin, Y., 2011. Templated synthesis of metal nanorods in silica nanotubes. Journal of the American Chemical Society,133(49), pp.19706-19709.

Han, J., Fang, P., Jiang, W., Li, L. and Guo, R., 2012. Ag-nanoparticle-loaded mesoporous silica: spontaneous formation of Ag nanoparticles and mesoporous silica SBA-15 by a one-pot strategy and their catalytic applications. Langmuir, 28(10), pp.4768-4775.

Huang, X., Dong, W., Wang, G., Yang, M., Tan, L., Feng, Y. and Zhang, X., 2011. Synthesis of confined Ag nanowires within mesoporous silica via double solvent technique and their catalytic properties. Journal of Colloid and Interface Science, 359, pp.40-46.

Jia, L., Zhang, S., Gu, F., Ping, Y., Guo, X., Zhong, Z. and Su, F., 2012. Highly selective gas-phase oxidation of benzyl alcohol to benzaldehyde over silver-containing hexagonal mesoporous silica. Microporous and Mesoporous Materials, 149(1), pp.158-165.

Kundu, S., Lau, S. and Liang, H., 2009. Shape-controlled catalysis by cetyltrimethylammonium bromide terminated gold nanospheres, nanorods, and nanoprisms. The Journal of Physical Chemistry C, 113(13), pp.5150-5156.

Liu, X., Wang, A., Yang, X., Zhang, T., Mou, C.Y., Su, D.S. and Li, J., 2008. Synthesis of thermally stable and highly active bimetallic Au-Ag nanoparticles on inert supports. Chemistry of Materials, 21(2), pp.410-418.

Naik, B., Hazra, S., Prasad, V.S. and Ghosh, N.N., 2011. Synthesis of Ag nanoparticles within the pores of SBA-15: an efficient catalyst for reduction of 4-nitrophenol. Catalysis Communications, 12(12), pp.1104-1108.

Panigrahi, S., Basu, S., Praharaj, S., Pande, S., Jana, S., Pal, A., Ghosh, S.K. and Pal, T., 2007. Synthesis and size-selective catalysis by supported gold nanoparticles: study on heterogeneous and homogeneous catalytic process. The Journal of Physical Chemistry C, 111(12), pp.4596-4605.

Patel, A., Rufford, T.E., Rudolph, V. and Zhu, Z., 2011. Selective catalytic reduction of NO by CO over CuO supported on SBA-15: Effect of CuO loading on the activity of catalysts. Catalysis today, 166(1), pp.188-193.

Petkov, N., Stock, N. and Bein, T., 2005. Gold electroless reduction in nanosized channels of thiol-modified SBA-15 material. The Journal of Physical Chemistry B, 109(21), pp.10737-10743.

Rojas, H., Borda, G., Reyes, P., Brijaldo, M. and Valencia, J., 2011. Liquid-phase hydrogenation of m-dinitrobenzene over platinum catalysts. Journal of the Chilean Chemical Society, 56(3), pp.793-798.

Sarkar, B., Pendem, C., Konathala, L.S., Tiwari, R., Sasaki, T. and Bal, R., 2014. Cu nanoclusters supported on nanocrystalline SiO_2–MnO_2: a bifunctional catalyst for the one-step conversion of glycerol to acrylic acid.Chemical Communications, 50(68), pp.9707-9710.

Subbaramaiah, V., Srivastava, V.C. and Mall, I.D., 2013. Optimization of reaction parameters and kinetic modeling of catalytic wet peroxidation of picoline by Cu/SBA-15. Industrial & Engineering Chemistry Research, 52(26), pp.9021-9029.

Szegedi, Á., Popova, M., Valyon, J., Guarnaccio, A., De Stefanis, A., De Bonis, A., Orlando, S., Sansone, M., Teghil, R. and Santagata, A., 2014. Comparison of silver NPs confined in nanoporous silica prepared by chemical synthesis and by ultra-short pulsed laser ablation in liquid. Applied Physics A, 117(1), pp.55-62.

Taghavimoghaddam, J., Knowles, G.P. and Chaffee, A.L., 2012. Preparation and characterization of mesoporous silica supported cobalt oxide as a catalyst for the oxidation of cyclohexanol. Journal of Molecular Catalysis A: Chemical, 358, pp.79-88.

Wang, X., Lin, K.S., Chan, J.C. and Cheng, S., 2005. Direct synthesis and catalytic applications of ordered large pore aminopropyl-functionalized SBA-15 mesoporous materials. The Journal of Physical Chemistry B, 109(5), pp.1763-1769.

Wang, Y., Hou, B., Chen, J. and Sun, Y., 2010. Influence of pore regularity on Fischer-Tropsch synthesis with Co/SiO_2 Catalysts. Reaction Kinetics, Mechanisms and Catalysis, 102(1), pp.155-164.

Xie, Y., Quinlivan, S. and Asefa, T., 2008. Tuning metal nanostructures in mesoporous silica by a simple change of metal complexes and by reduction with grafted imines and hemiaminals. The Journal of Physical Chemistry C,112(27), pp.9996-10003.

Xie, Y., Yan, B., Tian, C., Liu, Y., Liu, Q. and Zeng, H., 2014. Efficient removal of elemental mercury (Hg 0) by SBA-15-Ag adsorbents. Journal of Materials Chemistry A, 2(42), pp.17730-17734.

Yang, C.M., Sheu, H.S. and Chao, K.J., 2002. Templated Synthesis and Structural Study of Densely Packed Metal Nanostructures in MCM-41 and MCM-48. Advanced Functional Materials, 12(2), pp.143-148.

Yang, F., Jing, X., Huang, J., Sun, D. and Li, Q., 2015. Microwave-assisted biosynthesis of Ag/ZrO_2 catalyst with excellent activity toward selective oxidation of 1, 2-propanediol. Industrial & Engineering Chemistry Research, 54(20), pp.5373-5380.

Yin, A., Wen, C., Dai, W.L. and Fan, K., 2011. Ag/MCM-41 as a highly efficient mesostructured catalyst for the chemoselective synthesis of methyl glycolate and ethylene glycol. Applied Catalysis B: Environmental, 108, pp.90-99.

Zhang, H., Tang, C., Lv, Y., Sun, C., Gao, F., Dong, L. and Chen, Y., 2012. Synthesis, characterization, and catalytic performance of copper-containing SBA-15 in the phenol hydroxylation. Journal of colloid and interface science, 380(1), pp.16-24.

Zhang, X., Qu, Z., Li, X., Zhao, Q., Wang, Y. and Quan, X., 2011. Low temperature CO oxidation over Ag/SBA-15 nanocomposites prepared via in-situ "pH-adjusting" method. Catalysis Communications, 16(1), pp.11-14.

Zhao, D., Feng, J., Huo, Q., Melosh, N., Fredrickson, G.H., Chmelka, B.F. and Stucky, G.D., 1998. Triblock copolymer syntheses of mesoporous silica with periodic 50 to 300 angstrom pores. Science, 279(5350), pp.548-552.

Zhao, X.S., Lu, G.Q., Whittaker, A.K., Millar, G.J. and Zhu, H.Y., 1997. Comprehensive study of surface chemistry of MCM-41 using 29Si CP/MAS NMR, FTIR, pyridine-TPD, and TGA. The Journal of Physical Chemistry B, 101(33), pp.6525-6531.

Zhu, Y., Morisato, K., Li, W., Kanamori, K. and Nakanishi, K., 2013. Synthesis of silver nanoparticles confined in hierarchically porous monolithic silica: a new function in aromatic hydrocarbon separations. ACS applied materials & interfaces, 5(6), pp.2118-2125.

Zienkiewicz-Strzałka, M., Pasieczna-Patkowska, S., Kozak, M. and Pikus, S., 2013. Silver nanoparticles incorporated onto ordered mesoporous silica from Tollen's reagent. Applied Surface Science, 266, pp.337-343.

Chapter 4

Fine CuO anisotropic nanoparticles supported on mesoporous SBA-15 for selective hydrogenation of nitroaromatics

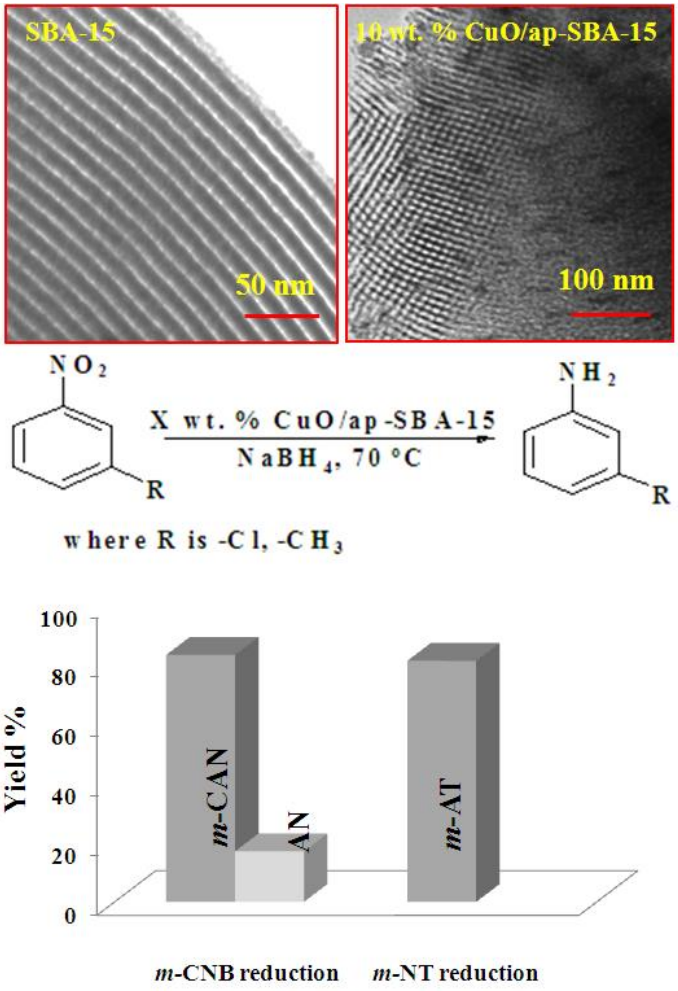

4.1 Introduction

In the last decade, a great deal of research has been dedicated to the incorporation of various precious metals like Pt (Rioux et al., 2005), Ag (Zhang et al., 2011), Au and Pd (El-Sheikh et al., 2013) on SBA-15 by different chemical approaches and their use as catalyst for catalyzing various oxidation-reduction reactions. Though these catalysts exhibit excellent catalytic activity, but their high cost limits their applicability on a large scale, stimulating studies on non-precious metals. Compared with noble metals, Cu and CuO are being economically viable and easily available, offers a promising material owing to its wide applications in the field of optics, electronics, and catalysis (Chan et al. 2007; Magdassi et al. 2010). Cu and CuO NPs has been used as a catalyst in many organic reactions like low temperature CO oxidation (Tu et al., 2006), oxidation of alcohols (Kalbasi et al., 2012), click synthesis (Kappe et al., 2010) and cross coupling reactions (Dulle et al., 2013). Moreover, Cu/CuO modified molecular sieves have also shown to be a good catalyst for different reactions. Recent reports based on the synthesis of Cu/SBA-15 and CuO/SBA-15 nanocomposites by different chemical approaches for catalyzing different oxidation-reduction reactions have been discussed in the literature (section 1.2.5, chapter 1). It is observed that the major difficulties involved with the methods reported in the literature have been the uncontrolled growth of metal NPs (Yang et al., 2008) resulting in their agglomeration and the low amount of loading (Tu et al., 2006) that leads to decrease in their catalytic efficiency. So, synthesis of well dispersed supported CuO/SBA-15 nanocomposites with high catalytic efficiency even at higher metal loading, by a simple, sustainable process involving green chemistry credentials is still a challenge. Moreover, on comparing the surface structural, morphological and catalytic properties of Au, Ag and Cu loaded SBA-15 nanocomposites (section 3.3.6, chapter 3) it was found that CuO loaded SBA-15 catalysts exhibited enhanced catalytic properties for reduction of nitroaromatics. Thus, keeping in view the cost effectiveness, rich abundance and environment friendly properties of CuO, SBA-15 supported CuO nanocomposites of varying wt. % of Cu loading were prepared for catalyzing the reduction of *m*-chloronitrobenzene (CNB) and *m*-nitrotoluene (NT) respectively.

4.2 Experimental Section

4.2.1 Synthesis and characterization of CuO/ap-SBA-15 nanocomposites

The preparation and characterization techniques used for the synthesis of CuO/ap-SBA-15 nanocomposites have been described in section 1.3.2-1.3.4 and 1.3.6 (Chapter 1).

4.2.2 Catalytic activity

The catalytic activity of the CuO/ap-SBA-15 nanocomposites has been evaluated for the reduction of (3 mM each)) *m*-chloronitrobenzene (*m*-CNB) and *m*-nitrotoluene (*m*-NT) as per procedure given in section (section 1.3.7, chapter 1). Reaction samples were analyzed by HPLC (section 1.3.6.11, chapter 1).

4.3 Results and discussion

4.3.1 Surface structural studies

Low angle XRD patterns for different wt. % Cu loading (Fig. 4.1a) exhibited similar XRD spectra, as that of SBA-15 with well resolved diffraction peaks at 1.0, 1.6 and 1.9^{o} corresponding to 100, 110 and 200 planes of the well-ordered hexagonal structure (Zhao et al., 1998) of *p6mm*

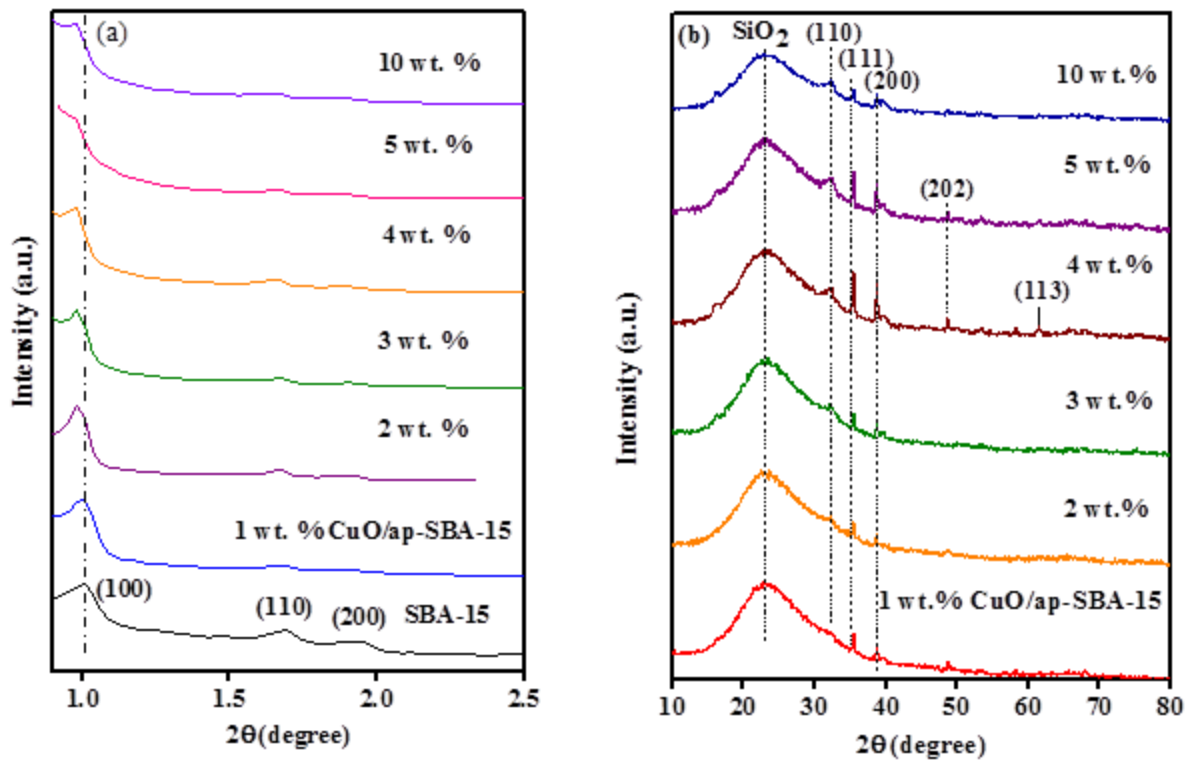

Fig. 4.1 (a) Low angle and **(b)** wide angle XRD patterns of bare SBA-15 and various wt. % CuO/ap-SBA-15 catalysts.

symmetry. It indicated no significant change in long range mesopore ordering and textural uniformity of SBA-15 even after metal impregnation. However, a decrease in the intensity of 110 and 200 peaks was observed with the loading of Cu on the surface of amino functionalized SBA-15 due to pore filling effect leading to decrease in electron density contrast upon introduction of CuO nanospecies within the mesochannels of the silica host. Ungureanu et al. (2013) also reported the decrease in the intensity of peaks due to the partial filling of SBA-15 mesopores with NiO for impregnated NiO-CuO/SBA-15 materials. Further, as Cu loading was increased from 1-10 wt. %, the peak corresponding to (100) plane shifted to lower 2θ value (from 1.00 to 0.97) illustrating an increase in structural parameters viz., lattice spacings (d_{100}) and unit cell parameters (a_o) (Table 4.1). The shifting of the (100) peak can be attributed to the slight disordering of the pore channels due to the development of the strain arising from the confinement of the CuO NPs within the mesopores. This further indicated the existence of CuO NPs within the mesoporous host. Similar findings have been reported elsewhere (Ajitha et al., 2010; Lihitkar et al., 2012). Moreover, an increase in various structural parameters due to the shifting of peaks to lower angle was also observed for various wt. % Ag/ap-SBA-15 nanocomposites (as discussed in chapter 3). However, when the Cu loading was increased to 5 wt. % and 10 wt. %, the peaks begin to fade away, implying a slight disruption of mesoporous structure at higher metal loading.

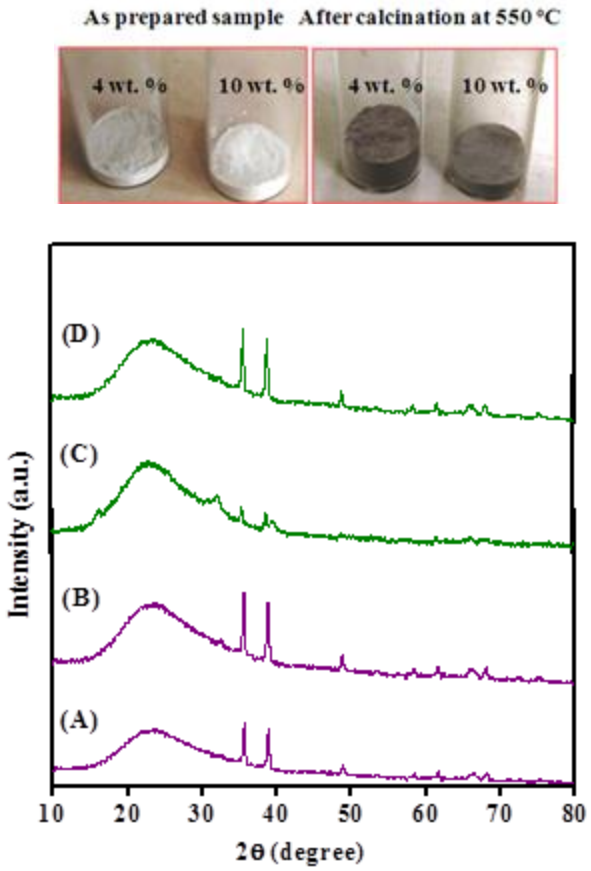

Fig. 4.2 Powder XRD patterns of 4 wt. % CuO/ap-SBA-15 (A) as prepared sample, (B) after calcination at 550 ^{o}C and 10 wt. % CuO/ap-SBA-15 (C) as prepared sample, (D) after calcination at 550 ^{o}C respectively.

Wide angle XRD patterns (Fig. 4.1b) of varying wt. % CuO/ap-SBA-15 nanocomposites exhibited a broad SiO_2 band at 22^{o} (Zhang et al., 2000) and diffraction peaks at

2θ = 32, 35.4, 38.3, 48.4 and 61.3^{o} corresponding to the monoclinic phase of CuO NPs (JCPDS card no. 48-1548). The intensity of the peaks was found to be directly dependent upon the metal loaded on mesoporous silica. The presence of very small and broad diffraction peaks in positions corresponding to CuO NPs was indicative of small crystallite size probably resulting from the confined growth of CuO within the mesoporous channels. Gu et al. (2008) and Van der Meer et al. (2009) also reported broader diffraction peaks for crystallites formed within the mesochannels of SBA-15. However, the spectra depicted an increase in intensity and narrowing/decrease in FWHM (full width at half maxima) of the peaks with an increase in Cu loading from 1 to 4 wt. %, illustrating an increase in the size of CuO NPs dispersed within/on the surface of mesoporous silica. This is supported by an increase in crystallite size i.e., 5.5 nm, 6.5 nm, 7.1nm and 8.3 nm for 1, 2, 3 and 4 wt. % Cu loading, respectively as calculated by the Scherrer equation for Cu (111) peak. Moreover, the (110) peak broadened in comparison to the (111) and (200) peaks in the diffraction pattern of 4 wt. % CuO/ap-SBA-15 signifying that with an increase in Cu loading, an effective amount of CuO nanospecies within the mesopores increase gradually leading to the development of the strain. As a result, crystal deformations w.r.t. specified planes also increased forming anisotropic nanoparticles (NPs) viz., nanospheres (NS) and nanorods (NR) within mesoporous sieves and has been further confirmed by TEM studies. Zienkiewicz-Strzałka et al. (2013) also reported that differences in the intensity and FWHM of the XRD peaks (wide angle) illustrate a change in the morphology of embedded Ag NPs within the SBA-15 for Ag/SBA-15 nanocomposites. Ma et al. (2014) also stated that increase in intensity and narrowing of peaks with increased Ag loading indicated a change in the morphology of Ag NPs for Ag/SBA-15 materials. However, further, increase in Cu loading to 5 and 10 wt. % did not have any negative effect on the dispersion, as it did not lead to a considerable increase in the size of CuO metal NPs, which was found to be 7.1 nm and 7.7 nm respectively. In fact, the mesoporous channels acted as a nanoreactor restricting the size, probably resulting in a change in morphology of CuO NPs. Moreover, beyond 4 wt. % Cu loading, the reflections become weak and diffuse implying poor crystallinity (Karakassides et al., 2000) due to partial disruption of the SBA-15 structure as a result of increased Cu loading. Moreover, the effect of an increase in calcination temperature upto 550 ^{o}C (Fig. 4.2) on the dispersion and size of 4 wt. % and 10 wt. % CuO/ap-SBA-15 nanocomposites were also studied.

It showed an increase in the intensities and sharpness of all the peaks, indicating the formation of large sized CuO NPs at a higher temperature within the mesoporous matrix.

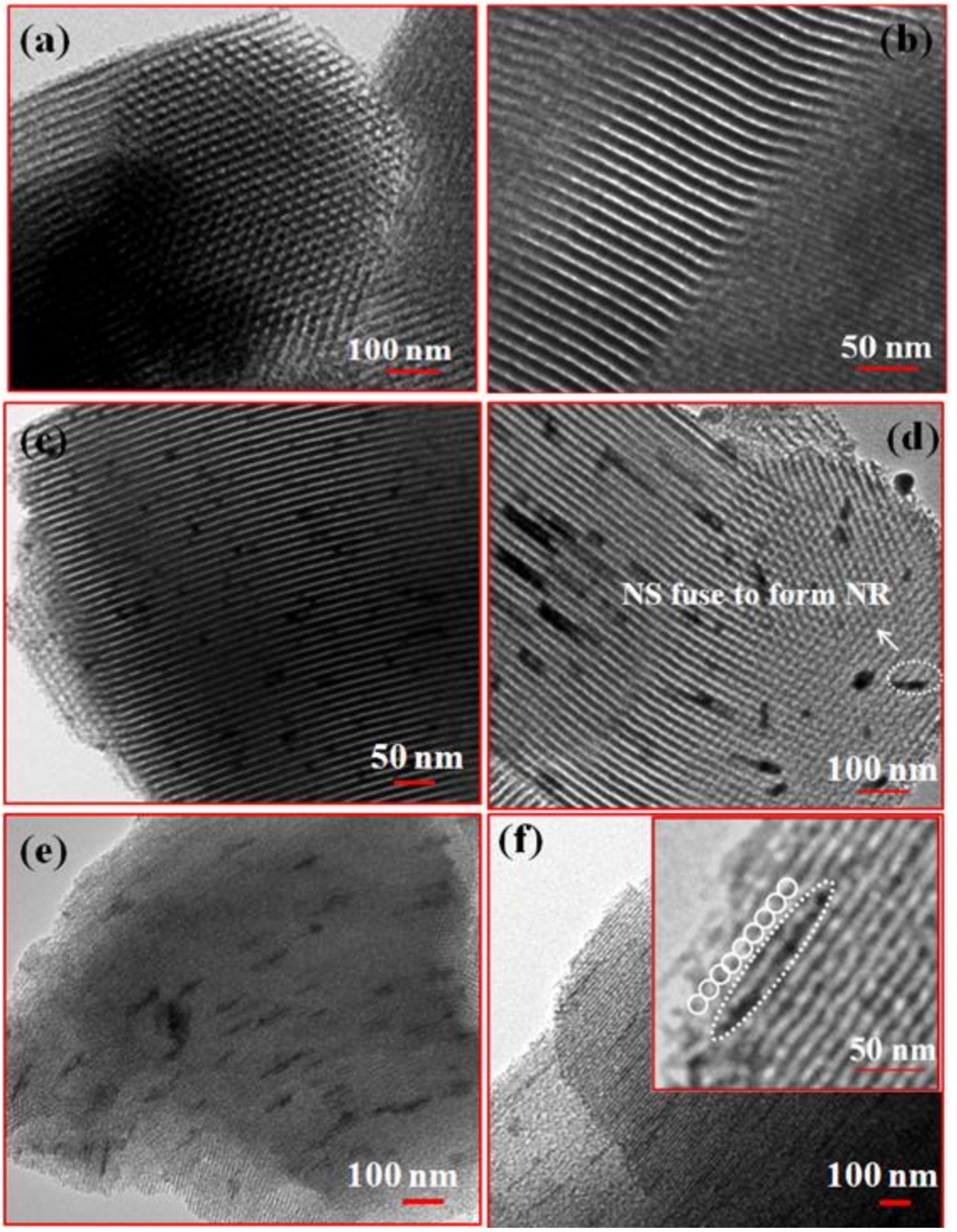

Fig. 4.3 TEM images of **(a)** SBA-15, **(b)** 1wt.% CuO/ap-SBA-15, **(c)** 2 wt.% CuO/ap-SBA-15, **(d)** 4 wt.% CuO/ap-SBA-15, **(e)** 5 wt.% CuO/ap-SBA-15 and **(f)** 10 wt.% CuO/ap-SBA-15 catalyst.

TEM micrographs (Fig. 4.3a) displayed regular hexagonal mesoporous SBA-15 structure with

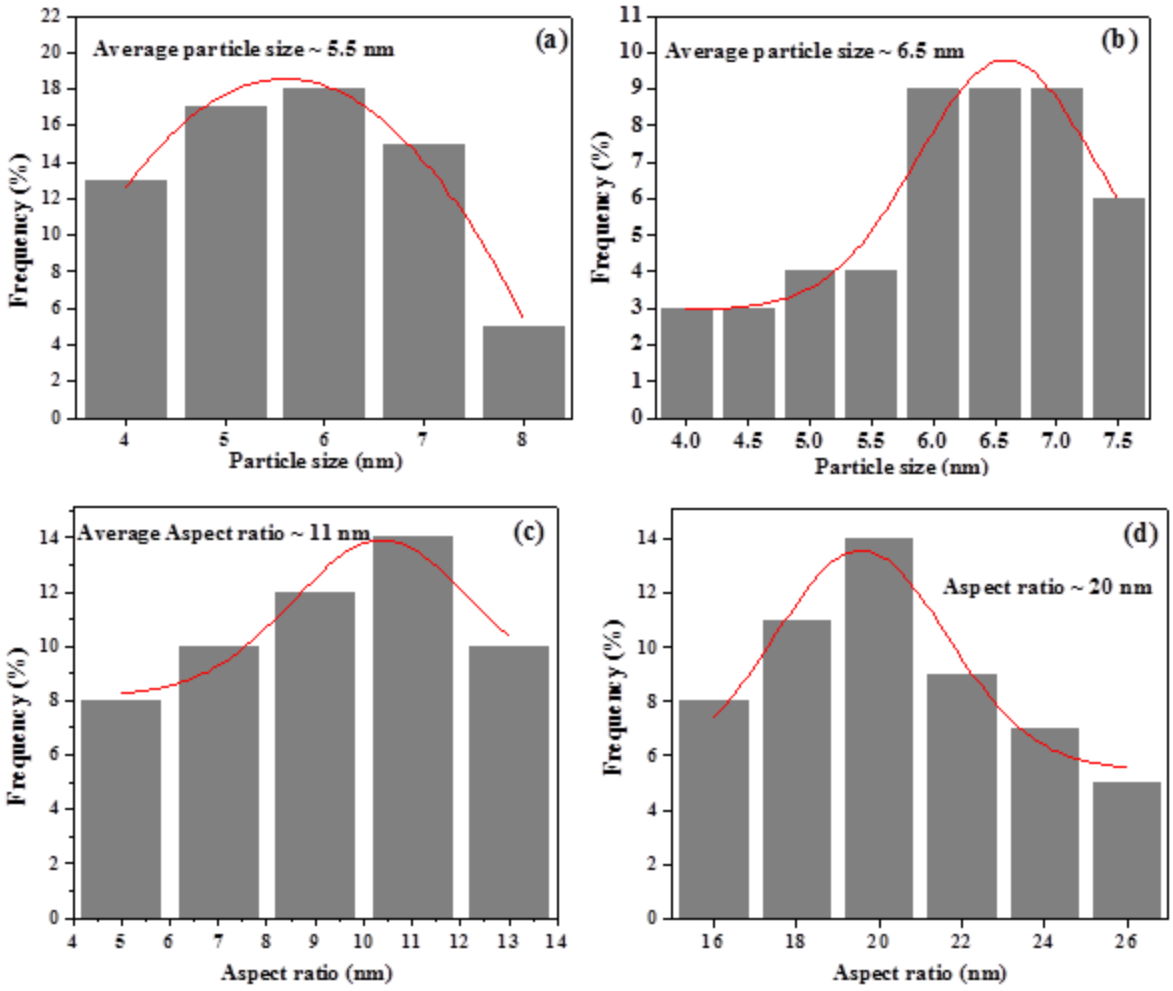

Fig. 4.4 Particle-size histograms of **(a)** 1 wt. %, **(b)** 2 wt. %, **(c)** 5 wt. % and **(d)** 10 wt. % CuO/ap-SBA-15 catalysts.

cylindrical channels exhibiting narrow pore size distribution. Although, no disruption of mesoporous channels was observed yet large differences in morphology of CuO NPs were observed as a function of increased Cu loading. Fine CuO NPs of average size ~5.5 nm, Figs. 4.3b and 4.4a) were depicted as black dots well dispersed against the light background of mesoporous support for 1 wt. % Cu loading. With increased metal loading to 2 wt. % (Figs. 4.3c and 4.4b), uniformly distributed CuO NS of average size ~6.5 nm were noticed within mesochannels. These results were in accordance with wide angle XRD studies. However, with an increase in Cu loading to 4 wt. %, instead of aggregation, anisotropic CuO NPs (Fig. 4.3d) were

observed as trapped within as well as on the surface of silica host. Both spherical and rod like

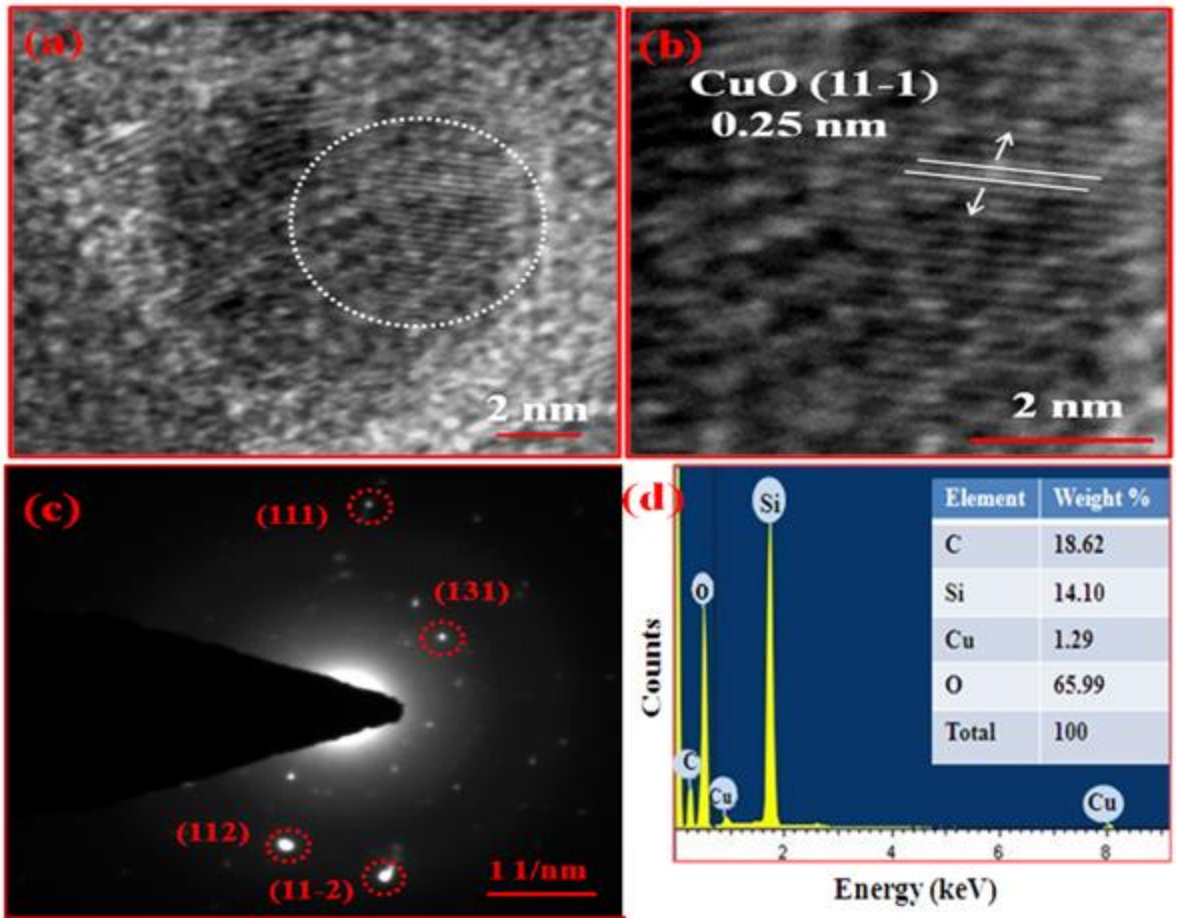

Fig. 4.5 (a) HR-TEM, **(b)** marked portion of fig. (a), **(c)** SAED pattern and **(d)** EDX spectra of 4 wt. % CuO/ap-SBA-15 catalyst.

CuO NPs were observed with diameter ~8 nm (in consistency with a pore diameter of SBA-15) and length ~ 80-150 nm. Due to strong metal-support interaction and restriction from channel walls, excessive CuO NPs (with increased Cu loading) were forced to align one after another, resulting in a change of morphology from spherical to rod shape (marked in Fig. 4.3d). Similar changes in particle morphology with increased metal loading have been reported elsewhere (Van der Meer et al., 2009; Taghavimoghaddam et al., 2012). Moreover, Chambers et al. (1998) also reported that due to strong metal-support interaction, Ni NPs supported on carbon nanofibres adopt different morphologies. For 5 wt. % Cu loading, small NR with average aspect ratio ~11 nm along with nanobundles (Figs. 4.3e and 4.4c) formed by the growth of some NR in adjacent mesopores were also observed. However, larger CuO NR (average aspect ratio ~20 nm,

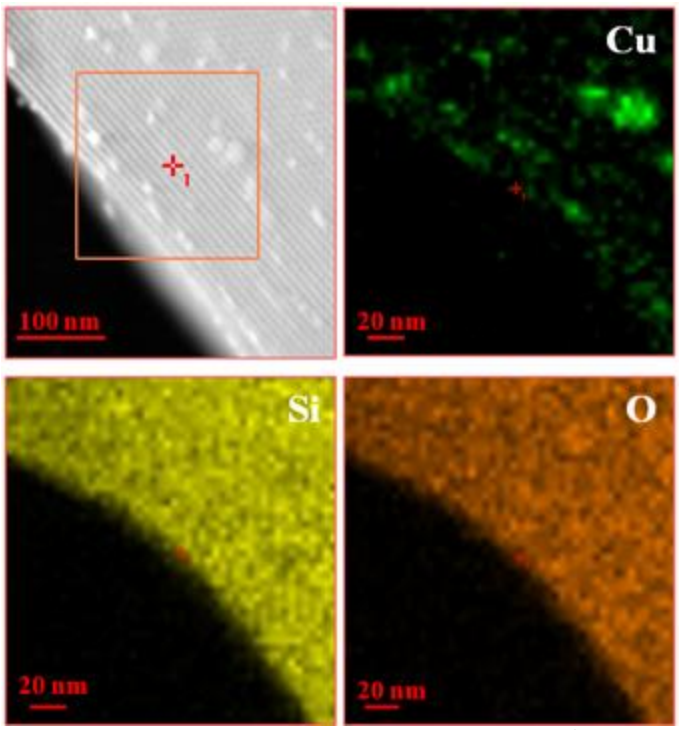

Fig. 4.6 STEM image and elemental mapping of 4 wt. % CuO/ap-SBA-15 catalyst.

Fig. 4.4d) were seen homogeneously dispersed and extending throughout the entire mesochannels for 10 wt. % Cu loading (Fig. 4.3f) due to the perfect alignment of CuO NPs forming rod like morphology. Furthermore, the lattice distance (0.25 nm) measured from HR-TEM (Figs. 4.5a,b) was found to be in agreement with (11-1) plane of crystalline CuO (JCPDS card no. 48-1548). Moreover, the selective area electron diffraction (SAED) pattern (Fig. 4.5c) confirmed (111), (131) and (11-2) planes corresponding to the presence of CuO nanospecies. EDX spectra (Fig. 4.5d) of the 4 wt. % CuO/ap-SBA-15 further established the presence of well dispersed and crystalline CuO within mesoporous support with 1.29 wt. % Cu loading. Elemental mapping studies (Fig. 4.6) also confirmed the uniform distribution of CuO NPs on the mesoporous host.

XPS spectrum of 10 wt. % CuO/ap-SBA-15 (Fig. 4.7) depicted a Cu $2p_{3/2}$ peak at a binding energy of 934 eV with a satellite at 943.3 eV which is the characteristic of Cu^{2+} species. Similar results have been reported by Zhang et al. (2012) for Cu/SBA-15 nanocomposites. The value of Cu $2p_{3/2}$ peak was little higher than the reported value of bulk CuO (Kong et al., 2009), attributed to the uniform dispersion of CuO nanospecies within MMs.

4.3.2 Optical studies

The solid state UV-Visible absorption spectra (Fig. 4.8) of different wt. % Cu impregnated SBA-15 catalysts depicted a sharp band at 359 nm due to the charge transfer between mononuclear Cu^{2+} and oxygen in $(Cu–O–Cu)_n$ surface species, indicating the presence of some Cu oligomers or CuO clusters in the extra framework position. Similar results have been

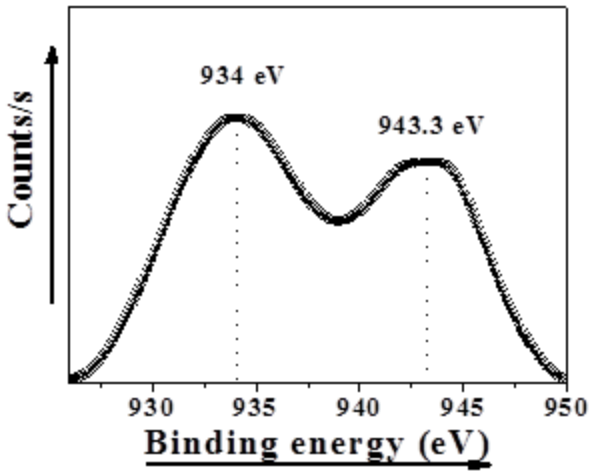

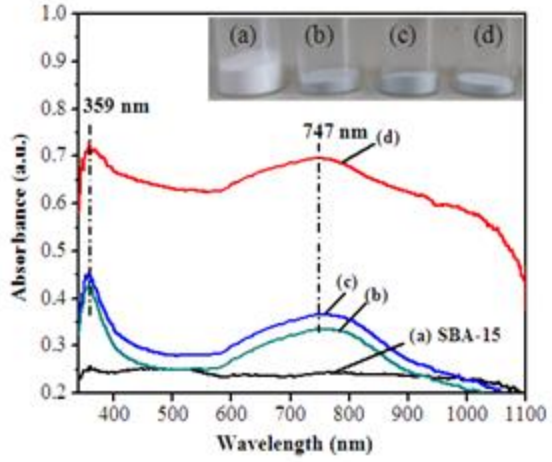

Fig. 4.7 XPS spectra of 10 wt. % CuO/ap-SBA-15 and **Fig. 4.8** Solid state UV-Visible absorption spectra of **(a)** bare SBA-15, **(b)** 1 wt.% CuO/ap-SBA-15, **(c)** 4 wt.% CuO/ap-SBA-15 and **(d)** 10 wt. % CuO/ap-SBA-15 catalyst.

reported by Chen et al. (2013) and Zhang et al. (2009) for impregnated Cu/SBA-15 and Cu/MCM-41 samples respectively. However, a broad band at 747 nm can be attributed to the d-d transition of Cu^{2+} in a pseudo-octahedral ligand oxygen environment, implying the presence of CuO NPs (Petre et al., 2013; Prasad et al., 2002), while no band was observed for bare SBA-15. An increase in the absorbance intensities further reflected an increase in Cu loading with a color change from white for bare SBA-15 to light green indicating the presence of Cu in the samples.

The FTIR spectra (Fig. 4.9) represented characteristic bands of SBA-15 (as discussed in section 2.3.1, chapter 2) with a broad absorption band at 3460 cm^{-1}, sharp bands at 1629 cm^{-1} and 973 cm^{-1} assigned to the stretching and bending vibrations of Si-OH bonds. In addition, characteristic bands of absorption at 1077, 790 and 463 cm^{-1} corresponding to asymmetric and symmetric stretching vibrations of Si-O-Si bonds of the host SBA-15 matrix (Martin-Aranda et al., 2010) were also observed in all the samples. The presence of a band at 2930 cm^{-1} attributed to NH_3^+ stretching confirmed the presence of aminopropyl groups (Wang et al., 2005) in ap-SBA-15. Similar spectra for ap-SBA-15 and Cu loaded samples indicated retention of structural integrity of SBA-15 even after surface functionalization and metal impregnation in accordance with the XRD and TEM studies. However, a slight decrease in the intensity of silanol groups is

due to the inclusion of Cu within the mesoporous sieves. Similar findings have been reported by Gao et al. (2008) for Vanadium loaded SBA-15 materials.

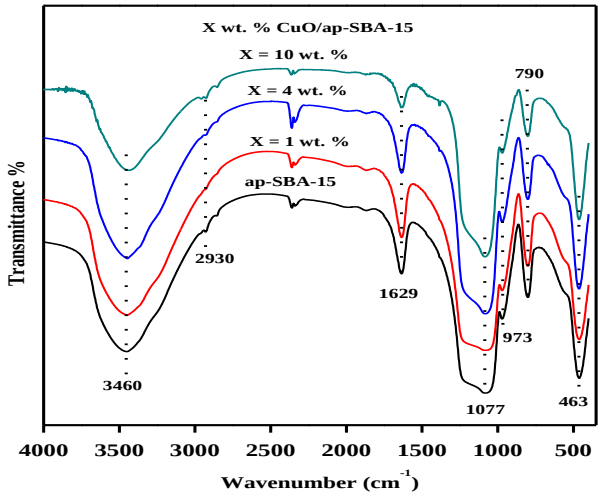

Fig. 4.9 FT-IR spectra of SBA-15 and various wt. % CuO/ap-SBA-15 catalysts

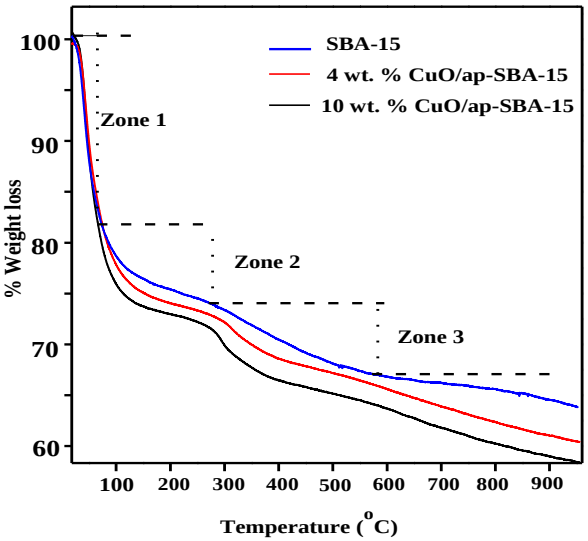

Fig. 4.10 TGA of SBA-15 and various wt. % CuO/ap-SBA-15 catalysts.

4.3.3 Thermal analysis

The TGA pattern of SBA-15 and various wt. % CuO/ap-SBA-15 catalysts (Fig. 4.10) showed degradation in three different wt. loss zones. The first wt. loss zone at ~100 ^{o} C (constituting ~17 % for SBA-15, 4 wt. % and 10 wt. % CuO/ap-SBA-15 respectively), is associated with the loss of physically adsorbed water molecules in silica channels and coordinated to Cu complexes (Zhang et al., 2012). The second wt. loss (~8 % for SBA-15, ~9 % for 4 wt. % and ~10 % for 10 wt. % CuO/ap-SBA-15) between 100-300 ^{o}C may be attributed to the decomposition of remaining surfactant (if any). The third wt. loss zone (~ 6 % for SBA-15, ~7 % for 4 wt. % and ~10 % for 10 wt. % CuO/ap-SBA-15) between 300-550 ^{o}C can probably be assigned to the decomposition of the aminopropyl groups. This is further supported by the wide angle XRD studies, where an increase in the size of CuO NPs was observed with increase in calcination temperature to 550 ^{o}C probably due to the decomposition of APTMS. However, a small wt. loss of ~ 3 % for SBA-15, ~7 % for 4 wt. % and ~9 % for 10 wt. % CuO/ap-SBA-15 above 570 ^{o}C is related to the combustion of remaining carbon species and dehydroxylation of Si-OH groups (Zhao et al., 1997).

4.3.4 Textural properties

Nitrogen adsorption-desorption isotherm of SBA-15 exhibited a typical type IV isotherm (Fig. 4.11) displaying HI hysteresis loop characteristic of MMs (Sing et al., 1985) having a narrow pore size distribution of cylindrical channels. Similar shape of the CuO/ap-SBA-15 isotherms as that of SBA-15 further revealed that mesostructural ordering of SBA-15 was maintained even after Cu loading (Taghavimoghaddam et al., 2012) as suggested by low angle XRD and TEM studies. In comparison to SBA-15, the capillary condensation step for various wt. % CuO/ap-SBA-15 slightly shifted towards lower relative pressure (from 0.65 to 0.6) signifying a decrease in pore diameter with Cu loading. Moreover, the BET profile for 1 wt. %

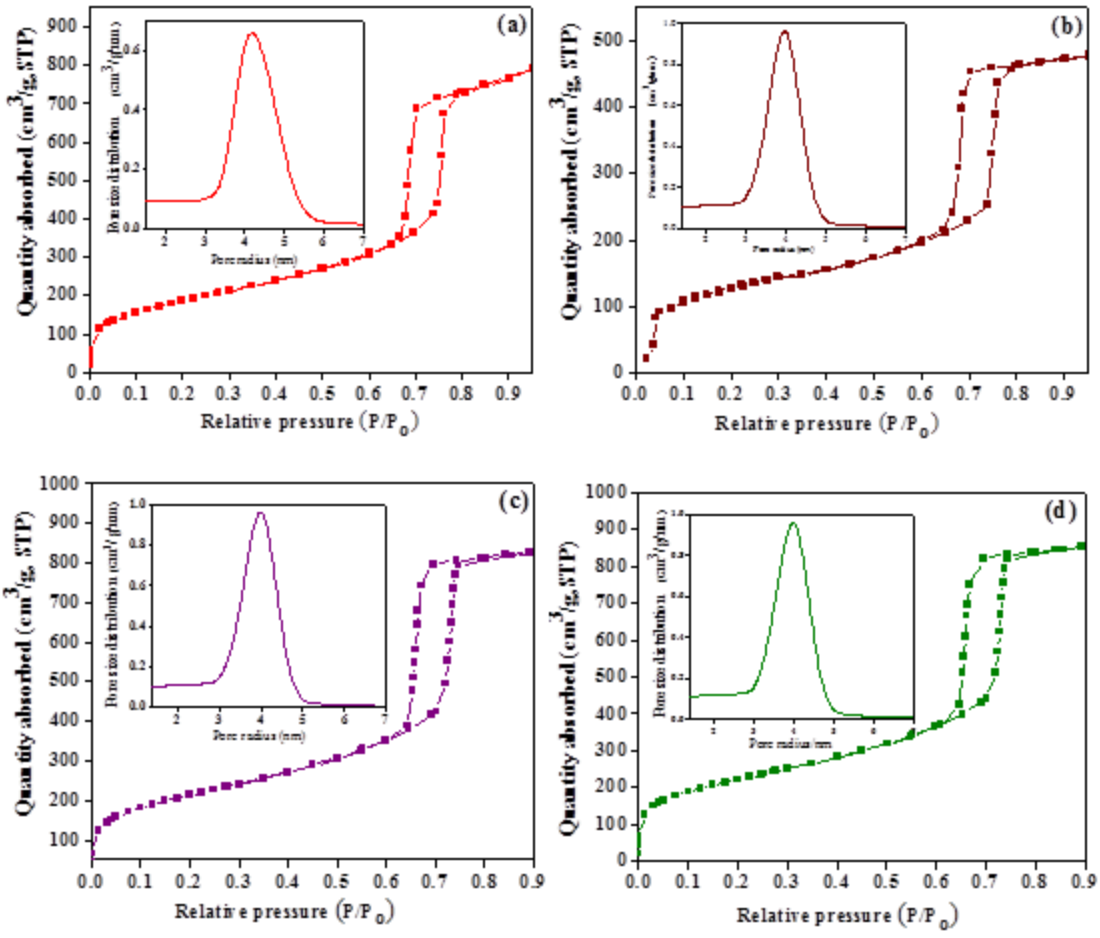

Fig. 4.11 Nitrogen adsorption-desorption isotherms and pore size distribution of **(a)** SBA-15, **(b)** 1 wt. % CuO/ap-SBA-15, **(c)** 4 wt. % CuO/ap-SBA-15 and **(d)**10 wt. % CuO/ap-SBA-15 catalyst.

CuO/ap-SBA-15 indicated a decrease in volume of adsorbed nitrogen implying a decrease in the surface area in comparison to bare SBA-15. This decrease in surface area can be attributed to the pore filling effect (Lin et al., 2008) by the formation of CuO NPs within the mesopores simultaneously followed by an increase in wall thickness (Table 4.1). Moreover, for higher Cu loadings of 4 and 10 wt. %, respectively, forced closure of the hysteresis loop on the desorption branch at p/p_o ~0.6 was noticed. This results from the cavitation phenomenon (Van der Voort et al., 2002) that occurs due to the partial blockage of SBA-15 pore openings with the increased amount of Cu impregnation and has been further supported by the increase in the surface area (more than that of SBA-15) for both 4 and 10 wt. % Cu loaded materials possibly due to the deposition of an excess of CuO NPs (as shown in TEM studies) to the outer silica surface due to the partial blockage of SBA-15 mesopores. Patel et al. (2011) also found that at higher Cu loading (10 wt. %) deposition of an excess of CuO NPs on the external surface resulted in an increase in the surface area for CuO/SBA-15 nanocomposites.

Table 4.1 Physico-chemical parameters of SBA-15 and various wt. % CuO/ap-SBA-15 catalysts.

Sample	**d-spacing, d_{100} (nm)**	**Unit cell parameter, a_o (nm)[a]**	**Wall thickness, d_w (nm)[b]**	**Surface area (m^2/g)**	**Pore volume (cm^3/g)**	**Pore size (nm)**
SBA-15	8.79	10.14	1.35	694	1.37	8.06
1 wt. % CuO/ap-SBA-15	8.99	10.38	1.39	512	0.93	7.48
2 wt. % CuO/ap-SBA-15	8.97	10.35	1.38	---	---	---
3 wt. % CuO/ap-SBA-15	9.06	10.46	1.4	---	---	---
4 wt. % CuO/ap-SBA-15	9.09	10.49	1.4	725	0.71	7.36
5 wt. % CuO/ap SBA-15	8.80	10.16	1.36	---	---	---
10 wt. % CuO/ap-SBA-15	9.04	10.43	1.39	762	1.37	7.22

$a_0 = 2/3^{1/2} d_{100}$, [b] $d_w = a_0 - d_{100}$

4.3.5 Catalytic activity

The catalytic activity of prepared CuO/ap-SBA-15 nanocomposites was evaluated for the reduction of *m*-substituted nitroaromatics such as CNB (Scheme 4.1) and NT (Scheme 4.2) to their respective amines. It was observed that in the absence of CuO/ap-SBA-15 catalysts, reduction of nitroaromatics with $NaBH_4$ and with bare SBA-15 did not take place, implying that metal oxide NPs were the real active sites. Moreover, the reaction was initiated by the addition of CuO/ap-SBA-15 catalyst suggesting adsorption of an electron donor (BH_4^-) and electron

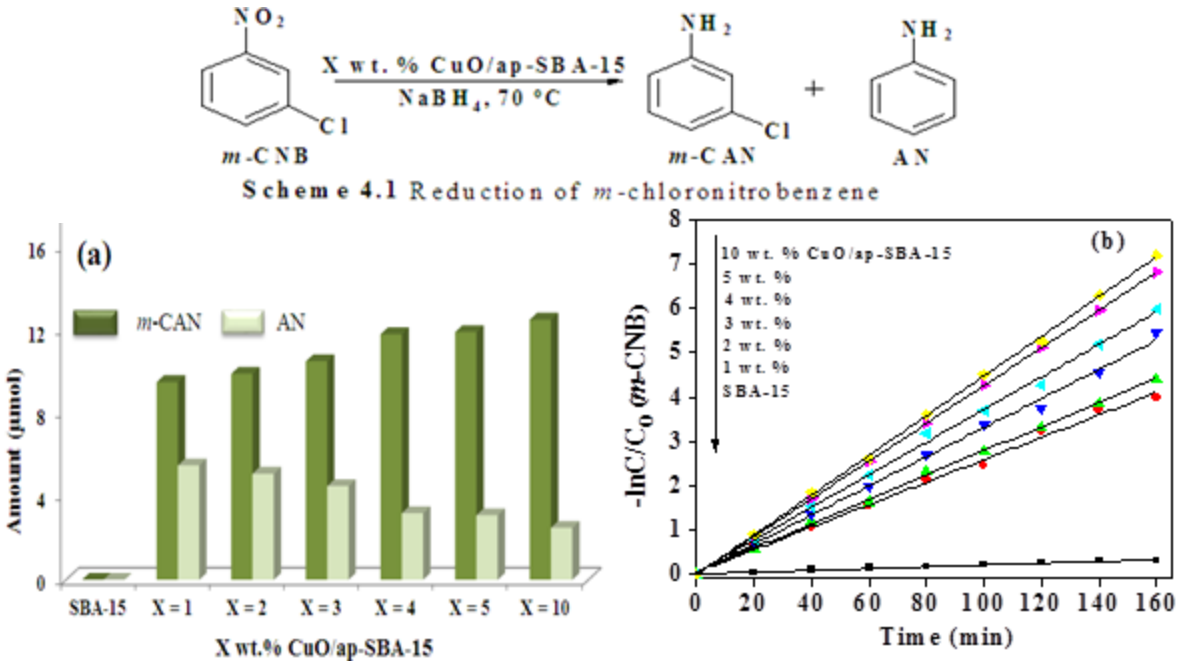

Fig. 4.12 (a) Product distribution of reduction of *m*-chloronitrobenzene (*m*-CNB) and **(b)** Time course graph of concentration of *m*-CNB (-ln C/C_o) for SBA-15 and various wt.% CuO/ap-SBA-15 catalysts.

acceptor (substrate) species on the surface of the CuO loaded SBA-15. It seems that the catalyst merely provides the adsorption sites and is not involved in the electron transfer process. Instead, the transfer of electrons takes place from BH_4^- to the nitroaromatics through the CuO nanospecies. Similar results have also been reported for CuO/γ-Al_2O_3 (Nandanwar et al., 2012). Moreover, reduction of *m*-CNB gave *m*-CAN as the major product accompanied by side reaction such as dechlorination leading to the formation of aniline whereas *m*-NT resulted in the formation of *m*-AT respectively (as confirmed by HPLC analysis Figs. 4.13 and 4.15a,b and c). Zhang et al. (1994) reported that the reactions catalyzed by supported metal (Pd) catalysts often exhibit moderate CAN selectivity with dechlorination to aniline. Linear plots of ln (C_t/C_o) vs time were obtained for all catalysts indicating pseudo first order kinetics of the reaction (Figs. 4.12b and 4.14b). It was seen that the catalytic activity increased with the increase in Cu loading from 1- 10 wt. %, leading to increase in the selectivity of *m*-CAN from 66 % to 83 %. This can be attributed to the fact that at lower Cu loading, Cu exists in the form of very fine CuO NPs (~5-6 nm) homogeneously dispersed and deep-seated (due to the lower surface area i.e., 512 m^2g^{-1} for 1 wt. % CuO/ap-SBA-15) within the mesochannels of the host, resulting in lesser accessibility of

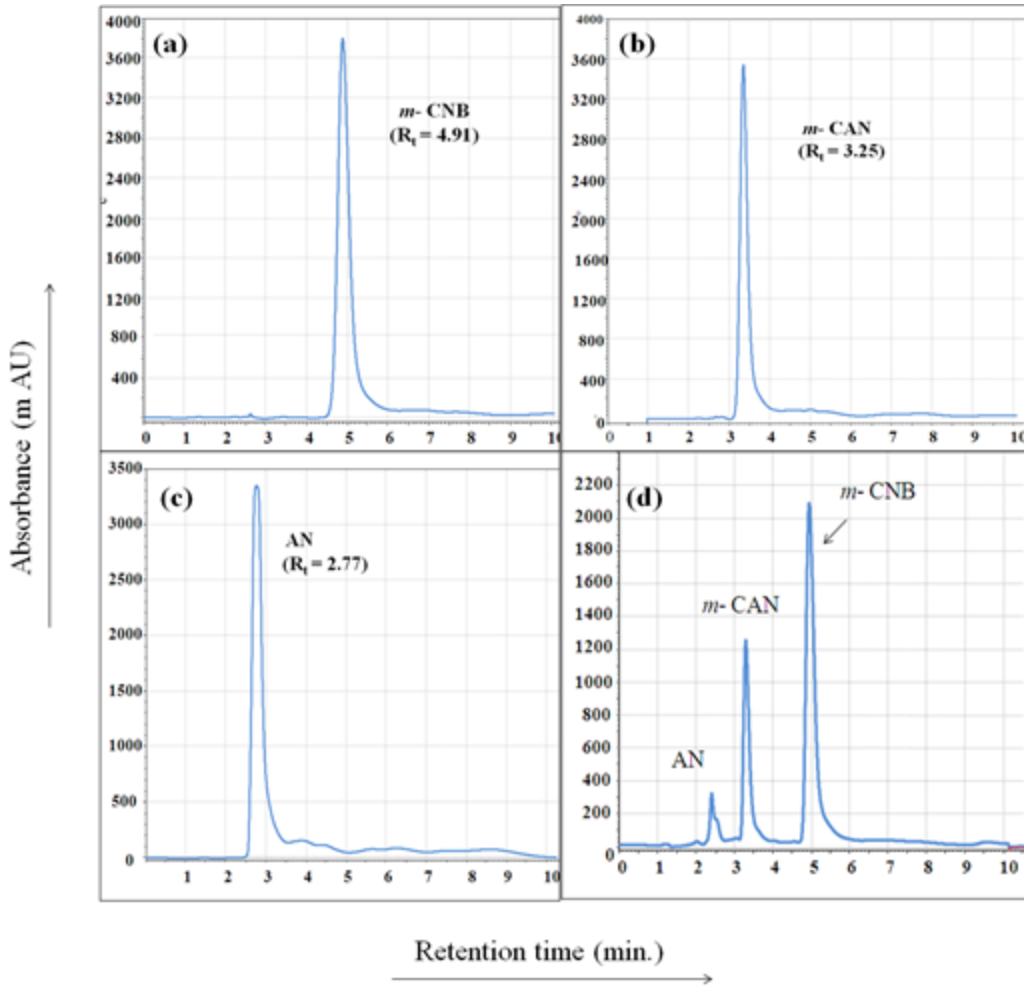

Fig. 4.13 HPLC chromatograms of 3 mM authentic samples of **(a)** *m*-CNB, **(b)** *m*-CAN, **(c)** AN and **(d)** reaction mixture at 70 min. interval.

active sites towards the reactant molecules. But at higher Cu loading of 4-10 wt. %, effective amount of CuO NPs within the mesopores also gradually increased (confirmed by MP-AES analysis, 3.1 wt. % and 8.7 wt. % for 4 and 10 wt. % CuO/ap-SBA-15 respectively) resulting in the development of the strain leading to slight disruption of the mesoporous channels. Thus, NPs come to lie both within as well as on the surface of the mesoporous host favoring improved access of CuO active sites towards the reactant that probably resulted in higher catalytic activity. This is further supported by the BET studies where 10 wt. % CuO/ap-SBA-15 exhibited highest surface area (762 $m^2 g^{-1}$) due to the presence of CuO NPs within as well as on the outer surface facilitating better adsorption of reactant molecules on the active catalytic sites. Thus, the catalytic activity is found to be strongly influenced by the amount of Cu loading, distribution of

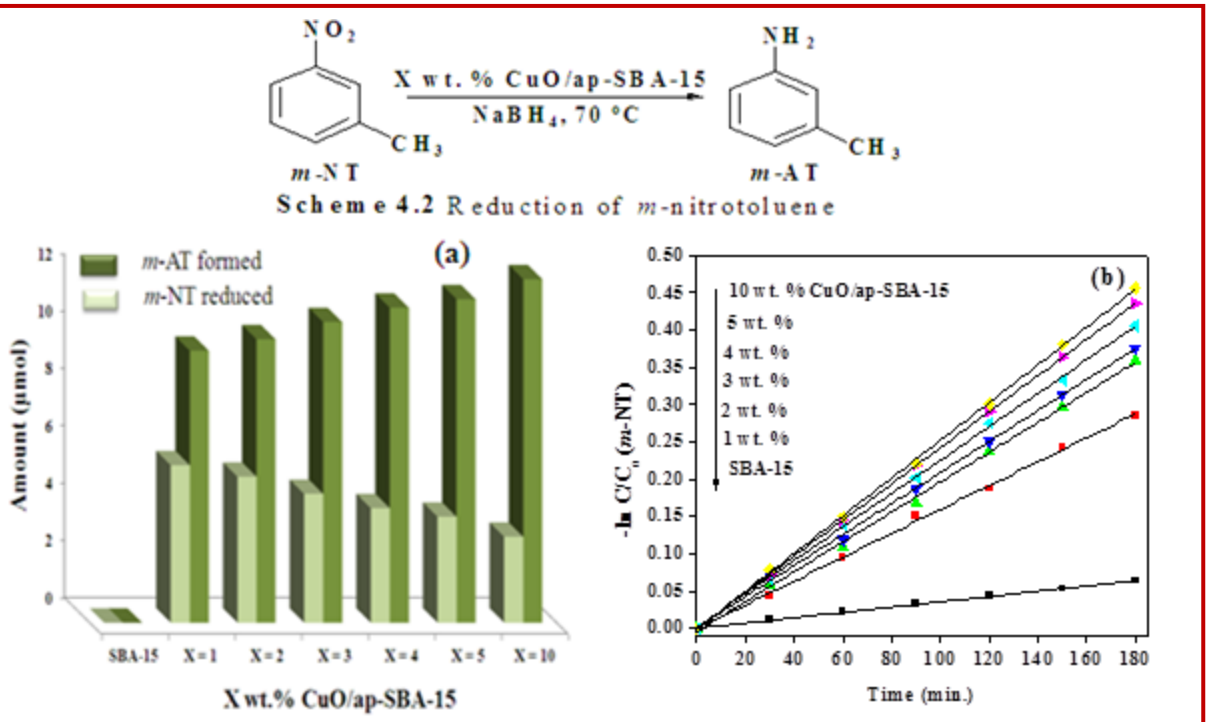

Fig. 4.14 **(a)** Product distribution of reduction of *m*-nitrotoluene by various wt. % CuO/ap-SBA-15 catalysts and **(b)** Time course graph of concentration of *m*-NT (-ln C/C_o) for SBA-15 and various wt.% CuO/ap-SBA-15 catalysts.

CuO NPs and surface area of the CuO/ap-SBA-15 nanocomposites. Similar findings have been reported by Kalbasi et al. (2014), for nitroaromatic reduction catalyzed by Ni incorporated polyamidoamine-polyvinylamine/SBA-15 nanocomposites. Jiang et al. (2009) also reported the presence of the active sites on the outer surface of the support to be the contributing factors to the high catalytic activity of supported Pt and Pd catalysts for the reduction of *o*-CNB. As a result, of all the prepared catalysts, 10 wt. % Cu loaded catalyst exhibited highest catalytic activity by 83 % and 100 % selectivity of *m*-chloroaniline (CAN) and *m*-aminotoluene (AT) for *m*-CNB and *m*-NT reduction respectively (Figs. 4.12a and 4.14a). The catalytic activity also showed a dependence on the nature of substituents present on the nitrobenzene (Van der Voort et al., 2002). The reaction rate increased with the increase in electron withdrawing effect of the substituents (-I effect) and varied as *m*-CNB (4.52×10^{-2}) > *m*-NT (1.47×10^{-3}) for 10 wt. % CuO/ap-SBA-15. For *m*-CNB, the presence of one $-NO_2$ group being electron withdrawing, lowered the electron density favoring fast conversion of nitro to the amino group resulting in higher selectivity for *m*-CAN. However, it was also observed that the presence of the electron

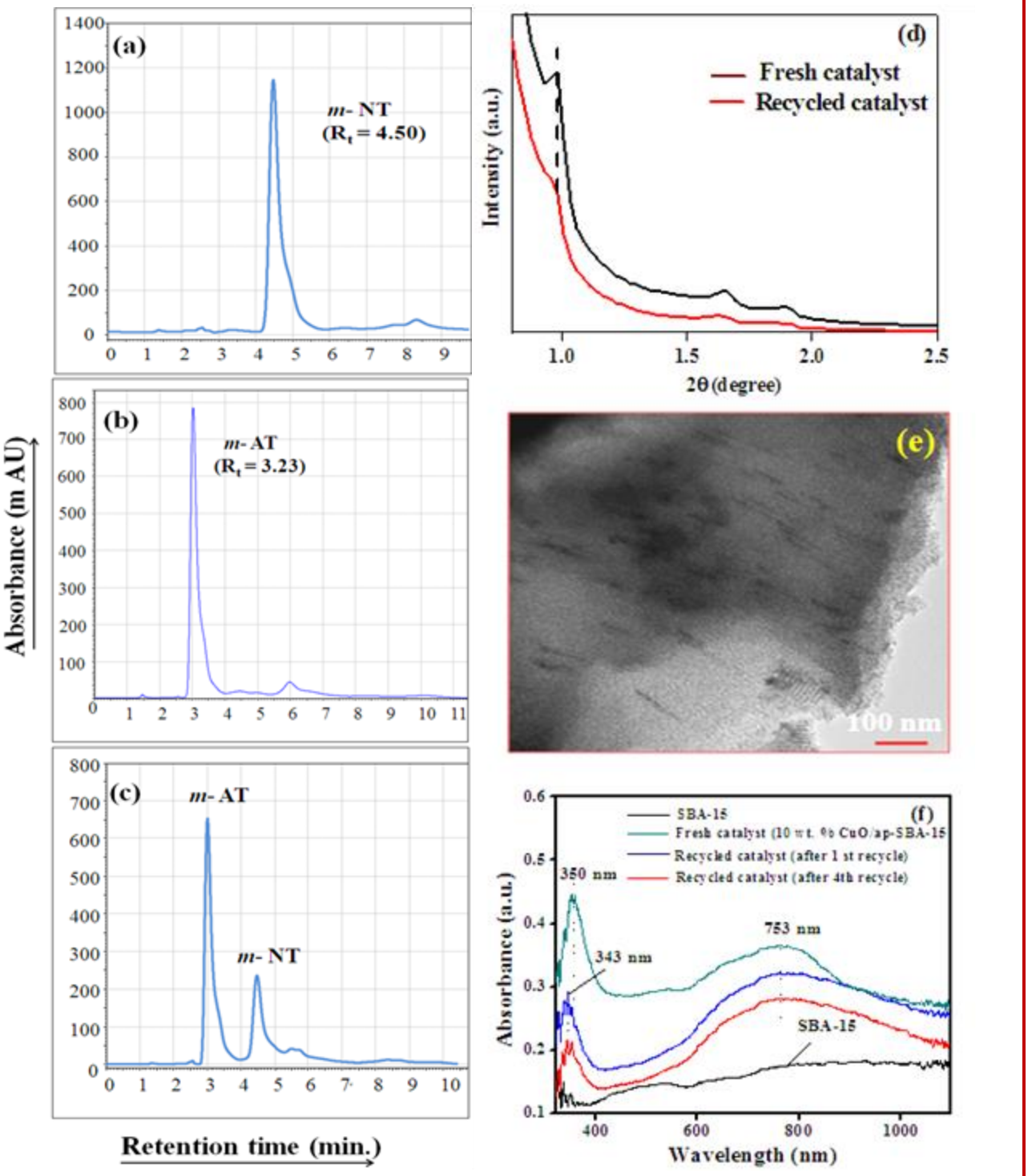

Fig. 4.15 HPLC chromatograms of 3 mM authentic samples of **(a)** *m*-NT, **(b)** *m*-AT and **(c)** reaction mixture at 180 min. interval and **(d)** Low angle XRD pattern, **(e)** TEM image of recycled 10 wt. % CuO/ap-SBA-15 catalyst after fourth successive run and **(f)** Solid state UV-Visible spectra of fresh and recycled 10 wt. % CuO/ap-SBA-15 catalyst.

eleasing group, i.e., -CH_3 group, increases the electron density on the nitrobenzene and reducethe rate of reduction. Moreover, although selectivity was 100 %, but yield obtained was ~ 81 % for *m*-NT reduction. In order to gain insight into the reusability and stability of the CuO/ap-SBA-15 catalyst under the reaction conditions, recycling experiments were carried out with 10 wt. % CuO/ap-SBA-15 catalyst for the reduction of *m*-NT. For recyclability, the catalyst was recovered from the reaction mixture by filtration, washed with ethanol, dried at the 60 ^{o}C for 8h and reused in the subsequent run. It was found that the catalyst can be reused for successive four recycles with a small decrease in the catalytic activity to 77 % for the reduction of *m*-NT. In addition, the low angle XRD pattern (Fig. 4.16) of the reused catalyst after the fourth run depicted a slight shifting (0.97 to 0.95) of the (100) peak towards the lower angle, implying a slight increase in the lattice parameters probably due to the hydrolysis of surface silica resulting in expansion of the pore-wall. TEM image (Fig. 16) of the recycled catalyst did not depict any aggregation of the CuO NPs relative to that of the fresh catalyst. The solid state UV-Visible absorption spectra of the recycled catalysts after 1st and 4 th recycle also represented bands at 343 nm and 753 nm respectively almost similar to that of the fresh catalyst (absorption bands at 350 nm and 753 nm). However, with a slight decrease in the intensity which may be due to the loss of small amounts of CuO during catalyst recovery (fig. 4.16). Moreover, the recycled catalysts retained same color (light green) as that of the fresh catalyst illustrating no change in the chemical composition of the catalyst. These results suggest the high stability and reusability of the catalyst.

It is thus demonstrated that metal loading had a significant effect on the size, morphology, dispersion ability and catalytic activity of the metal oxide NPs present within the mesoporous host. The high surface area of the 10 wt. % CuO/ap-SBA-15 also contributed to the efficient adsorption of nitro groups on the active sites of the CuO/ap-SBA-15 resulting in enhanced catalytic activity. The reaction rate showed dependence on the electron withdrawing ability of the substituents present on nitrobenzene and was found to be maximum for m-CNB. The easy preparation method, use of an economical catalyst, benign reaction conditions, the greater selectivity of products and high recyclability of the catalyst make this protocol be highly efficient and appealing for the reduction of nitroaromatics.

4.4 References

Ajitha, S. and Sugunan, S., 2010. Tuning mesoporous molecular sieve SBA-15 for the immobilization of α-amylase. Journal of Porous Materials, 17(3), pp.341-349.

Chambers, A., Nemes, T., Rodriguez, N.M. and Baker, R.T.K., 1998. Catalytic behavior of graphite nanofiber supported nickel particles. Comparison with other support media. The Journal of Physical Chemistry B, 102(12), pp.2251-2258.

Chan, G.H., Zhao, J., Hicks, E.M., Schatz, G.C. and Van Duyne, R.P., 2007. Plasmonic properties of copper nanoparticles fabricated by nanosphere lithography. Nano Letters, 7(7), pp.1947-1952.

Chen, C.S., Lai, Y.T., Lai, T.W., Wu, J.H., Chen, C.H., Lee, J.F. and Kao, H.M., 2013. Formation of Cu Nanoparticles in SBA-15 Functionalized with Carboxylic Acid Groups and Their Application in the Water–Gas Shift Reaction. ACS Catalysis, 3(4), pp.667-677.

Dulle, J., Thirunavukkarasu, K., Mittelmeijer-Hazeleger, M.C., Andreeva, D.V., Shiju, N.R. and Rothenberg, G., 2013. Efficient three-component coupling catalysed by mesoporous copper-aluminum based nanocomposites. Green Chemistry, 15(5), pp.1238-1243.

El-Sheikh, S.M., Ismail, A.A. and Al-Sharab, J.F., 2013. Catalytic reduction of p-nitrophenol over precious metals/highly ordered mesoporous silica. New Journal of Chemistry, 37(8), pp.2399-2407.

Gao, F., Zhang, Y., Wan, H., Kong, Y., Wu, X., Dong, L., Li, B. and Chen, Y., 2008. The states of vanadium species in V-SBA-15 synthesized under different pH values. Microporous and Mesoporous Materials, 110(2), pp.508-516.

Gu, J., Fan, W., Shimojima, A. and Okubo, T., 2008. Microwave-induced synthesis of highly dispersed gold nanoparticles within the pore channels of mesoporous silica. Journal of Solid State Chemistry, 181(4), pp.957-963.

Jiang, L., Gu, H., Xu, X. and Yan, X., 2009. Selective hydrogenation of o-chloronitrobenzene (o-CNB) over supported Pt and Pd catalysts obtained by laser vaporization deposition of bulk metals. Journal of Molecular Catalysis A: Chemical, 310(1), pp.144-149.

Kalbasi, R.J. and Zamani, F., 2014. Synthesis and characterization of Ni nanoparticles incorporated into hyperbranched polyamidoamine–polyvinylamine/SBA-15 catalyst for simple reduction of nitro aromatic compounds. RSC Advances, 4(15), pp.7444-7453.

Kalbasi, R.J., Nourbakhsh, A.A. and Zia, M., 2012. Aerobic Oxidation of Alcohols Catalyzed by Copper Nanoparticle-Polyacrylamide/SBA-15 as Novel Polymer-Inorganic Hybrid. Journal of Inorganic and Organometallic Polymers and Materials, 22(2), pp.536-542

Kappe, C.O. and Van der Eycken, E., 2010. Click chemistry under non-classical reaction conditions. Chemical Society Reviews, 39(4), pp.1280-1290.

Karakassides, M.A., Bourlinos, A., Petridis, D., Coche-Guerente, L. and Labbe, P., 2000. Synthesis and characterization of copper containing mesoporous silicas. J. Mater. Chem., 10(2), pp.403-408.

Kong, A., Wang, H., Yang, X., Hou, Y. and Shan, Y., 2009. A facile direct route to synthesize large-pore mesoporous silica incorporating high CuO loading with special catalytic property. Microporous and Mesoporous Materials, 118(1), pp.348-353.

Lihitkar, P.B., Violet, S., Shirolkar, M., Singh, J., Srivastava, O.N., Naik, R.H. and Kulkarni, S.K., 2012. Confinement of zinc oxide nanoparticles in ordered mesoporous silica MCM-41. Materials Chemistry and Physics, 133(2), pp.850-856.

Lin, D.H., Jiang, Y.X., Wang, Y. and Sun, S.G., 2008. Silver nanoparticles confined in SBA-15 mesoporous silica and the application as a sensor for detecting hydrogen peroxide. Journal of Nanomaterials, 2008, p.12.

Ma, L., Guo, X. and Xiang, L., 2014. Catalytic activity of Ag/SBA-15 for low-temperature gas phase selective oxidation of benzyl alcohol to benzaldehyde. Chinese Journal of Catalysis, 35(1), pp.108-119.

Magdassi, S., Grouchko, M. and Kamyshny, A., 2010. Copper nanoparticles for printed electronics: routes towards achieving oxidation stability. Materials, 3(9), pp.4626-4638.

Martin-Aranda, R.M. and Cejka, J., 2010. Recent advances in catalysis over mesoporous molecular sieves. Topics in Catalysis, 53(3-4), pp.141-153.

Nandanwar, S.U. and Chakraborty, M., 2012. Synthesis of colloidal CuO/γ-Al_2O_3 by microemulsion and its catalytic reduction of aromatic nitro compounds. Chinese Journal of Catalysis, 33(9), pp.1532-1541.

Patel, A., Rufford, T.E., Rudolph, V. and Zhu, Z., 2011. Selective catalytic reduction of NO by CO over CuO supported on SBA-15: Effect of CuO loading on the activity of catalysts. Catalysis today, 166(1), pp.188-193.

Petre, A.L., Carbajo, J.B., Rosal, R., Garcia-Calvo, E. and Perdigon-Melon, J.A., 2013. CuO/SBA-15 catalyst for the catalytic ozonation of mesoxalic and oxalic acids. Water matrix effects. Chemical Engineering Journal, 225, pp.164-173.

Prasad, M.R., Kamalakar, G., Kulkarni, S.J. and Raghavan, K.V., 2002. Synthesis of binaphthols over mesoporous molecular sieves. Journal of Molecular Catalysis A: Chemical, 180(1), pp.109-123.

Rioux, R.M., Song, H., Hoefelmeyer, J.D., Yang, P. and Somorjai, G.A., 2005. High-surface-area catalyst design: synthesis, characterization, and reaction studies of platinum nanoparticles in mesoporous SBA-15 silica. The Journal of Physical Chemistry B, 109(6), pp.2192-2202.

Sing, K.S., 1985. Reporting physisorption data for gas/solid systems with special reference to the determination of surface area and porosity (Recommendations 1984). Pure and applied chemistry, 57(4), pp.603-619.

Taghavimoghaddam, J., Knowles, G.P. and Chaffee, A.L., 2012. Preparation and characterization of mesoporous silica supported cobalt oxide as a catalyst for the oxidation of cyclohexanol. Journal of Molecular Catalysis A: Chemical, 358, pp.79-88.

Tu, C.H., Wang, A.Q., Zheng, M.Y., Wang, X.D. and Zhang, T., 2006. Factors influencing the catalytic activity of SBA-15-supported copper nanoparticles in CO oxidation. Applied Catalysis A: General, 297(1), pp.40-47.

Ungureanu, A., Dragoi, B., Chirieac, A., Ciotonea, C., Royer, S., Duprez, D., Mamede, A.S. and Dumitriu, E., 2013. Composition-dependent morphostructural properties of Ni–Cu oxide

nanoparticles confined within the channels of ordered mesoporous SBA-15 silica. ACS applied materials & interfaces, 5(8), pp.3010-3025.

Van der Meer, J., Bardez, I., Bart, F., Albouy, P.A., Wallez, G. and Davidson, A., 2009. Dispersion of Co_3O_4 nanoparticles within SBA-15 using alkane solvents. Microporous and Mesoporous Materials, 118(1), pp.183-188.

Van der Voort, P., Ravikovitch, P.I., De Jong, K.P., Neimark, A.V., Janssen, A.H., Benjelloun, M., Van Bavel, E., Cool, P., Weckhuysen, B.M. and Vansant, E.F., 2002. Plugged hexagonal templated silica: a unique micro-and mesoporous composite material with internal silica nanocapsules. Chemical Communications, (9), pp.1010-1011.

Wang, X., Lin, K.S., Chan, J.C. and Cheng, S., 2005. Direct synthesis and catalytic applications of ordered large pore aminopropyl-functionalized SBA-15 mesoporous materials. The Journal of Physical Chemistry B, 109(5), pp.1763-1769.

Yang, J.S., Jung, W.Y., Lee, G.D., Park, S.S., Jeong, E.D., Kim, H.G. and Hong, S.S., 2008. Catalytic combustion of benzene over metal oxides supported on SBA-15. Journal of Industrial and Engineering Chemistry,14(6), pp.779-784.

Zhang, G., Long, J., Wang, X., Zhang, Z., Dai, W., Liu, P., Li, Z., Wu, L. and Fu, X., 2009. Catalytic role of Cu sites of Cu/MCM-41 in phenol hydroxylation. Langmuir, 26(2), pp.1362-1371.

Zhang, H., Tang, C., Lv, Y., Sun, C., Gao, F., Dong, L. and Chen, Y., 2012. Synthesis, characterization, and catalytic performance of copper-containing SBA-15 in the phenol hydroxylation. Journal of colloid and interface science, 380(1), pp.16-24.

Zhang, W.H., Shi, J.L., Wang, L.Z. and Yan, D.S., 2000. Preparation and characterization of ZnO clusters inside mesoporous silica. Chemistry of materials, 12(5), pp.1408-1413.

Zhang, X., Qu, Z., Li, X., Zhao, Q., Zhang, X. and Quan, X., 2011. In-situ synthesis of Ag/SBA-15 nanocomposites by the "pH-adjusting" method. Materials Letters, 65(12), pp.1892-1895.

Zhang, Y., Liao, S. and Xu, Y., 1994. Highly active polymer anchored palladium catalyst for the hydrodehalogenation of organic halides under mild conditions. Tetrahedron letters, 35(26), pp.4599-4602.

Zhao, D., Huo, Q., Feng, J., Chmelka, B.F. and Stucky, G.D., 1998. Nonionic triblock and star diblock copolymer and oligomeric surfactant syntheses of highly ordered, hydrothermally stable, mesoporous silica structures. Journal of American Chemical Society, 120, pp.6024-6036.

Zhao, X.S., Lu, G.Q., Whittaker, A.K., Millar, G.J. and Zhu, H.Y., 1997. Comprehensive study of surface chemistry of MCM-41 using 29Si CP/MAS NMR, FTIR, pyridine-TPD, and TGA. The Journal of Physical Chemistry B, 101(33), pp.6525-6531.

Zienkiewicz-Strzałka, M., Pasieczna-Patkowska, S., Kozak, M. and Pikus, S., 2013. Silver nanoparticles incorporated onto ordered mesoporous silica from Tollen's reagent. Applied Surface Science, 266, pp.337-343.

Chapter 5

Uniform dispersion of a bimetallic/binary mixture of Au-Ag supported SBA-15 nanocomposites for selective reduction of nitroaromatics

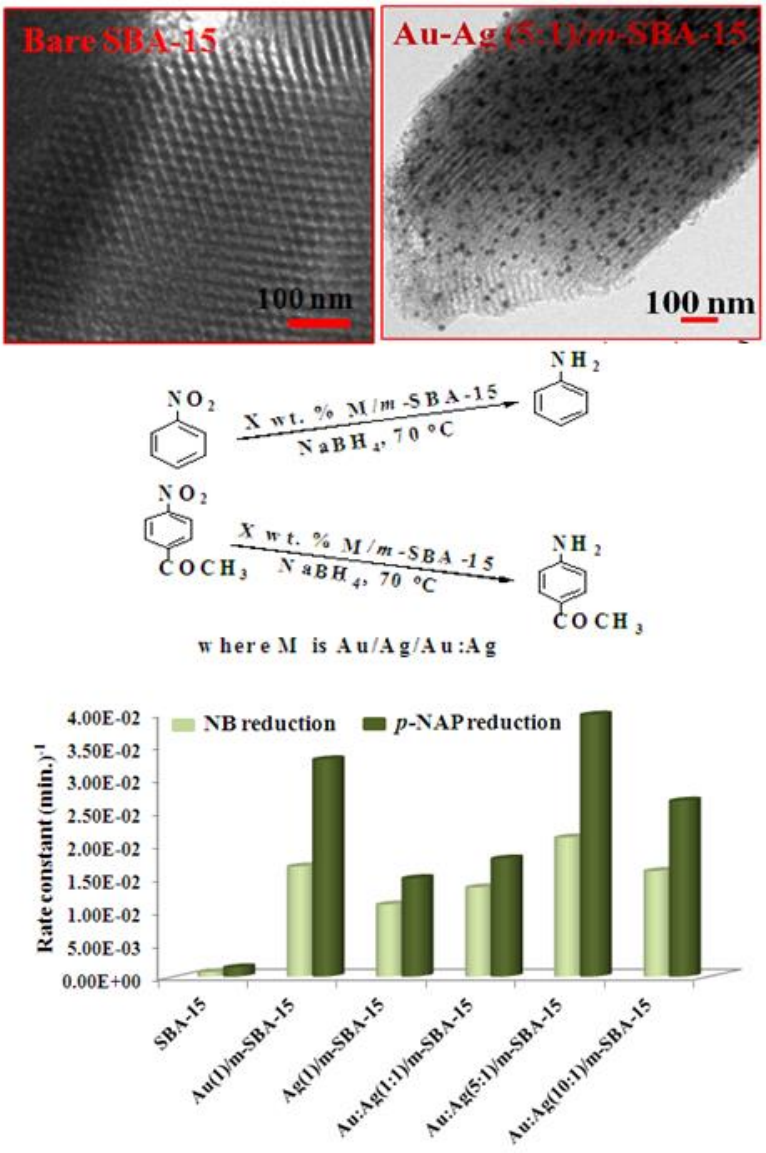

5.1 Introduction

Advancement in nanomaterial synthesis has been a major breakthrough in the field of nanoscience and nanotechnology, which has diversified its applications in electronics, material chemistry, sensors and even catalysis. Moreover, it is observed that the metals when reduced to nanometric range exhibit maximum reactivity and outstanding catalytic activity in comparison to their bulk state. The essentiality of controlled synthesis of metallic nanoparticles (NPs) has attracted the scientific community over the last two decades. It is necessary to stabilize the metal NPs by confining within some suitable porous support/matrix with a large surface area like SBA-15 (as discussed in previous chapters) as they may undergo agglomeration at elevated temperature (Ivashchenko et al., 2012). Furthermore, it is expected that metal/support synergy and the confinement effect within the mesopores play a crucial role in circumventing undesirable NP growth/sintering at high temperature (Bond et al., 1991) and serves to be apt for the controlled synthesis of metallic NPs resulting in high catalytic activity. In contrary to supported monometallic NPs, the formation of the supported bimetallic (BM) nanostructures (composed of two different metals) is found to be dependent on their composition, miscibility and reduction of the metal ions (Pal et al., 2007) and thus, variation in the composition of the BM NPs often results in tunable catalytic, electrical and optical properties. As a result, supported bimetallic (BM) nanostructures show improved physicochemical properties based on the synergistic effect of two metals (Liu et al., 2011). In recent years, reports on the synergistic catalysis of supported BM nanostructures have tremendously increased, however, accurate control over nucleation and growth of two metals due to their different thermodynamic and kinetic characteristics is still required for the controlled synthesis of BM NPs.

Reports have been published on the synergistic catalytic effects of various supported noble metal alloy NPs particularly Au containing bimetallic catalysts viz., Au-Cu, Au-Pt, Au-Pd, and Au-Ag etc. which have already been described in section 1.2.6 (chapter 1). Liu et al. (2011) reported the synthesis of Au-Cu alloy NPs on SBA-15 for catalyzing CO oxidation and found that the Au-Cu (BM) NPs showed superior catalytic activity in comparison to their monometallic (Au) counterparts illustrating the synergistic effect between Au and Cu. Among all the noble metals that form BM combinations with Au, due to similar lattice constants and face-centered cubic (FCC) structure, Ag exhibits higher affinity for Au atoms and can easily form homogeneous Au-Ag phase (Murugadoss et al., 2012). Thus, the geometric and electronic

properties of Au based catalysts can be easily enhanced with the introduction of Ag atoms leading to improved activity in comparison to monometallic Au or Ag based catalysts. In recent years, Au-Ag BM systems have been used for catalyzing CO oxidation (Qu et al., 2013), oxidation of alcohols (Nagy et al., 2014), alkene epoxidation (Kustov et al., 2013) and selective hydrogenation of esters (Zheng et al., 2013). However, there have been few reports of Au-Ag BM systems used as a catalyst for the reduction of nitroaromatics although reports (Torres et al., 2013) based on monometallic noble metal catalysts exhibiting high activity and selectivity for the reduction of nitroaromatics are available. The reduction of nitroaromatic compounds to their respective anilines is an important industrial reaction as anilines form intermediates in the preparation of dyes, pharmaceuticals, agrochemicals and polymers (Rahaim et al., 2005; Chandrasekhar et al., 2006; Shi et al., 2007). However, in Au-Ag BM catalytic system motivated by the role of Ag in demonstrating the strong ability for oxygen adsorption and activation capabilities for CO oxidation (Wang et al., 2005a, 2005b and 2006). It is expected that Au-Ag BM catalytic systems may also show better catalytic activity for the reduction of nitroaromatics. In reference to the above context, synthesis of BM Au-Ag loaded SBA-15 nanocomposites were carried out and their catalytic activity was evaluated for the reduction of nitrobenzene (NB) and *p*-nitro acetophenone (*p*-NAP) respectively. Moreover, changes in their physicochemical and catalytic parameters were also studied as a function of increased Au loading.

5.2 Experimental Section

5.2.1 Preparation and characterization of Au-Ag/m-SBA-15 nanocomposites

The synthesis procedure and characterization techniques used for the synthesis of BM Au-Ag/*m*-SBA-15 nanocomposites have already been described in section 1.3.2-1.3.5 and 1.3.6 (chapter 1).

5.2.2 Catalytic Activity

The catalytic activity of the BM Au-Ag/*m*-SBA-15 nanocomposites was evaluated for the reduction of 10µmol of nitrobenzene (NB) and *p*-nitro acetophenone (*p*-NAP) by the procedure given in section 1.3.7 (chapter 1). Reaction samples were analyzed by HPLC (section 1.3.6.11, chapter 1).

5.3 Results and discussion

5.3.1 Synthesis of Au-Ag/m-SBA-15 nanocomposites

The formation of Au-Ag/*m*-SBA-15 nanocomposites involved the addition of $HAuCl_4$ (aq.) solution followed by the addition of $AgNO_3$ (aq.) solution to the surface modified silica support. Surface modification was done with APTMS that acted as stabilizing agent and helped in creating anchoring sites for the uniform dispersal of Au NPs on the mesoporous support which may otherwise undergo aggregation. Similar reports of a strong interaction between amine and gold precursor have been published elsewhere (Chi et al., 2005; Chiang et al., 2005). With APTMS modification, the support surface gets positively charged with aminium ions and can strongly adsorb the negatively charged $AuCl_4^-$ ions due to the strong electrostatic interaction between the amino groups and the gold precursor. Then, $AgNO_3$ (aq.) solution was subsequently added when Ag^+ ions were adsorbed on the negatively charged Au surface due to electrostatic attraction and metallic bonding. However, the formation of AgCl cannot be avoided due to the galvanic replacement reaction between Ag and $AuCl_4^-$ ions that may result in aggregation of some particles upon thermal treatment. Qu et al. (2013) also stated that the increase in the particle size of (BM) Au-Ag nanocomposites is ascribed to the formation of AgCl during Ag deposition on Au loaded APTMS modified SBA-15 nanocomposites. In order to remove the AgCl so formed the suspension was filtered, washed thoroughly with ammonia solution, deionized water and dried at 60 ^oC. The prepared materials were finally calcined at high temperature under H_2 for the removal of organic moieties and for the formation of BM Au-Ag nanocomposites.

5.3.2 Chemical composition of the samples

A series of BM catalysts were prepared by varying Au loading from 1-5 and 10 wt. % w.r.t 1 wt. % Ag loading. Table 5.1 gives the actual wt. % of metal loading which is close to the used wt. % indicating the successful impregnation of Au and Ag metals on the mesoporous support.

5.3.3 Surface structural morphology

Low angle XRD pattern (Fig. 5.1a) of SBA-15 exhibited an intense diffraction peak at 0.8^o indexed to (100) plane, characteristic of ordered hexagonal structure with *p6mm* symmetry (Zhao et al., 1998). Similar XRD patterns were obtained for mono as well as various (BM) Au:Ag(x:y)/*m*-SBA-15 nanocomposites indicating that the mesoporous structure is maintained after metal loading (Wang et al., 2008). However, a decrease in the intensity of peaks relative to

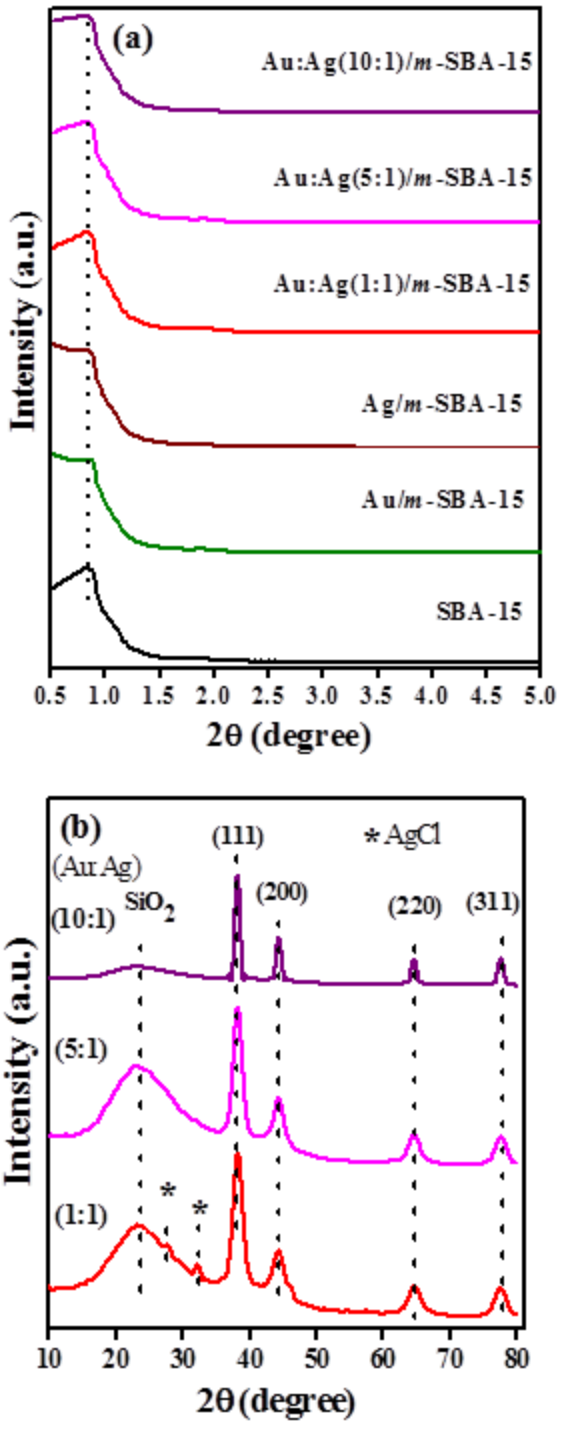

Fig. 5.1 Powder XRD pattern (a) Low angle of SBA-15, Au/ *m*-SBA-15, Ag/ *m*-SBA-15, bimetallic Au:Ag(x:y)/*m*-SBA-15 catalysts and **(b)** Wide angle of bimetallic Au:Ag(x:y)/*m*-SBA-15 catalysts.

SBA-15 was observed, attributed to the pore-filling effect (Han et al., 2012) due to the formation of metallic as well as BM NPs within the silica framework. Moreover, the array channels also get affected by the introduction of the metal within the mesoporous sieves. As a result, peak shifting leading to the decrease in lattice parameters (Table 5.1) took place signifying slight shrinkage of mesoporous sieves. Mureddu et al. (2014) stated that the shifting of the XRD peaks to higher angles with a decrease in lattice parameters is associated with the introduction of ZnO and FeO NPs within the SBA-15 channels for metal-oxide SBA-15 nanocomposites.

Wide angle XRD patterns (Fig. 5.1c) of monometallic Au(1)/*m*-SBA-15 displayed the characteristic broad SiO_2 band at 22^o and diffraction peaks of metallic Au (as discussed in section 2.3.2, chapter 2). In contrast Ag(1)/*m*-SBA-15 did not exhibit any diffraction peak probably due to the low Ag loading signifying the presence of highly dispersed Ag nano species within the mesoporous support (Zhang et al., 2012). On the other hand, for all (BM) Au-Ag/*m*-SBA-15 nanocomposites (Fig. 5.1b) with different (Au:Ag) ratios, similar XRD diffraction patterns as that of the monometallic Au or Ag were observed. Due to similar face-centered

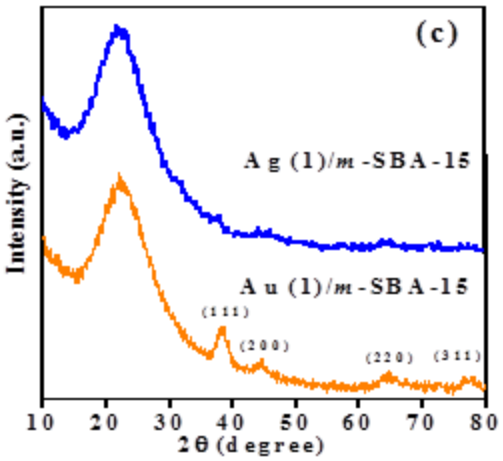

Fig. 5.1 (c) Wide angle Powder XRD pattern of Au/*m*-SBA-15 and Ag/*m*-SBA-15 catalyst.

cubic (FCC) structures and lattice constants (0.408 nm and 0.409 nm) of Au and Ag respectively, it becomes difficult to differentiate Au-Ag bimetallic phase from either monometallic phase based on XRD patterns (Yen et al., 2009). However, in addition to the peaks corresponding to monometallic Au or Ag phase, the spectra of Au-Ag (1:1) loading also showed weak peaks at 27.8 and 32.3^{o} corresponding to the FCC planes of AgCl (JCPDS- 01-1013). This further indicated the presence of small amounts of AgCl on the surface of (BM) Au-Ag nanocomposites. However, these peaks disappeared as the Au loading was increased from 1 to 10 wt. %. This has been supported by the elemental analysis results (discussed later) that showed the absence of AgCl for higher Au loading. With the increase in Au loading, the sharpness of the peaks increased (decrease in the full width at half maxima i.e., FWHM) suggesting an increase in the size of BM NPs formed within the mesoporous sieves. The average particle size of Au (1)/*m*-SBA-15 calculated from the Scherrer equation for (111) peak was found to be 3.9 nm whereas it was found to be 5.5 nm, 5.7 nm and 17.9 nm for Au-Ag (1:1), (5:1) and (10:1) loaded *m*-SBA-15 nanocomposites respectively. Thus, BM Au-Ag (x:y)/*m*-SBA-15 nanocomposites exhibited quite larger size in comparison to monometallic Au/*m*-SBA-15 respectively. This may be due to the presence of small amounts of AgCl that may have been formed due to the galvanic replacement reaction between Au and Ag precursor and is not removed during washing with NH_3 solution. Thus, it is expected that the prepared materials contained both BM Au-Ag NPs and some AgCl particles. Yang et al. (2013) also reported similar findings for Ag-loaded Au-Ag metal core/alloy-shell SBA-15 nanocomposites. However, for higher Au loading w.r.t fixed (1 wt. %) Ag loading, a lesser amount of AgCl particles may have been formed, leading to their easy removal by NH_3 solution. As a result, the peaks corresponding to AgCl were not seen in the spectra of higher Au loaded (5 and 10 wt. %) BM nanocomposites.

TEM

TEM micrographs of SBA-15 (Fig. 5.2a) displayed a regular hexagonal mesoporous structure with a long range ordering of mesochannels. Impregnation of 1 wt. % of Au (Fig. 5.2b) and Ag (Fig. 5.2c) resulted in the formation of highly dispersed nanospheres (NS) (size ~4 and ~6 nm) stabilized and confined within the mesoporous channels. In comparison to monometallic Au or Ag-loaded SBA-15, (BM) Au:Ag (x:y)/*m*-SBA-15 nanocomposites with (1:1) and (5:1) loading of Au:Ag (Fig. 5.2d, e and f), depicted NS (size ~5 nm and ~6 nm) extending as tiny dark spots uniformly distributed throughout the channels of the mesoporous support. These observations indicated that the mesoporous structure was preserved even at higher metal loadings, in agreement with the low angle XRD studies. However, for Au:Ag (1:1) loading beside the presence of well dispersed NS, some larger aggregated particles were seen on the surface of the SBA-15 support. With further increase in Au loading to 5 wt. %, slight disruption of mesoporous channels took place due to the development of strain with increased amount of BM impregnation. As a result, some of the NS was even observed on the external surface of the siliceous host (Fig. 5.2f). For Au:Ag (10:1)/*m*-SBA-15 (Fig. 5.2g), owing to the restriction imposed by the channel walls, excess of the NPs aligned one after the other under the form of rod-like morphology (diameter ~8 nm and length between 50-180 nm) extending as long nanorods (NR) along the mesochannels. It is thus concluded that Au:Ag (5:1) is the optimum amount of loading for homogeneous dispersal of BM NPs within/on the mesoporous support. Beyond this value, the NPs get packed one after the other (as depicted in TEM micrographs) resulting in the formation of NR. Moreover, comparatively large sized BM nanocomposites were formed on alloying (1:1) ratio of Au:Ag contrary to the reported findings (Liu et al., 2008). This may be due to the formation of small amounts of AgCl NPs (depicted in Fig. 5.2d) as a result of galvanic replacement reaction between $HAuCl_4$ and $AgNO_3$ that have not been removed completely during washing. The formation of AgCl resulted in the enlargement of Au-Ag NPs because of the lower melting point of AgCl than that of metallic Ag (Wang et al., 2005b), in consonance with the wide-angle XRD pattern of Au:Ag (1:1) /*m*-SBA-15. However, for BM nanocomposites with 5 and 10 wt. % Au loading (w.r.t 1 wt. % Ag loading) lesser amount of AgCl has been formed that may have been completely removed during washing. As a result, no major increase in the size of NPs was observed for 5 wt. % Au loaded BM nanocomposites whereas 10 wt. % Au

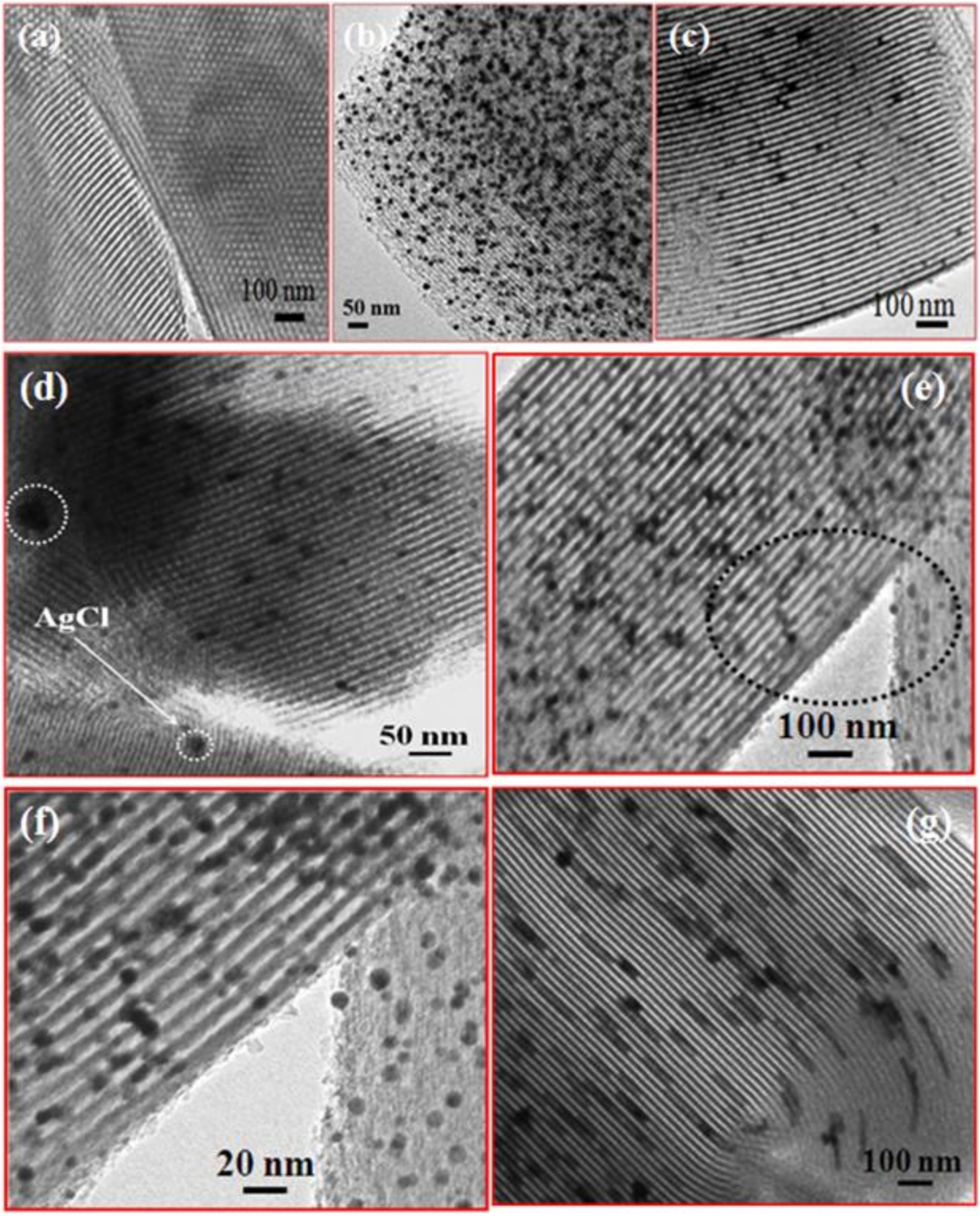

Fig. 5.2 TEM images of **(a)** SBA-15, **(b)** Au(1)/*m*-SBA-15, **(c)** Ag(1)/*m*-SBA-15, **(d)** Au:Ag(1:1)/*m*-SBA-15, **(e-f)** Au:Ag(5:1)/*m*-SBA-15 and **(g)** Au:Ag(10:1)/*m*-SBA-15 catalyst.

loaded BM nanocomposites led to the formation of NR (aspect ratio ~15-20 nm). This is further supported through the wide-angle XRD pattern of (5:1) and (10:1) Au:Ag loading, where peaks corresponding to AgCl were not observed. Elemental mapping studies (Fig. 5.3a) also represented the uniform distribution of SiO_2 species with Au and Ag nano species being overlapped in the Au:Ag (5:1)/*m*-SBA-15, thus forming a homogeneous phase across the mesoporous matrix. The corresponding SAED (Fig. 5.3b) pattern further established the (220), (400) and (422) planes of Au/Ag on the siliceous host. EDX (Fig. 5.3c) studies further revealed the presence of both Au and Ag and absence of AgCl nano species on the mesoporous support.

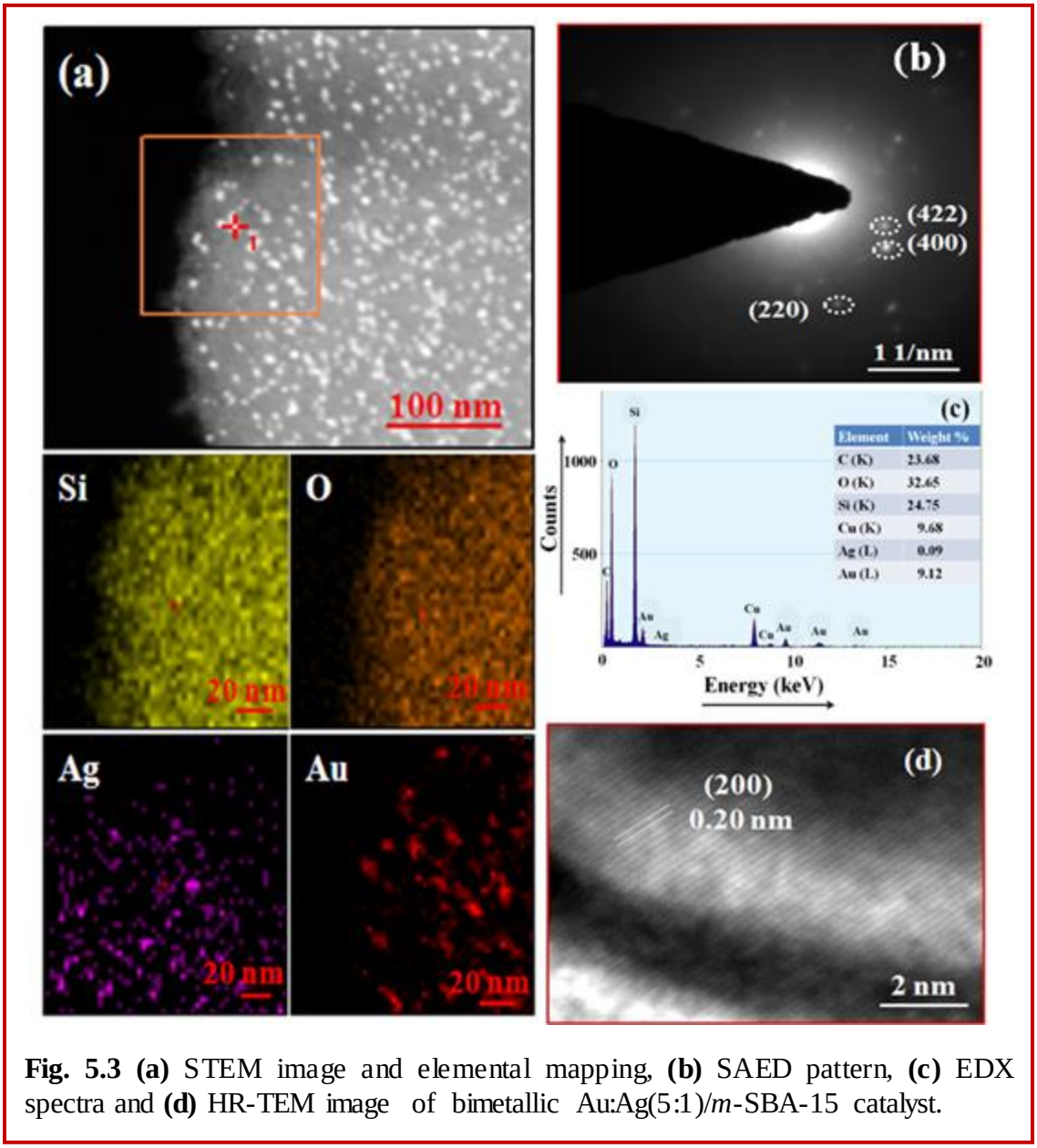

Fig. 5.3 (a) STEM image and elemental mapping, **(b)** SAED pattern, **(c)** EDX spectra and **(d)** HR-TEM image of bimetallic Au:Ag(5:1)/*m*-SBA-15 catalyst.

The HR-TEM image (Fig. 5.3d) depicted lattice fringes ~0.20 nm corresponding to the (200) planes of Au/Ag. However, owing to the similar lattice constants and FCC structures, it is not possible to confirm the alloy nature of Au-Ag NPs from the HR-TEM image.

5.3.4 Optical studies

The solid state UV-visible absorbance spectra (Fig. 5.4A) of Au/*m*-sba-15 and Ag/*m*-SBA-15 exhibited a single and strong absorption band at 503 nm and 366 nm respectively, in consistency with the reported values of pure Au and Ag NPs (Rodriguez-Gonzalez et al., 2004; Yen et al., 2009), while no band was observed for bare SBA-15. For all BM Au-Ag/*m*-SBA-15 nanocomposites, a single band at an intermediate position between that of pure Au and Ag was observed indicating that the NPs formed an alloy structure with homogeneous composition. This is supported by the TEM images (Fig. 5.2d and e) depicting all the particles having nearly similar morphology (spherical) and structure. Similar findings have been reported elsewhere (Qu et al., 2013). The formation of alloy has been further confirmed by comparing the spectra of (1:1) mixture of pure Au and Ag NPs loaded *m*-SBA-15 with that of the bimetallic

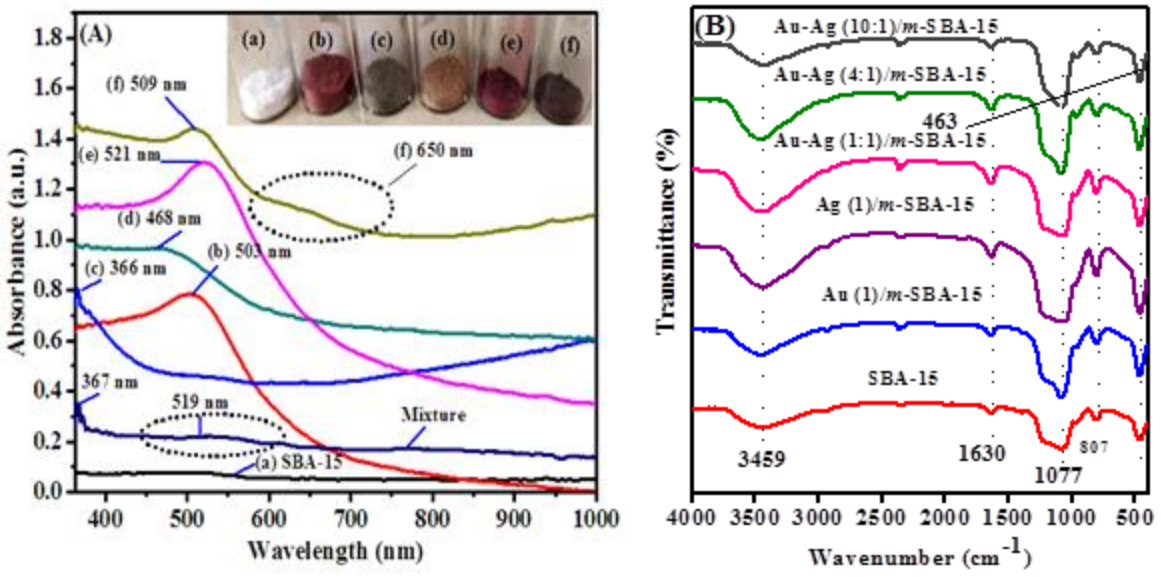

Fig. 5.4 (A) Solid state absorption spectra of **(a)** bare SBA-15, **(b)** Au(1)/*m*-SBA-15, **(c)** Ag(1)/*m*-SBA-15, **(d)** Au:Ag(1:1)/*m*-SBA-15, **(e)** Au:Ag(5:1)/*m*-SBA-15 and **(f)** Au:Ag(10:1)/*m*-SBA-15 catalyst and **(B)** FTIR spectra of bare SBA-15, monometallic Au/Ag loaded SBA-15 and various wt. % bimetallic Au:Ag/*m*-SBA-15 catalysts.

Au:Ag (1:1)/*m*-SBA-15. The spectra of (1:1) mixture of pure Au and Ag NPs depicted a peak at 367 nm and a weak band at 519 nm corresponding to the peak absorbance of Ag and Au respectively, whereas for BM Au:Ag (1:1)/*m*-SBA-15, a single broad band was observed at 468 nm. This further suggested that the BM solution consisted of alloy NPs and not a mixture of Au and Ag NPs. Mallin et al. (2002) also observed two separate peaks at 399 nm and 523 nm for the physical mixture of Ag and Au NPs respectively, while a single broad band at 455 nm for the (1:1) ratio of Au:Ag alloy. Moreover, with the bimetallic impregnation a change in the color of the nanocomposites from white (for bare SBA-15) to dark purple [Au:Ag(10:1) loading] also confirmed the inclusion of Au:Ag within the mesoporous sieves. However, as the Au loading was increased from Au:Ag (1:1) to (5:1), the surface plasmon band red shifted from 468 nm to 521 nm due to the Au-Ag interactions thus implying the formation of Au-rich alloy. As the Au/SBA-15 nanocomposites exhibit absorption bands at ~530 nm, so with the increase in Au content, the absorption will always shift in this direction. With further increase in the Au loading to 10 wt. %, the spectra depicted a blue shift of the absorption band to 509 nm with the appearance of a weak band at 650 nm indicating a probable change in the morphology of embedded BM NPs within the SBA-15. This is consistent with the TEM micrographs of Au:Ag (10:1)/*m*-SBA-15 that further established the presence of anisotropic NPs (NR) at higher Au loading. The presence of a weak band further indicated that the formed anisotropic NPs were not perfect NR but were the result of the alignment of (BM) Au-Ag NS one after the other (due to increased BM loading) forming the shape of NR.

The FTIR spectra (Fig. 5.4B) depicted characteristic SBA-15 bands at 3459 cm^{-1} corresponding to the stretching frequencies of the hydrogen bonded silanols and the absorbed water molecules, whereas the band at 1630 cm^{-1} could be assigned to bending vibration of O-H bonds overlapped with C-O-C stretching vibrations (Azimov et al., 2012; Wang et al., 2005c). In addition, the presence of bands at 463, 807 and 1077 cm^{-1} attributed to the rocking, bending and asymmetric vibrations of tetrahedral SiO_4 groups. As seen the absorption bands of SBA-15 were also present in monometallic and BM nanocomposites suggesting that the basic structure of SBA-15 was maintained even after metal loading.

5.3.5 Surface area studies

The N_2 adsorption-desorption isotherm of SBA-15 (Fig 5.5a) exhibited type IV isotherms, according to IUPAC classification (Sing et al., 1985) with a characteristic H1type hysteresis curve. The curve depicted a single step capillary condensation and capillary evaporation indicative of uniform mesoporous structure. A similar type of isotherm was obtained for monometallic Au/Ag-loaded materials, implying no major structural deformation with metal loading. However, a decrease in the surface area, pore volume and pore size (Table 5.1) were observed, attributed to the confinement of Au/Ag NPs within the mesopores (Sing et al., 1985). In comparison to monometallic Au/Ag-loaded *m*-SBA-15 materials, various BM Au:Ag(x:y)/*m*-SBA-15 nanocomposites exhibited a further decrease in textural properties (Table 5.1) implying the incorporation of (BM) Au-Ag NPs within the mesochannels. These findings are in consonance with the XRD results (decrease in lattice parameters, Table 5.1). All the BM nanocomposites displayed a single step capillary condensation in the adsorption branch with shifting of the inflection point to the lower relative pressure signifying the decrease in pore size. This has been further confirmed by the observed decrease in the pore size distribution from ~8 nm for SBA-15 to ~5.9 nm for Au:Ag(10:1)/*m*-SBA-15 nanocomposites (Fig. 5.5b). However, the desorption branch in the isotherms depicted two step capillary evaporation with forced closure at relative pressure p/p_o ~0.48 for 5 wt. % and 10 wt. % Au loaded BM nanocomposites.

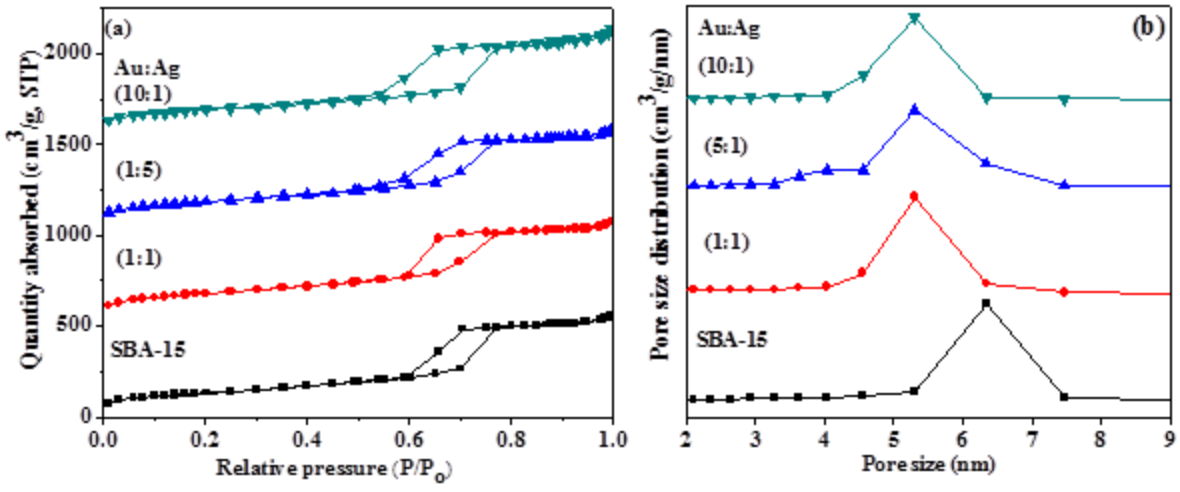

Fig. 5.5 (a) Nitrogen adsorption-desorption isotherms and **(b)** pore size distribution of bare SBA-15 and various wt. % bimetallic Au:Ag/*m*-SBA-15 catalysts.

The forced closure of the hysteresis in the desorption branch at p/p_o ~0.48 conformed to the plugging of the pores (Sietsma et al., 2008) and is known as the pore-blocking effect/cavitation effect (Van der Voort et al., 2002). This cavitation phenomenon arises due to the partial pore blockage as a result of the presence of a greater amount of (BM) Au-Ag NPs within the aperture of the pores. As a result, significant pore-blocking is observed for (BM) Au:Ag (5:1) and (10:1) loading. Similar decreases in structural parameters with increased Au loading has been observed (as discussed in section 2.3.4, chapter 2). Naik et al. (2011) also reported pore-plugging leading to decrease in textural properties at higher metal loading for Ag/SBA-15 nanocomposites.

Table 5.1 Physicochemical parameters of bare SBA-15, monometallic Au/Ag-loaded SBA-15 and various wt. % bimetallic Au:Ag/*m*-SBA-15 catalysts.

Sample	d-spacing, d_{100} (nm)	unit cell parameter, a_o (nm)[a]	wall thickness, d_w (nm)[b]	Surface area (m^2/g)	Pore volume (cm^3/g)	Pore size (nm)	Metal loading (wt. %)	
							Au	Ag
SBA-15	10.12	11.68	1.57	694	1.37	8.06		
Au/*m*-SBA-15	10.09	11.65	1.56	475	0.82	6.92	0.86	
Ag/*m*- SBA-15	10.08	11.63	1.55	507	0.91	7.21		0.67
Au:Ag (1:1)/*m*-SBA-15	10.11	11.67	1.56	490	0.82	6.68	0.89	0.56
Au:Ag (5:1)/*m*-SBA-15	10.09	11.65	1.56	478	0.77	6.44	3.74	0.68
Au:Ag (10:1)/*m*-SBA-15	10.08	11.63	1.55	533	0.79	5.95	7.99	0.54

[a] $a_0 = 2/3^{1/2} d_{100}$, [b] $d_w = a_0 - d_{100}$

5.3.6 Catalytic activity

The catalytic activity of the prepared nanocomposites was evaluated for the reduction of nitrobenzene (NB) (Scheme 5.1) and *p*-nitro acetophenone (NAP) (Scheme 5.2) respectively. It was found that the BM nanocomposites exhibited higher catalytic activity than monometallic nanocomposites in comparison to negligible activity with bare SBA-15. As shown in Fig. 5.6 a and b, the catalytic activities followed the order Au:Ag(5:1)/*m*-SBA-15>Au:Ag(10:1)/*m*-SBA-15>Au(1)/*m*-SBA-15>Au:Ag(1:1)/*m*-SBA-15>Ag(1)/*m*-SBA-15>SBA-15. In comparison to monometallic Au/*m*-SBA-15 (1.68×10^{-2} min^{-1} and 3.31×10^{-2} min^{-1}), BM Au:Ag(5:1)/*m*-SBA-15 nanocomposite exhibited a much higher rate of reaction (2.12×10^{-2} min^{-1} and 3.99×10^{-2} min^{-1}), in comparatively short contact time for both reduction of NB and *p*-NAP (Fig. 5.8) respectively. Both the reduction of NB and *p*-NAP resulted in the formation of aniline and *p*-AAP respectively as confirmed by the HPLC analysis (Fig. 5.7). In fact, the higher catalytic performance of BM nanocomposites can be explained on the basis of strong synergistic electronic effect (Xu et al.,

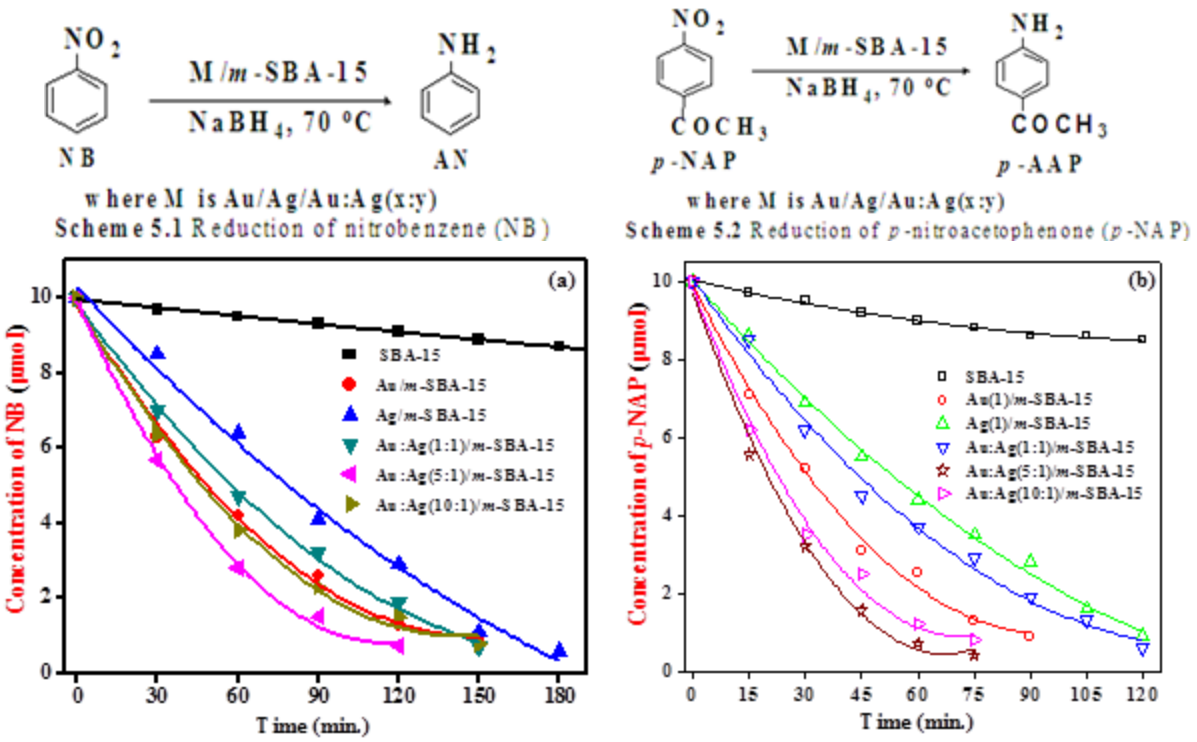

Fig. 5.6 Time course graph of **(a)** nitrobenzene (NB) reduction and **(b)** *p*-nitroacetopheneone (*p*-NAP) by bare SBA-15, monometallic Au/Ag loaded SBA-15 and various wt. % bimetallic Au:Ag/*m*-SBA-15 catalysts.

2012; Liu et al., 2005) of Au with Ag implying that Au and Ag atoms together comprised the active sites. This has been further supported by the DRS studies that depicted the single absorbance band for various loadings of BM nanocomposites. Although the catalytic properties of the supported catalyst were greatly influenced by the metal/support interactions as well as the shape and size of metallic NPs embedded within the support. However, the present study implied that the particle size does not seem to influence much the catalytic activity. As the BM nanocomposites exhibited a larger average particle size ~5-8 nm in contrast to the small sized ~4 nm (for monometallic Au) and ~6 nm (for monometallic Ag) nanocomposites and still showed improved catalytic activity. This is in consonance with the report of Iizuka et al. (2009) where the presence of small amounts of Ag as an impurity to the Au nanopowder resulted in the enhancement of its catalytic activity for CO oxidation. Moreover, Zhou et al. (2011) also found that the improvement in the catalytic activity for CO oxidation was due to the addition of CeO_2 NPs (~5 nm) to the Au film which acted as the active sites. Similarly, Jurgens et al. (2007) stated nanoporous Au formed by the Ag leaching of Au-Ag alloy resulted in increased catalytic activity

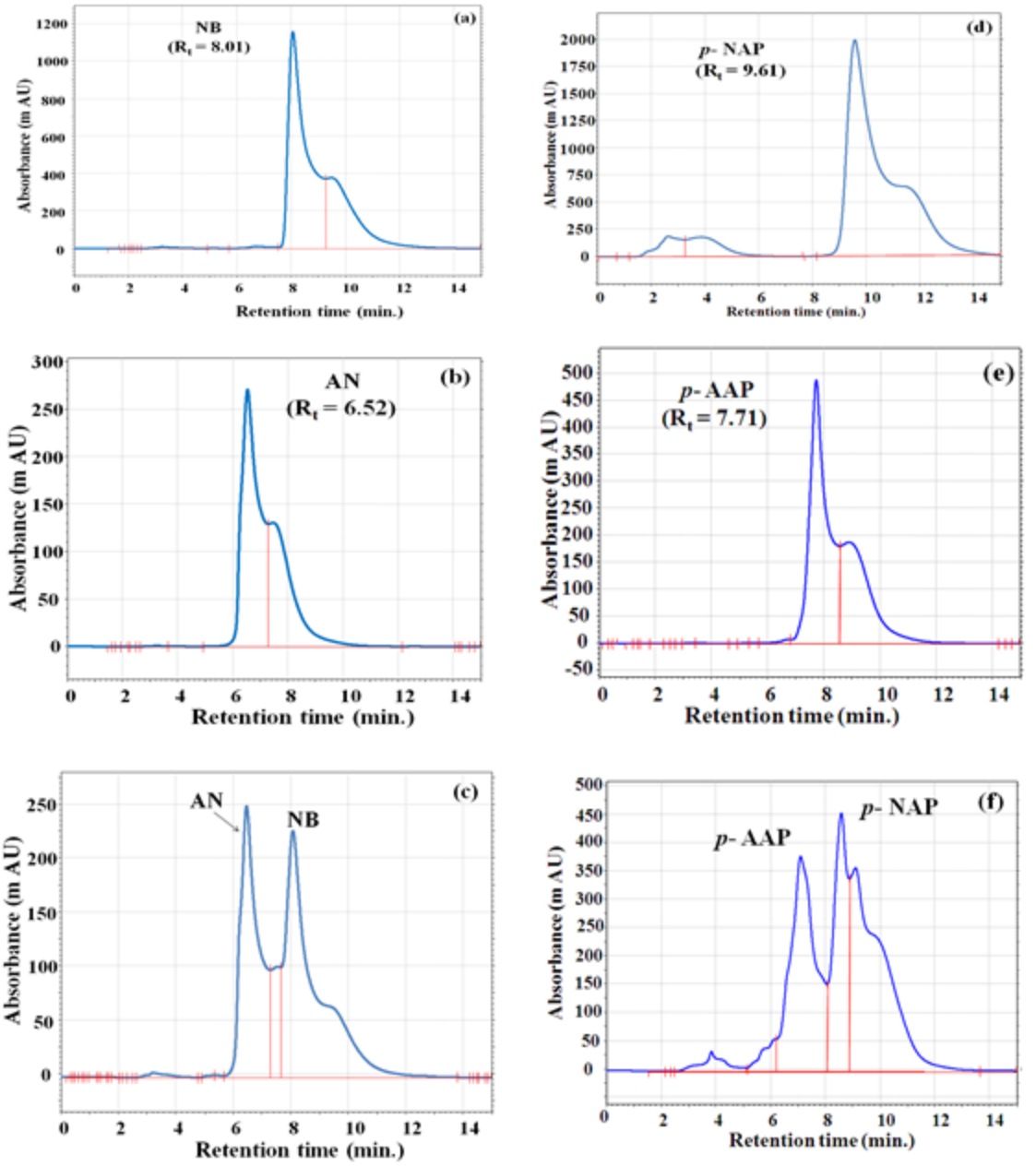

Fig. 5.7 HPLC chromatograms of reaction sample for nitrobenzene reduction **(a-b-c)** at 90 min. and *p*-nitroacetophenone **(d-e-f)** reduction at 30 min. catalysed by Au:Ag(5:1)/*m*-SBA-15 catalyst.

for CO oxidation. Thus, it is the interaction between the Au and Ag that is responsible for improving the catalytic activity rather than the size of Au (Fujita et al., 2012). Among the BM nanocomposites, Au:Ag(5:1)/*m*-SBA-15 showed the excellent catalytic performance in comparison to (1:1) and (10:1) loading. This could be attributed to the fact that with the increased amount of Au:Ag loading, the strain is developed within the mesoporous channels leading to their slight disruption. As a result, BM NS (as revealed in TEM micrographs, Fig.

5.2e-f) come to lie within as well as on the surface of the support. Thus, the presence of BM NS both on the outer as well as the inner surface of the support result in increased number of accessible active sites that favor the easy movement of reactants towards the active sites resulting in high catalytic activity (Zhou et al., 2011). Further, the decrease in the surface area, pore volume and pore size (Table 5.1) for Au:Ag (5:1) loading also indicate the presence of highly dispersed Au-Ag NPs within/on the surface of mesochannels. However, as the Au:Ag loading increased to (10:1), the decrease in catalytic activity was observed that could be accredited to the partial blocking of mesopores with further increase in the amount of bimetallic impregnation. Here, the possibility of diffusion limitation cannot be avoided due to intensive encapsulation of bimetallic NS within the long mesochannels of the host. As a result, the NPs deep seated within the channels of the host do not participate in the reaction consequently decreasing the effective no. of active sites resulting in decreased catalytic activity. In contrast, nanocomposites with Au:Ag (1:1) loading exhibited lower catalytic activity, even in comparison to the monometallic Au/*m*-SBA-15 credited to the presence of large sized AgCl NPs present on the surface (in accordance with the XRD and TEM studies) that interfere with the catalytic activity. Moreover, in order to test the heterogeneity and stability of the prepared materials, recycling experiments were carried out using Au:Ag(5:1)/*m*-SBA-15 as a catalyst for the reduction of *p*-NAP under the optimized reaction conditions. For reusability, the catalyst was separated from the reaction mixture, filtered and dried overnight at 60 ^{o}C. It was found that the catalyst can be reused repeatedly till 4 recycles with no major decrease in the selectivity of the *p*-AAP. The conversion obtained was still 100 %, however, the reaction time increased to 4h. Moreover, the amount of the catalyst recovered from the mixture was 3.9 mg in comparison to the optimum amount (5 mg) of the fresh catalyst used for the reaction. This might

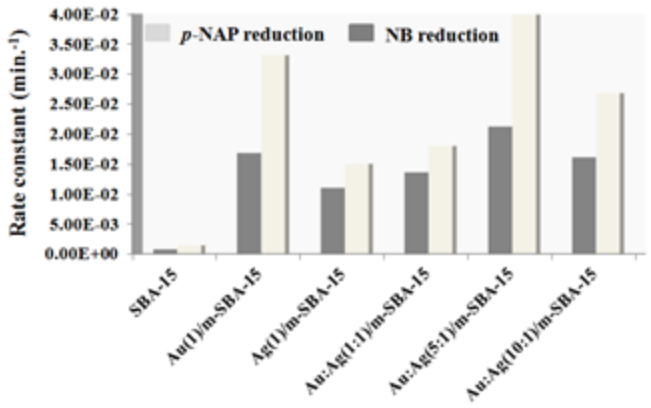

Fig. 5.8 Comparison of rate of reaction for reduction of nitrobenzene and *p*-nitroacetopheneone (*p*-NAP) by bare SBA-15, monometallic Au/Ag loaded SBA-15 and various wt. % bimetallic Au:Ag/*m*- SBA-15 catalysts.

be due to the loss of a small amount of catalyst during catalyst recovery. These experimental results established the stability and heterogeneous nature of the catalyst.

Various bimetallic Au:Ag/ SBA-15 nanocomposites with controlled shape and size were prepared by varying the Au loading w.r.t fixed Ag loading. The strong synergism between Au and Ag resulted in the improved catalytic activity of the bimetallic Au:Ag nanocomposites in comparison to the monometallic Au/Ag counterparts and bare SBA-15 for the reduction of NB and p-NAP respectively. Furthermore, the catalytic activity was greatly influenced by Au loading, surface area and distribution of bimetallic NS within /on the surface of the mesoporous host. Of all the prepared nanocomposites, Au:Ag(5:1)/m-SBA-15 showed the highest catalytic activity for reduction of NB and p-NAP respectively. Keeping in view, the simple synthesis, easy retrieval and high catalytic activity, this method can also be extended to the formation of other bimetallic systems.

5.4 References

Azimov, F., Markova, I., Stefanova, V. and Sharipov, Kh., 2012. Synthesis and characterization of SBA-15 and Ti-SBA-15 nanoporous materials for DME catalysts. Journal of the University of Chemical Technology and Metallurgy, 47(3), pp.333-340.

Bond, G.C., 1991. Supported metal catalysts: some unsolved problems. Chemical Society Reviews, 20(4), pp.441-475.

Chandrasekhar, S., Prakash, S.J. and Rao, C.L., 2006. Poly (ethylene glycol)(400) as superior solvent medium against ionic liquids for catalytic hydrogenations with PtO_2. The Journal of organic chemistry, 71(5), pp.2196-2199.

Chi, Y.S., Lin, H.P. and Mou, C.Y., 2005. CO oxidation over gold nanocatalyst confined in mesoporous silica. Applied Catalysis A: General, 284(1), pp.199-206.

Chiang, C.W., Wang, A., Wan, B.Z. and Mou, C.Y., 2005. High catalytic activity for CO oxidation of gold nanoparticles confined in acidic support Al-SBA-15 at low temperatures. The Journal of Physical Chemistry B, 109(38), pp.18042-18047.

Fujita, T., Guan, P., McKenna, K., Lang, X., Hirata, A., Zhang, L., Tokunaga, T., Arai, S., Yamamoto, Y., Tanaka, N. and Ishikawa, Y., 2012. Atomic origins of the high catalytic activity of nanoporous gold. Nature materials, 11(9), pp.775-780.

Han, J., Fang, P., Jiang, W., Li, L. and Guo, R., 2012. Ag-nanoparticle-loaded mesoporous silica: spontaneous formation of Ag NPs and mesoporous silica SBA-15 by a one-pot strategy and their catalytic applications. Langmuir, 28(10), pp.4768-4775.

Iizuka, Y., Miyamae, T., Miura, T., Okumura, M., Date, M. and Haruta, M., 2009. A kinetic study on the low temperature oxidation of CO over Ag contaminated Au fine powder. Journal of Catalysis, 262(2), pp.280-286.

Ivashchenko, N.A., Gac, W., Tertykh, V.A., Yanishpolskii, V.V., Khainakov, S.A., Dikhtiarenko, A.V., Pasieczna-Patkowska, S. and Zawadzki, W., 2012. Preparation, characterization and catalytic activity of palladium nanoparticles embedded in the mesoporous silica matrices. World Journal of Nano Science and Engineering, 2(3), pp.117-125.

Jurgens, B., Kubel, C., Schulz, C., Nowitzki, T., Zielasek, V., Biener, J., Biener, M.M., Hamza, A.V. and Baumer, M., 2007. New gold and silver-gold catalysts in the shape of sponges and sieves. Gold Bulletin, 40(2), pp.142-149.

Kustov, L.M., 2013. Catalytic properties of supported gold nanoparticles in organic syntheses. Russian Chemical Bulletin, 62(4), pp.869-877.

Liu, J.H., Wang, A.Q., Chi, Y.S., Lin, H.P. and Mou, C.Y., 2005. Synergistic effect in an Au-Ag alloy nanocatalyst: CO oxidation. The Journal of Physical Chemistry B, 109(1), pp.40-43.

Liu, X., Wang, A., Yang, X., Zhang, T., Mou, C. Y., Su, D.S. and Li, J., 2008. Synthesis of thermally stable and highly active bimetallic Au-Ag NPs on inert supports. Chemistry of Materials, 21(2), pp.410-418.

Liu, X., Wang, A., Yang, X., Zhang, T., Mou, C.Y., Su, D.S., Li, J., Mu, R., Fu, Q. and Xu, H., 2011. Synergetic effect of surface and subsurface Ni species at Pt-Ni bimetallic catalysts for CO oxidation. Journal of the American Chemical Society, 133(6), pp.1978-1986.

Mallin, M.P. and Murphy, C.J., 2002. Solution-phase synthesis of sub-10 nm Au-Ag alloy nanoparticles. Nano Letters, 2(11), pp.1235-1237.

Mureddu, M., Ferino, I., Musinu, A., Ardu, A., Rombi, E., Cutrufello, M.G., Deiana, P., Fantauzzi, M. and Cannas, C., 2014. MeO_x/SBA-15 (Me= Zn, Fe): highly efficient nanosorbents for mid-temperature H_2S removal. Journal of Materials Chemistry A, 2(45), pp.19396-19406.

Murugadoss, A., Kai, N. and Sakurai, H., 2012. Synthesis of bimetallic gold-silver alloy nanoclusters by simple mortar grinding. Nanoscale, 4(4), pp.1280-1282.

Nagy, G., Benko, T., Borko, L., Csay, T., Horvath, A., Frey, K. and Beck, A., 2014. Bimetallic Au-Ag/SiO_2 catalysts: comparison in glucose, benzyl alcohol and CO oxidation reactions. Reaction Kinetics, Mechanisms and Catalysis, 115(1), pp.45-65.

Naik, B., Hazra, S., Prasad, V.S. and Ghosh, N.N., 2011. Synthesis of Ag NPs within the pores of SBA-15: an efficient catalyst for reduction of 4-nitrophenol. Catalysis Communications, 12(12), pp.1104-1108.

Pal, A., Shah, S. and Devi, S., 2007. Synthesis of Au, Ag and Au-Ag alloy nanoparticles in aqueous polymer solution. Colloids and Surfaces A: Physicochemical and Engineering Aspects, 302(1), pp.51-57.

Qu, Z., Ke, G., Wang, Y., Liu, M., Jiang, T. and Gao, J., 2013. Investigation of factors influencing the catalytic performance of CO oxidation over Au-Ag/SBA-15 catalyst. Applied Surface Science, 277, pp.293-301.

Rahaim, R.J. and Maleczka, R.E., 2005. Pd-catalyzed silicon hydride reductions of aromatic and aliphatic nitro groups. Organic letters, 7(22), pp.5087-5090.

Rodriguez-Gonzalez, B., Sanchez-Iglesias, A., Giersig, M. and Liz-Marzan, L. M., 2004. Au-Ag bimetallic nanoparticles: formation, silica-coating and selective etching. Faraday discussions, 125, pp.133-144.

Shi, Q., Lu, R., Lu, L., Fu, X. and Zhao, D., 2007. Efficient Reduction of Nitroarenes over Nickel-Iron Mixed Oxide Catalyst Prepared from a Nickel-Iron Hydrotalcite Precursor. Advanced Synthesis & Catalysis, 349(11-12), pp.1877-1881.

Sietsma, J.R., Meeldijk, J.D., Versluijs-Helder, M., Broersma, A., Dillen, A.J.V., de Jongh, P.E. and de Jong, K.P., 2008. Ordered mesoporous silica to study the preparation of Ni/SiO_2 ex nitrate catalysts: Impregnation, drying, and thermal treatments. Chemistry of materials, 20(9), pp.2921-2931.

Sing, K.S., 1985. Reporting physisorption data for gas/solid systems with special reference to the determination of surface area and porosity (Recommendations 1984). Pure and applied chemistry, 57(4), pp.603-619.

Torres, C., Campos, C., Fierro, J.L.G., Oportus, M. and Reyes, P., 2013. Nitrobenzene Hydrogenation on Au/TiO_2 and Au/SiO_2 Catalyst: Synthesis, Characterization and Catalytic Activity. Catalysis letters, 143(8), pp.763-771.

Van der Voort, P., Ravikovitch, P.I., De Jong, K.P., Neimark, A.V., Janssen, A.H., Benjelloun, M., Van Bavel, E., Cool, P., Weckhuysen, B.M. and Vansant, E.F., 2002. Plugged hexagonal templated silica: a unique micro and mesoporous composite material with internal silica nanocapsules. Chemical Communications, (9), pp.1010-1011.

Wang, A., Hsieh, Y.P., Chen, Y.F. and Mou, C.Y., 2006. Au-Ag alloy nanoparticle as catalyst for CO oxidation: Effect of Si/Al ratio of mesoporous support. Journal of Catalysis, 237(1), pp.197-206.

Wang, A.Q., Chang, C.M. and Mou, C.Y., 2005a. Evolution of catalytic activity of Au-Ag bimetallic nanoparticles on mesoporous support for CO oxidation. The Journal of Physical Chemistry B, 109(40), pp.18860-18867.

Wang, A.Q., Liu, J.H., Lin, S.D., Lin, T.S. and Mou, C.Y., 2005b. A novel efficient Au-Ag alloy catalyst system: preparation, activity, and characterization. Journal of Catalysis, 233(1), pp.186-197.

Wang, X., Lin, K.S.K., Chan, J.C.C. and Cheng, S., 2005c. Direct synthesis and catalytic applications of ordered large pore aminopropyl-functionalized SBA-15 mesoporous materials. The Journal of Physical Chemistry B, 109, pp.1763-1769.

Wang, X., Sun, T., Yang, J., Zhao, L. and Jia, J., 2008. Low-temperature H_2S removal from gas streams with SBA-15 supported ZnO nanoparticles. Chemical Engineering Journal, 142(1), pp.48-55.

Xu, W., Si, R., Senanayake, S.D., Llorca, J., Idriss, H., Stacchiola, D., Hanson, J.C. and Rodriguez, J.A., 2012. In situ studies of CeO_2 supported Pt, Ru, and Pt-Ru alloy catalysts for the water-gas shift reaction: active phases and reaction intermediates. Journal of Catalysis, 291, pp.117-126.

Yang, L., Qi, M. and Jin, M., 2013. Fabrication of SBA-15 supported Ag@ Au-Ag metal-core/alloy-shell nanoparticles for CO oxidation. Crystal Engineering Communications 15(15), pp.2804-2808.

Yen, C.W., Lin, M.L., Wang, A., Chen, S.A., Chen, J.M. and Mou, C.Y., 2009. CO oxidation catalyzed by Au-Ag bimetallic nanoparticles supported in mesoporous silica. The Journal of Physical Chemistry C, 113(41), pp.17831-17839.

Zhang, H., Tang, C., Lv, Y., Sun, C., Gao, F., Dong, L. and Chen, Y., 2012. Synthesis, characterization and catalytic performance of copper-containing SBA-15 in the phenol hydroxylation. Journal of colloid and interface science, 380(1), pp.16-24.

Zhao, D., Feng, J., Huo, Q., Melosh, N., Fredrickson, G.H., Chmelka, B.F. and Stucky, G.D., 1998. Triblock copolymer syntheses of mesoporous silica with periodic 50 to 300 angstrom pores. Science, 279(5350), pp.548-552.

Zheng, J., Lin, H., Wang, Y.N., Zheng, X., Duan, X. and Yuan, Y., 2013. Efficient low-temperature selective hydrogenation of esters on bimetallic Au-Ag/SBA-15 catalyst. Journal of Catalysis, 297, pp.110-118.

Zhou, Z., Flytzani-Stephanopoulos, M. and Saltsburg, H., 2011. Decoration with ceria nanoparticles activates inert gold island/film surfaces for the CO oxidation reaction. Journal of Catalysis, 280(2), pp.255-263.

Summary, Conclusions and future perspectives

The present study involved the preparation of transition metal (Au, Ag and CuO) supported SBA-15 nanocomposites and the effect of the incorporation of embedded metal/metal-oxide nanoparticles on various physicochemical and catalytic properties depending on the nature of metal as well as the amount of metal loading. The catalytic activity of the various nanocomposites was evaluated for a series of nitroaromatics using $NaBH_4$ as reducing agent. Initially, an introductory note on the porous materials including historical background of porous materials, major breakthroughs and advancements in the field of mesoporous materials has been described. Moreover, the various pathways used for the synthesis of different mesoporous silicates like MCM-41 and SBA-15 have also been discussed. It further inculcated the need and the methods by which an inert mesoporous support like SBA-15 is converted into a potential heterogeneous catalyst to be used for different industrially important reactions. Thus, paving a way for the host -guest chemistry, in which mesoporous materials act as the host on which metal nanoparticles are incorporated as a guest. Generally, transition metals have been incorporated as a guest on mesoporous host owing to their high surface energy and surface-to-volume ratio, making their surface atoms very active. A brief overview of the various reports on transition metal (monometallic viz., Au, Ag, Cu and bimetallic viz., Au-Ag) incorporated SBA-15 catalytic systems have been included in the literature. Moreover, experimental methods viz., synthesis of bare SBA-15, its surface functionalisation with APTMS/APTES, the formation of Au/Ag/CuO as well as bimetallic Au-Ag loaded SBA-15 nanocomposites by post modification and characterisation techniques used in the present study have also been explained.

Initially, SBA-15 was prepared and its surface was modified with APTMS/APTES followed by metallic (Au/Ag/CuO) or bimetallic (Au-Ag) impregnation. It was demonstrated that the strong interactions between the surface modified support and the metal nanoparticles promoted the formation of homogeneously dispersed and highly stabilized metal nanostructures within the pores of the host which have been further supported by various characterization analysis. FTIR and TGA studies confirmed the retention of mesoporous structure and stability of prepared materials even after surface functionalization and metal loading. Moreover, the presence of metal/metal-oxide nanoparticles (Au, Ag and CuO) within the mesoporous sieves was further confirmed by HR-TEM, SAED pattern and EDX spectra. Elemental mapping studies

also depicted uniform dispersal of metal nano species throughout the siliceous support. Low angle Powder XRD spectra also illustrated retention of mesoporous geometry after surface functionalization and metal loading, however, a decrease in the intensities of peaks was observed owing to the pore-filling effect due to the formation of metal nanoparticles within the mesopores. Wide angle XRD spectra depicted characteristic diffraction peaks w.r.t different metals indicating the presence of metal/metal-oxide species within the SBA-15. It was further supported by XPS spectra that confirmed the existence of metallic Au and Ag whereas Cu being susceptible to oxidation was present in the form of CuO within the mesoporous host. On comparing wide angle Powder XRD spectra of Au/Ag/CuO nanocomposites, it was found that for Au loaded SBA-15 nanocomposites, intensity of peaks increased with increase in Au loading from 1-10 wt. %, evidencing an increase in the size and crystallinity of prepared materials. On the contrary, for Ag and CuO loaded SBA-15 nanocomposites, increase in the size of embedded metal/metal-oxide nano species was observed till 4 wt. % of metal loading. Furthermore, the diffraction pattern of 4 wt. % loaded Ag/CuO catalyst showed a difference in the broadening of the peaks corresponding to different planes, suggesting that as metal loading was increased, an effective amount of metal/metal-oxide nano species within the mesopores increased gradually leading to the development of strain. As a result, crystal deformations w.r.t. specified planes increased forming anisotropic nanoparticles (nanospheres and nanorods) within the mesoporous sieves. Beyond 4 wt. % loading, any significant change in the size of metal/metal-oxide nano species was not observed. This was supported by solid state absorption studies that depicted a single absorption band characteristic of respective metals (Au/Ag/ CuO) at lower metal loading implying the formation of highly dispersed nanospheres within the mesoporous host. However, higher metal loading, indicated a probable change in the morphology of metallic species from nanospheres to nanorod-like shape, due to the blue shifting of transverse band and appearance of the weaker longitudinal band in the spectrum. Change in the shape of incorporated metal/metal-oxide nano species at higher metal loading was further confirmed by TEM micrographs that showed the formation of fine homogeneously dispersed nanospheres (average particle size 5-7 nm) for 1- 4 wt. % metal (Au, Ag and CuO) loading and nanorods (average aspect ratio ~15-20 nm) for 10 wt. % metal loading extending along the long mesochannels of SBA-15. It was found that due to the restriction imposed by the channel walls and strain generated within the sieves at higher (10 wt. %) metal loading, an excess of the nanospheres aligned one after the other in the

form of nanorod-like shape. Considering catalytic parameters of Au and Ag-loaded SBA-15 nanocomposites, a catalyst with 4 wt. % Au/Ag loading showed the highest catalytic activity for nitroaromatic reduction. The catalytic activity of Au loaded SBA-15 nanocomposites was evaluated for the reduction of *m*- and *p*-dinitrobenzene (*m*-DNB). It was found that the high Au loading and uniform dispersion of small particle size (~5-6 nm) of Au nanospheres within SBA-15 channels leads to large number of exposed active sites for favoring easy access of reactants and thus contributed towards efficient catalytic activity (89 % selectivity for *m*-phenylenediamine and 81% for *p*-nitroaniline formation). Among the Ag supported SBA-15 nanocomposites, a catalyst with 4 wt. % Ag loading exhibited the highest catalytic activity for the reduction of *p*-DNB and *p*-nitrophenol (*p*- NP) exhibiting 87 % selectivity for *p*-nitroaniline and 100 % selectivity for *p*-aminophenol formation due to high Ag loading that resulted in the formation of well dispersed Ag NPs (active sites) within/on the surface of the mesopores, exhibiting the unexpectedly high surface area (708 m^2/g) more than SBA-15 with improved access of active species to the substrate molecules leading to enhanced catalytic activity. Moreover, the value of rate constant was found to be 4.7×10^{-3} s^{-1} for *p*-NP and 1.803×10^{-1} s^{-1} for *p*-DNB, quite comparable with the reported rate constants where supported Ag catalysts were used, signifying the high efficiency of the prepared catalyst. On the contrary, for CuO loaded SBA-15 catalysts, nanocomposite with 10 wt. % Cu loading displayed highest catalytic efficiency accredited to the increased amount of Cu impregnation and high surface area. Thus, it was concluded that metal loading significantly influences the shape, size, dispersion ability and catalytic activity of the supported metal/metal oxide nanocomposites. For the reduction of *m*-nitrotoluene (*m*-NT) and *m*-chloronitrobenzene (*m*-CNB) catalyzed by CuO loaded SBA-15 catalysts, the reaction rate also showed dependence on the electron withdrawing ability of the substituents present on nitrobenzene and was found to be maximum for *m*-CNB. Further, on comparing the Au/Ag/CuO loaded SBA-15 nanocomposites w.r.t 4 wt. % metal impregnation, it was observed that Au nanospheres impregnated SBA-15 with smallest particle size (~5 nm), better metallic dispersion and lowest surface area (292 m^2/g) exhibited the best catalytic activity for *m*-DNB reduction ($k = 1.765 \times 10^{-1}$ min^{-1}) establishing the fact that catalytic activity could also be well tuned to the desired reach as a function of nature of metal and its dispersion density.

Since the prepared monometallic nanocomposites exhibited enhanced catalytic activity for nitroaromatic reduction, so this methodology was extended for the synthesis of bimetallic

Au-Ag loaded SBA-15 nanocomposites. Of all bimetallic nanocomposites, Au:Ag(5:1)/*m*-SBA-15 nanocomposites exhibited the best catalytic activity ($k= 2.12\times10^{-2}$ min^{-1} and 3.99×10^{-2} min^{-1}) in comparison to monometallic Au/*m*-SBA-15 and Ag/*m*-SBA-15 nanocomposites for the selective reduction of nitrobenzene (NB) to aniline (AN) and *p*-nitro acetophenone (*p*-NAP) to *p*-aminoacetophenone (*p*-AAP)respectively. The strong synergism between Au and Ag resulted in the improved catalytic activity of the bimetallic Au:Ag nanocomposites in comparison to the monometallic Au/Ag counterparts and bare SBA-15. The catalytic activity was greatly influenced by metal loading, surface area and distribution of bimetallic nanospheres within/on the surface of the mesoporous host. Keeping in view, the simple synthesis, easy retrieval and high catalytic activity of prepared nanocomposites, this method can also be extended for the formation of other bimetallic as well as trimetallic systems.

It is thus concluded from the work that catalytic activity of the metal supported SBA-15 nanocomposites can be enhanced with suitable metal impregnation depending upon the nature of metal and amount of metal loading. Moreover, the prepared nanocomposites could be effectively utilized for the selective reduction of nitroaromatics possessing multifunctional reducible groups at *m*- or *p*- position in short reaction time resulting in high yield and minimal side product generation. The easy preparation method, benign reaction conditions, greater selectivity of products and high recyclability of the prepared materials make this protocol to be highly efficient and appealing for the reduction of other nitroaromatics. Moreover, excellent stability and reusability of the catalyst offer a great scope for extending it to other noble metals promising greater opportunities for designing novel materials for various applications.

Future scope

In the work accomplished for this thesis, efforts were made for the preparation and development of a stable heterogeneous catalyst for the nitroaromatic reduction. Although there have been satisfactory results and findings in the work carried out, yet there is scope in the same field. The improved catalytic and physicochemical properties of the prepared materials offers a possibility of extending it to other monometallic, bimetallic (Au-Cu, Ag-Cu), supported core-shell nanocomposites as well as other trimetallic systems for catalyzing other industrially important reactions.

Publications in SCI Journals

1. Shweta Sareen, Vishal Mutreja, Satnam Singh and Bonamali Pal, **"**Homogeneous dispersion of Au nanoparticles into mesoporous SBA-15 exhibiting improved catalytic activity for nitroaromatic reduction" ***Microporous and mesoporous materials*** 202 (2015) 219-225.

2. Shweta Sareen, Vishal Mutreja, Satnam Singh and Bonamali Pal, "Highly dispersed Au, Cu and Cu nanoparticles into mesoporous SBA-15 for highly selective catalytic reduction of nitroaromatics" ***RSC Advances*** 5 (2015) 184-190.

3. Shweta Sareen, Vishal Mutreja, Satnam Singh and Bonamali Pal, "Fine CuO anisotropic nanoparticles supported on mesoporous SBA-15 for selective hydrogenation of nitroaromatics" ***Journal of Colloid and Interface Science*** 461 (2016) 203–210**.**

4. Shweta Sareen, Vishal Mutreja, Satnam Singh and Bonamali Pal, "Preparation, surface structural morphology and catalytic properties of uniformly dispersed Ag nanoparticle loaded mesoporous SBA-15". (Communicated)

5. Shweta Sareen, Vishal Mutreja, Satnam Singh and Bonamali Pal,**"**Uniform dispersion of a bimetallic/binary mixture of Au-Ag supported SBA-15 nanocomposites for selective reduction of nitroaromatics" under preparation.

List of papers/posters presented in conferences

1. Shweta Sareen, Vishal Mutreja, **Satnam Singh** and Bonamali Pal, "Homogeneous dispersion of Au nanoparticles into mesoporous SBA-15 exhibiting improved catalytic activity for nitroaromatic reduction" International Conference on Advances in Functional Materials **(ICAFM-2015)** held at Stony Brook University, NY, USA on June 29th - July 3rd, 2015.

2. Shweta Sareen, Vishal Mutreja, Satnam Singh and Bonamali Pal, "Synthesis and catalytic applications of nanocomposites containing gold and SBA-15" National Conference on Innovative Molecules for Sustainable Future **(NCIMS-2013)** held at Thapar University, Patiala, India on October 24-26th, 2013.

3. Shweta Sareen, Vishal Mutreja, Satnam Singh and Bonamali Pal, **"**Synthesis of well dispersed Au nanorods within mesoporous silica and their catalytic applications" International Conference on Nanotechnology in the service of Health, Environment and Society **(Nanoscitech-2014)** held at Chandigarh, India on February 13-15th, 2014.

4. Shweta Sareen, Vishal Mutreja, Satnam Singh and Bonamali Pal, "Homogeneous dispersion of varying morphologies of Au/SBA-15 nanocomposites for nitroaromatic reduction" National Conference on New frontiers in Chemical Sciences (NFCS-01) held at Khalsa College, Patiala on November 15th, 2014.

5. Shweta Sareen, Vishal Mutreja, Satnam Singh and Bonamali Pal, "Highly dispersed Au nanoparticles in mesoporous SBA-15 for highly selective nitroaromatic reduction" National Conference on **(SACOS 2015)** held at Punjabi University, Patiala, India on November 15-16th, 2015.